UNIVERSITY OF CALIFORNIA
SANTA CRUZ

ELECTRONIC AND MAGNETIC PROPERTIES OF THIN FILM TRANSITION METAL FLUORIDES, TOPOLOGICAL INSULATORS, AND THEIR BILAYERS

A dissertation submitted in partial satisfaction
of the requirements for the degree of

DOCTOR OF PHILOSOPHY

in

PHYSICS

by

Ryan T. Van Haren

December 2023

The Dissertation of Ryan T. Van Haren is approved:

_____
Professor David Lederman, chair

_____
Professor Jairo Velasco Jr.

_____
Professor Holger Schmidt

_____
Peter Biehl
Vice Provost and Dean of Graduate Studies

Contents

List of Figures

List of Tables

Abstract

Electronic and magnetic properties of thin film transition metal fluorides, topological insulators, and their bilayers

Ryan Van Haren

Materials with long range magnetic order and strong spin-orbit coupling can exhibit unique physical phenomena when the materials are structured in novel configurations. Thin film growth via molecular beam epitaxy enables precise engineering of these materials into novel configurations by elemental doping and construction of bilayer structures.

The effect of random competing single-ion anisotropies in antiferromagnets was studied using epitaxial $Mn_xNi_{1-x}F_2$ antiferromagnetic thin film alloys. Both MnF_2 and NiF_2 have the tetragonal rutile crystal structure, but MnF_2 has an easy axis magnetic anisotropy along the c-axis of the unit cell while NiF_2 has an easy plane magnetic anisotropy perpendicular to the c-axis. Crystallographic and magnetization measurements demonstrated that the thin film alloys exhibit epitaxial strain from the MgF_2 (110) substrates, and that pure MnF_2 thin films exhibit piezomagnetic effects due to the epitaxial strain. Mean field theory is used to calculate the exchange energies of the alloy system and predict the existence of an oblique antiferromagnetic phase. Magnetization measurements show evidence of this oblique antiferromagnetic phase in addi-

tion to an emergent magnetic phase that is believed to be either a magnetic glassy phase or a helical phase.

Thin films of the topological insulator Bi_2Te_3 doped with Mn ions exhibit a spontaneous ferromagnetic moment below $T \approx 16$ K. These Mn doped Bi_2Te_3 thin films are grown on several different substrates, hexagonal Al_2O_3 (0003), tetragonal MgF_2 (110), and the tetragonal antiferromagnet NiF_2 (110), with crystallographic characterization indicating single phase growth of the Mn doped Bi_2Te_3 film regardless of substrate. Electronic transport and magnetic moment measurements show that the ferromagnetic moment of the Mn doped Bi_2Te_3 thin films is enhanced as the Fermi level moves from the bulk conduction band and towards the bulk band gap, suggesting that electronic surface states play an important role in mediating the ferromagnetic order. Mn doped Bi_2Te_3 grown on antiferromagnetic NiF_2 show evidence that the ferromagnetic moment of the Mn doped Bi_2Te_3 film is suppressed, suggesting the existence of an interface effect between the two magnetic layers.

The Fermi level of the co-doped topological insulator $(BiSb)_2Te_3$ can be tuned to lie in the bulk band gap by careful control of the (BiSb) stoichiometric ratio. Thin films of $(BiSb)_2Te_3$ are grown on both Al_2O_3 and antiferromagnetic MnF_2. Perpendicular and parallel magnetoconductance measurements are performed and fit to several models of the magnetoconductance, including comparisons of the quasi-2D Hikami-Larkin-Nagaoka model to a model derived for 2D Dirac states. The fits of experimental data to theory suggest at improved conduction through the 2D topological surface states due to the tuned Fermi level. $(BiSb)_2Te_3$-MnF_2 bilayers show evidence of enhanced magnetic scattering, suggesting the presence of magnetoelectric coupling effects at the interface.

Acknowledgments

The text of this dissertation includes reprints of the following previously published material:

R. Van Haren, T. Joshi, D. Lederman, *Physical Review Materials* **2023**, Vol 7, 3 Publisher: American Physical Society.

R. Van Haren, N. Hald, and D. Lederman, *Physical Review B* **2023**, 108, 134437 Publisher: American Physical Society

The co-author David Lederman listed in these publications directed and supervised the research which forms the basis for the dissertation.

In the first work listed above, the candidate Ryan Van Haren contributed the entirety of the work and writing with the exception of the x-ray measurements, which were performed by T. Joshi.

In the second work listed above, the candidate Ryan Van Haren contributed the entirety of the work and writing with the exception of the growth of 6 of the $Mn_xNi_{1-x}F_2$ thin films, which were grown by N. Hald.

I would like to thank my PhD dissertation reading committee, Professor Jairo Velasco Jr. and Professor Holger Schmidt for volunteering their time to scrutinize and approve my dissertation.

I would also like to thank my PhD advisor, David Lederman, for the guidance and opportunities he gave to me during my studies. From him I learned the critical skill of thinking like a scientist, and not just as a student.

I would like to thank my colleagues in the physics department and in the Lederman Lab, who were right there in the grind with me, day in and day out. As well as the talented scientists who taught and mentored me in the early days of my graduate studies, Dr. Sophie Morley and Dr. Toyanath Joshi, and showed me the example of successful researchers.

I would like to thank the Professor Nicole Herbots at Arizona State University, who gave me my first research experience when I was just an undergraduate, and my high school calculus teacher Lisa Lewandowski who encouraged me to pursue further education in math and science.

I would like to thank my friends and colleagues in Santa Cruz and abroad, for enlightening conversations about science and for countless hours of fun and many great memories.

I would like to thank my family, from whom I have felt unconditional love and have been offered all the support I could possibly need as I pursued this goal. Especially my mom and dad who have been there for me through good times and bad. I hope they recognize that my achievements are a reflection of their positive influence.

Finally I would like to thank my fiancée, Nevé, whose intelligence and adventurous spirit is a constant inspiration. Her companionship gives me the strength to tackle hard challenges and the courage to take bold new steps.

Chapter 1

Introduction

1.1 Background

1.1.1 Motivation

In many ways, the history of human civilization is a story of our ability to harness the materials at our disposal and fashion them into new and useful technologies. Great advancements in the sophistication of our cultures and societies have often been predicated on the mastery of some new material. To give just a few examples, the oldest known example of clay pottery is approximately 18,000 years old [1]. The ability to fire malleable clay into durable pottery enabled better storage of water and goods and permitted new forms of art, just as civilization was beginning to emerge into a form we would recognize today. Approximately 3,000 years ago a method to create steeled iron, which incorporates carbon into the iron metal, was developed [2]. Mastery of this new metal enabled the creation of stronger and more durable tools and buildings, and a new age of human civilization. This trend has continued up into our current age, where the discovery and mastery of semiconductor

materials has enabled the creation of a myriad of electronic devices that have transformed the way we live. Looking to the past to help predict the future it is evident that great transformative technologies will require the discovery and mastery of entirely new materials. It is this idea that motivates fundamental materials science research both generally and in the specific materials studied in this work, that studying unique physical phenomena in novel systems will add to the scientific understanding of these phenomena in a way that will enable them to be utilized in new and transformative technologies.

In the work presented here, I have studied thin films of materials that have long range magnetic order or strong spin-orbit coupling, materials that in private conversation I have colloquially referred to as "spinful", due to the fact that they possess non-trivial electronic or atomic spin structure. Specifically, I have studied the insulating antiferromagnets MnF_2, NiF_2, and their alloy $Mn_xNi_{1-x}F_2$, and the topological insulator Bi_2Te_3, both pure and when doped with the elements Mn and Sb. Materials with long range magnetic order or strong spin-orbit coupling have already found niches in modern electronics, notably in the form of hard drives and magnetic field sensors, but there are still many powerful, hypothesized devices that have yet to be realized [3]. These spintronic devices would use the spins of atoms and electrons to store data and form logic gates in place of electric current and voltage used in electronic devices. Materials with long range spin order can also form unique spin structures on the nanoscale that could be utilized in novel device architectures [4–6]. This work attempts to build on the scientific understanding of these spin based physical phenomena by constructing novel thin film geometries of magnetic and strong spin-orbit coupling materials and characterizing the unique behaviors they exhibit.

1.1.2 Ferromagnetism and antiferromagnetism

Ferromagnets, like the Mn doped Bi_2Te_3 films that will be presented in Section 4.3, have atomic magnetic moments or spins that spontaneously align with each other to all point along the same direction. A cartoon of a simple 2D ferromagnetic lattice is shown in Fig. 1.1(a), where each atom on the lattice has a local spin that aligns with its neighbors. The transition from the random spin oriented state to the ferromagnetic state occurs as a function of temperature below the Curie temperature T_C. In a crystal lattice, the spins usually have a preferred crystallographic direction in which they all point, known as the magnetic easy axis. Because each of the local atomic spins point in the same direction along the easy axis, ferromagnets generate a non-zero net magnetic moment, which can be useful in device geometries where a magnetic moment is desired without the application of an external magnetic field. Situations where this effect is utilized will be presented later in the text.

Antiferromagnets (AF), like the transition metal fluorides MnF_2, NiF_2, and their alloy $Mn_xNi_{1-x}F_2$ that will be presented in Section 3.3.2, are materials with long range magnetic order where each neighboring spin is aligned anti-parallel to its neighbors, in contrast with ferromagnets where all of the spins align parallel. A cartoon of a simple 2D AF lattice is shown in Fig. 1.1(b). The transition from the random spin oriented state to the AF state occurs as a function of temperature below the Néel temperature T_N. The spins of the AF have a preferred orientation in the crystal lattice just like in the ferromagnet, with each spin alternating between parallel and anti-parallel orientation to the easy axis, also known as the Néel vector. The critical temperature and easy axis of the AF are named after Louis Néel for his prediction of antiferromagnetic order, for which he was awarded the Nobel Prize in Physics in 1970. Unlike the ferromagnet, a perfect AF has no net magnetic moment because each local

spin is compensated by a neighboring spin with antiparallel orientation. This feature makes AF materials potentially useful in next generation spintronic devices, as they maintain long range magnetic order without the generation of stray magnetic fields, potentially enabling vastly smaller and more robust device architectures.

Because it has long range magnetic order, the AF has a preferred spin orientation, with all of the atomic spins pointing along the Néel vector, coupling anti-parallel to their neighbors. Each atomic spin contributes some magnetic moment to the material, but because each of the spins is coupled to a neighboring spin with opposite orientation, the magnetic moments sum to zero and the material has no net magnetic moment. These two properties are potentially useful in next generation devices, as the material has a preferred spin orientation that can be used for spintronic functions, and due to its net zero magnetic moment, it produces no stray magnetic fields that could affect other nearby magnetic or spintronic components. In addition to these favorable magnetic properties, AF materials can also host spin wave excitations with frequencies around 1 THz, a frequency range with useful applications that is difficult to generate with other materials [7]. Discussion of these spin wave excitations will be presented in a following section.

1.1.3 Chiral spin texture

In some magnetic materials under certain conditions, a stable twisted or whirling configuration of local spins can form. These magnetic configurations are known as chiral spin textures and are of scientific interest both as manifestations of unique topological properties and for their potential use in spintronic devices. When these twisted spin textures form at the surface of a magnetic material as a 2D structure, then they are called skyrmions, named after the theoretical

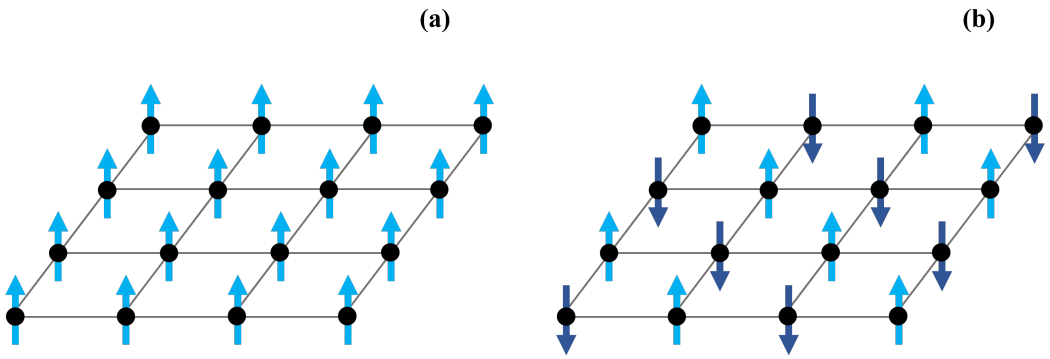

Figure 1.1: (a) Cartoon model of a 2D ferromagnet. (b) Cartoon model of a 2D antiferromagnet

physicist Tony Skyrme. These chiral spin textures can also form in the bulk of a material, where the 3D spin structures are known as Hopfions, named after the German physicist Heinz Hopf for his contributions to the field of topology.

Chiral spin textures do not seem to form in every magnetic material, but are frequently observed in systems that exhibit the Dzyaloshinskii-Moriya interaction (DMI), an anisotropic superexchange interaction present in some antiferromagnets that causes canting of the magnetic moments away from the Néel vector and manifests as a weak ferromagnetic moment perpendicular to the Néel vector [4, 5] . Phenomenologically the DMI can be expressed as an energy term in the spin Hamiltonian as $\vec{D} \cdot (\vec{S}_i \times \vec{S}_j)$ [8, 9]. The DMI, and the accompanying chiral spin textures that often form, make materials that exhibit this interaction especially interesting for magnetic studies. One such material is the antiferromagnet NiF_2 [10, 11].

Interestingly, while NiF_2 exhibits the DMI, the other antiferromagnetic transition metal fluorides with the same crystal structure as NiF_2 (specifically MnF_2, CoF_2, and FeF_2) do not exhibit the DMI. This is a result of the magnetic anisotropy of NiF_2, which has a N'eel vector that points along either the [100] or [010] crystallographic directions, while the other transition metal fluorides

named have a Néel vector that points along the [001] [10]. The presence of the DMI in NiF_2 makes it an especially interesting material to study, both alone and in alloys, for the potential to host chiral spin textures such as skyrmions or Hopfions.

1.1.4 Spin wave excitations

Spin waves are collective excitations of the spin lattice in a crystal with long range magnetic order. The quantized bosonic quasiparticle form of a spin wave is known as a magnon, and in the 1D ferromagnet the magnon has the dispersion relation

$$\hbar\omega = 4JS(1 - \cos ka), \tag{1.1}$$

where J is the exchange energy between nearest neighbors, S is the magnitude of the spin, and a is the distance between neighboring spins. The classical depiction of a spin excitation propagating across the width of a ferromagnetic materials is shown in Fig. 1.2(a).

In AF materials, where there are two sublattices with antiparallel spin orientations, there are two magnon modes that can be excited at different resonant frequencies, known as the spin up and spin down modes. A cartoon depiction of these two magnon modes is shown in Fig. 1.2(b). In MnF_2, these AF magnon modes are well studied and can be excited by the application of circularly polarized sub-terahertz microwave radiation, which generates magnon modes with sub-terahertz resonant frequency [12].

In addition to using radiation to excited spin waves, it is also possible to use a thermal gradient to generate spin waves. This process is known as the spin Seebeck effect, in analogy to the ordinary Seebeck effect where a thermal gradient generates an electric voltage across the gradient. In the

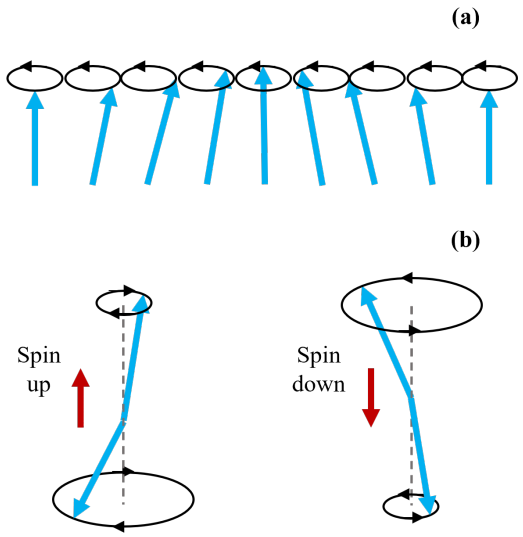

Figure 1.2: (a) Cartoon depiction of a spin wave on a 1D ferromagnetic lattice. (b) Cartoon depiction of the two types of magnon modes in an AF.

spin version, the thermal gradient in the material creates a nonequilibrium population of magnon modes across the gradient, essentially creating a magnon or spin potential difference across the material. The spin Seebeck effect has been observed in electrical insulators with at least short-range magnetic order, including in MnF_2 thin films [13].

While spectroscopy measurements can be used to detect many of these spin excitations, in order for them to be useful in spintronic devices, it is often necessary that they couple to charge carriers so they can be detected and manipulated with electric currents and voltages. In order to manifest these magnetoelectric effects, the charge carriers themselves require some non-trivial spin orientation that can couple to spin excitations in the magnetic material. The following section will introduce electrically conductive materials that have charge carriers with non-trivial spin orientations.

1.1.5 Strong spin-orbit coupling

In certain elements, coupling of an electrons spin with its orbital angular momentum will split the energy degeneracy between spin up and spin down electrons. This effect is known as spin-orbit coupling (SOC), and in materials where this effect is strong, the flow of electrons will have a preferred spin orientation due to one spin orientation being energetically favorable. This effect is most commonly seen in elements with heavy atoms, such as Pt or Bi_2Te_3, and can be used to couple electronic transport to spin interactions. When electric current flows through materials with SOC, anisotropic spin scattering mechanisms will cause the spin up and spin down electrons to gain momentum perpendicular to the direction of the current, with spin up electrons accumulating on one side of the conducting channel and spin down electrons on the other, as shown in Fig. 1.3. This is known as the spin Hall effect (SHE), in analogy to the ordinary Hall effect, where an electric voltage is generated perpendicular to the direction of current flow when the flow is perpendicular to a magnetic field [14–17]. The SHE requires no applied magnetic field, and there is no electric voltage generated across the conducting channel, only a spin voltage. In this way the SHE generates a spin polarized current at the surface of the SOC conducting channel that can couple magnetoelectrically to other spin effects.

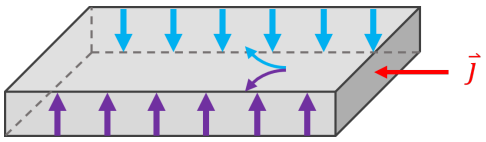

Figure 1.3: Cartoon depiction of the spin Hall effect in a non-magnetic slab.

1.1.6 Magnetoelectric coupling

In many proposed spintronic device architectures, it is necessary to couple the spin behaviors of the AF to an electric current so that the spin behaviors can be driven and measured by means of electric current and voltage. This is readily accomplished by spin polarizing the electrons in the conductor, such that there is a dominant spin orientation of the flowing electrons and a spin current is generated along with the electron current. There are several ways to create a spin polarized current, one way is to use an electrically conducting ferromagnetic material to spin polarize electrons flowing through the material. This type of technology is already utilized in modern magnetoresistive random access memory (MRAM) devices, but it has the drawback of requiring ferromagnetic conductors, which both generate and are sensitive to stray magnetic fields.

Another way to create a spin polarized current is to use a conducting material with strong SOC. In these materials the SHE will generate a spin polarized current at the surface of the conducting channel that can couple to spin excitations at the surface interface. If an atomically smooth junction is created between a material with strong SOC and an AF, then the spin current of the conducting layer can couple to the local magnetic moments in the AF, even without electric current flowing through the AF material. One way that this coupling can manifest in measurable effects is known as spin-pumping (SP), where a precessing magnetic moment or spin wave in a ferromagnet or AF will inject a spin current into a neighboring non-magnetic (NM) material. The equation describing this SP phenomenon is

$$j_{s,\mathrm{pump}}\boldsymbol{\sigma}(t) = \frac{\hbar}{4\pi} A_r \hat{\boldsymbol{m}} \times \frac{d\hat{\boldsymbol{m}}}{dt}, \tag{1.2}$$

where $j_{s,\text{pump}}$ is the magnitude of the spin current in the NM material and $\boldsymbol{\sigma}(t)$ is the polarization vector, A_r is the SP conductance of the NM, and $\hat{\boldsymbol{m}}$ is the unit vector of the magnetization in the magnetic material [18]. If the NM material has strong SOC, then it will induce an inverse spin Hall effect (ISHE) in the NM. As the name suggests, the ISHE is the reciprocal of the SHE, instead of a electric current generating a perpendicular spin current, the SP spin current induces an electric current in the NM material that can be measured externally. The ISHE is critical to these types of SP devices as it permits the detection of spin wave excitations in the magnetic material via an electric voltage. While first discovered in ferromagnetic-NM bilayers, SP and ISHE has since been observed in AF-NM bilayers as well [12].

Another method of coupling the electron spins in the conductor to the atomic spins of the AF is by an effect known as spin Hall magnetoresistance (SHMR) [19]. This is a type of magnetoresistance that develops at the interface between a magnetic material and a material with strong SOC. As electric current flows through the SOC material, a perpendicular spin current is generated due to the SHE. When the SOC material is bot interfaced with any other material, some of the spin current is reflected back at the edges of the material and adds to the electrical conductance of the material through the ISHE. When the SOC material is interfaced with a magnetic material with a magnetization vector that is collinear with the spin orientation of the spin current at the interface, then a spin back current will be generated as in the case of the free SOC conductor and the resistance is unchanged. If the orientation of the spin current at the interface with the magnetic material is perpendicular to the magnetic moments in the magnetic layer, then the spin current is absorbed at the interface in the form of a spin torque and the spin back current is reduced, thereby reducing the magnitude of the ISHE and increasing the overall

resistance. The SHMR is described by

$$\rho = \rho_0 + \rho_1(\hat{m} \cdot (\hat{j} \times \hat{z}))^2, \tag{1.3}$$

where ρ_0 is the ordinary resistivity, ρ_1 is the anisotropic resistivity amplitude, $\hat{m}$ is the magnetization orientation, $\hat{j}$ is the electric current unit vector, and $\hat{z}$ is the direction normal to the interface [18].

1.1.7 Anomalous Hall effect

In the ordinary Hall effect, an external magnetic field is applied normal to the direction of electric current in a conducting channel in order to generate a transverse electric voltage orthogonal to the magnetic field and current direction due to the Lorentz force $F = q(\vec{E} + \vec{v} \times \vec{B})$. The anomalous Hall effect (AHE) by contrast, requires no applied external magnetic field. While the AHE can be intuitively understood as a Hall effect generated by the spontaneous magnetic moment of a ferromagnetic conductor, it is actually a quantum mechanical effect that requires description of the electronic wavefunction to truly understand [20]. The physical mechanisms that generate the AHE can be divided into two types of contributions. The first type is known as the intrinsic contribution to the AHE. The intrinsic contribution arises from the Berry phase curvature that the electrons with strong SOC develop as they travel through k-space, generating an anisotropic transverse velocity. The Berry phase is discussed in more detail in section 1.2.3. The second type of contributions to the AHE are known as extrinsic contributions, which develop as a consequence of asymmetric scattering off of magnetic impurities, unlike the intrinsic contributions which develop as a consequence of the electronic band structure itself [20].

In 2D conducting systems at very low temperature and high magnetic fields,

quantum mechanical effects emerge in the ordinary Hall effect. The Hall conductance becomes quantized in integer or fractional multiples of the quantum of conductance, e^2/h, and the longitudinal resistance drops to zero as the electronic wavefunctions fill discrete orbitals known as Landau levels, in an effect known as the quantum Hall effect (QHE). This quantized Hall resistance was first observed by Klaus von Klitzing in 1980, for which he was awarded the Nobel Prize in Physics in 1985 [21, 22]. Like the ordinary Hall effect, the QHE has its own anomalous version. In the quantum anomalous Hall effect (QAHE), the quantized Hall resistance associated with Landau level filling is observed but it is done so in a ferromagnetic material without the application of an external magnetic field. Materials that exhibit the QAHE are highly desired among physicists as they permit study of this unique quantum behavior without the need of a large external magnetic field, which adds complications to the measurement.

Recently, topological insulator (TI) materials, such as Bi_2Te_3, have attracted attention in part due to their topologically protected 2D conducting surface states. In doped ferromagnetic TIs, these 2D surface states have been shown to exhibit the QAHE [23, 24]. Discussion of the topological nature of TIs in general, as well as studies of doped and undoped Bi_2Te_3 will be presented in Sections 1.2.2 and 4.3, respectively.

1.2 Theory

In order to interpret the experimental results that will be presented later in this work, it is necessary to introduce the relevant theoretical background that describes the experimental data. The following discussion will be broken into two main parts, the first part will present mean field theory expressions of long range magnetic order in mixed solid solution AFs and a derivation of the

mean field theory expression for the oblique phase of a mixed solid solution AF from the spin Hamiltonian. The second part will focus on TIs, beginning with discussion of the topological nature of the TI and followed by discussion of the models that describe the unique electronic transport in this system.

1.2.1 Mean field theory of magnetism

In the early to mid 20th century, physicists began to attempt to analytically solve the problem of long range magnetic order in ferromagnetic materials. One of the first breakthroughs in this field came with the invention of the Ising model in 1925, where magnetic sites on a lattice could be in one of two states, either spin up or spin down. While the 1D Ising model was analytically solved by Ernst Ising, the 2D and 3D Ising models proved much more difficult to directly solve, although theoretical physicist Lars Onsager would eventually analytically solve the 2D Ising model in his PhD thesis in 1944 [25]. Lars Onsager would go on to receive the Nobel Prize in Chemistry in 1968 for his contributions to the field of thermodynamics. In 3D, approximations must be made in order to mathematically describe the magnetic ordering in these lattices. One such approximation can be made by treating each individual Ising spin as interacting with a mean field that is made up of the average of the nearest neighbors to that individual Ising spin, rather than calculating the interaction between each individual lattice site, This is known as the mean field theory (MFT) approximation, and has enabled a solution to the 3D Ising model. MFT applies equally well to AF order, and can be used to describe the long range order of MnF_2, NiF_2, and the $Mn_xNi_{1-x}F_2$ alloys studied in this work, although it is important to understand the crystallographic and magnetic structure of these materials before delving into the MFT.

Structurally, MnF_2 and NiF_2 share a rutile, tetragonal $P4_2/mnm$ space group

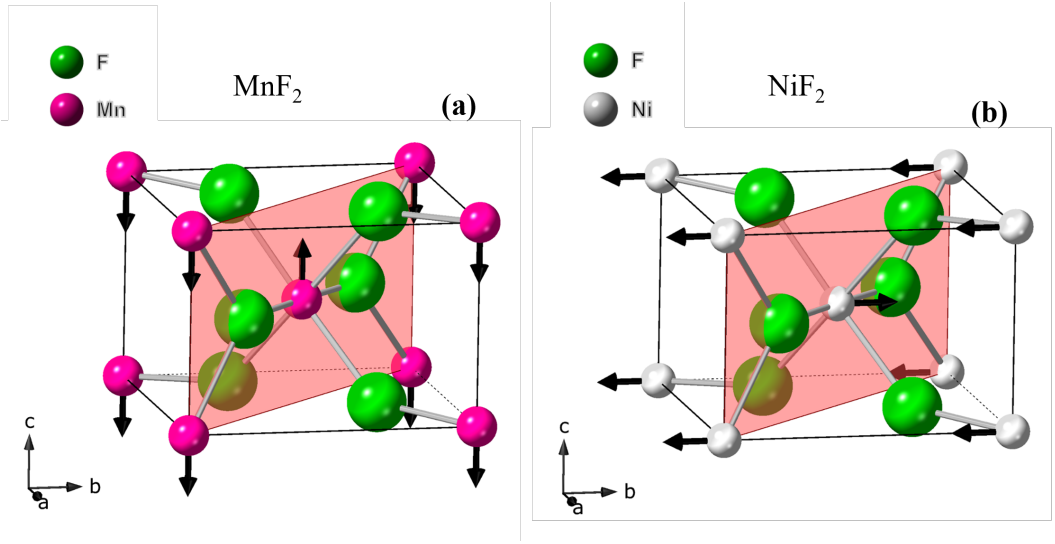

Figure 1.4: (a) Unit cell of MnF_2 with AF order shown and [110] face highlighted. (b) Unit cell of NiF_2 with AF order shown and [110] face highlighted.

crystal structure, with a Mn or Ni atom at the corners and body center of the unit cell, bonded to two F atoms. In addition, because Ni and Mn are similarly sized atoms, being only three columns apart on the periodic table, the lattice parameters of MnF_2 and NiF_2 are very similar. Both of these materials have AF order below their Néel temperatures, which are approximately 67 K and 73 K for MnF_2 and NiF_2 respectively. Below these temperatures, the corner site Mn or Ni atomic spins couple antiparallel with the body center atoms. In MnF_2, the Néel vector or easy axis along which the spins orient is the c-axis of the crystal, while in NiF_2 the Néel vector points preferentially along either the a or b-axis of the crystal, leading to easy plane antiferromagnetic order.

In zero external magnetic field, the spin Hamiltonian for MnF_2 may be written as

$$\mathcal{H} = \sum_{l=1}^{3} \sum_{\langle k-\delta_l \rangle} J_l \vec{S}_k \cdot \vec{S}_{k+\delta_l} + \sum_{i}^{N/2} D(S_i^z)^2 + \sum_{j}^{N/2} D(S_j^z)^2, \tag{1.4}$$

where l denotes the different types of neighbors; $l = 1$ refers to neighboring spins between the corner and body-center sites, $l = 2$ refers to neighbor spins

along the c-axis, and $l = 3$ refers to neighbor spins along the a and b axes; the sum over $\langle k - \delta_l \rangle$ denotes pairs of neighboring spins k and $k + \delta_l$ of type l, each pair counted only once; J_l represents the exchange coupling constants between ions of neighbor type l; D represents the magnetic anisotropy energy with respect to the direction z, summed over every lattice site i on each sublattice 1, and every lattice site j on sublattice 2; $S^z_{i,j}$ is defined as $S^z_{i,j} = \vec{S}_{i,j} \cdot \hat{z}$, and therefore represents the magnitude of the z component of the spin vector at site i or j. This Hamiltonian can be simplified by omitting the J_2 and J_3 terms because they are each an order of magnitude smaller in energy than the J_1 term

$$\mathcal{H} = \sum_{\langle k-\delta_1 \rangle} J_1 \vec{S}_k \cdot \vec{S}_{k+\delta_1} + \sum_{i}^{N/2} D(S^z_i)^2 + \sum_{j}^{N/2} D(S^z_j)^2. \tag{1.5}$$

Because the exchange term J_1 describes interactions only between the next-nearest neighbors on opposite sublattices, the sum can be expressed in terms of i and j,

$$\mathcal{H} = \sum_{i}^{N/2} \sum_{j \in \mathrm{nn}(i)} J_1 \vec{S}_i \cdot \vec{S}_j + \sum_{i}^{N/2} D(S^z_i)^2 + \sum_{j}^{N/2} D(S^z_j)^2, \tag{1.6}$$

where the sum over i counts all the lattice sites on sublattice 1, and the sum over $j \in \mathrm{nn}(i)$ counts all the j sites that are next nearest neighbors of i. Summing over pairs in only one sublattice will count all the pairs in the entire system without double counting. Because the interaction $J_1 \vec{S}_i \cdot \vec{S}_j$ is symmetric between the two sublattices, it makes no difference whether the sum is over i or j. A mean-field type expression can be used to simplify this expression by defining the spin at an arbitrary lattice site as the expectation value of the spin plus some fluctuations about that expectation value by using,

$$\vec{S}_{i,j} = \langle \vec{S}_{i,j} \rangle + \delta \vec{S}_{i,j}. \tag{1.7}$$

Then the first term in the spin Hamiltonian can be decoupled in the following manner

$$\begin{aligned}&\sum_{i}^{N/2}\sum_{j\in\mathrm{nn}(i)} J(\langle\vec{S}_i\rangle+\delta\vec{S}_i)\cdot(\langle\vec{S}_j\rangle+\delta\vec{S}_j)\\ =&\sum_{i}^{N/2}\sum_{j\in\mathrm{nn}(i)} J(\langle\vec{S}_i\rangle\cdot\langle\vec{S}_j\rangle+\langle\vec{S}_i\rangle\cdot\delta\vec{S}_j+\delta\vec{S}_i\cdot\langle\vec{S}_j\rangle+\delta\vec{S}_i\cdot\delta\vec{S}_j),\end{aligned} \tag{1.8}$$

where $J = J_1$ for brevity. At low temperatures, the spin fluctuations $\delta\vec{S}_{i,j}$ are very small such that $\delta\vec{S}_i \cdot \delta\vec{S}_j = 0$. Because the two sublattices are antiferromagnetically coupled, the magnitude of the expectation value of the spin is identical regardless of the site, but the direction is reversed between opposite sublattices, and the average magnetization vector at each lattice site can be expressed as

$$\vec{m}_1 = \langle\vec{S}_i\rangle = -\vec{m}_2 = -\langle\vec{S}_j\rangle. \tag{1.9}$$

The first term of the spin Hamiltonian can then be written as

$$\begin{aligned}&\sum_{i}^{N/2}\sum_{j\in\mathrm{nn}(i)} J(\langle\vec{S}_i\rangle\cdot\langle\vec{S}_j\rangle+\langle\vec{S}_i\rangle\cdot(\vec{S}_j-\langle\vec{S}_j\rangle)+(\vec{S}_i-\langle\vec{S}_i\rangle)\cdot\langle\vec{S}_j\rangle)\\ =J&\sum_{i}^{N/2}\sum_{j\in\mathrm{nn}(i)} (\vec{m}_2\cdot\vec{m}_1+\vec{m}_1\cdot\vec{S}_j-\vec{m}_2\cdot\vec{m}_1+\vec{m}_2\cdot\vec{S}_i-\vec{m}_2\cdot\vec{m}_1)\\ =J&\sum_{i}^{N/2}\sum_{j\in\mathrm{nn}(i)} (-\vec{m}_2\cdot\vec{m}_1+\vec{m}_2\cdot\vec{S}_i+\vec{m}_2\cdot\vec{S}_i)\\ =Jq&\sum_{i}^{N/2}\vec{m}_2\cdot(2\vec{S}_i-\vec{m}_1),\end{aligned} \tag{1.10}$$

where the definition $\delta\vec{S}_{i,j} = \vec{S}_{i,j} - \langle\vec{S}_{i,j}\rangle$ was used in the first line and $\vec{m}_1 \cdot \vec{S}_j = \vec{m}_2 \cdot \vec{S}_i$ was used to simplify the expression. Without any explicit j dependence in the sum, the sum over next-nearest neighbors can be expressed as the total number of next-nearest neighbors q. A similar method can be used for the

anisotropy term of the spin Hamiltonian

$$\begin{aligned}
&\sum_i^{N/2} D(S_i^z)^2 + \sum_j^{N/2} D(S_j^z)^2 = D\sum_i^{N/2}(\langle S_i^z\rangle + \delta S_i^z)^2 + D\sum_j^{N/2}(\langle S_j^z\rangle + \delta S_j^z)^2 \\
&= D\sum_i^{N/2} m_1^z(2S_i^z - m_1^z) + D\sum_j^{N/2} m_2^z(2S_j^z - m_2^z) \\
&= D\sum_i^{N/2} m_1^z(2S_i^z - m_1^z) + D\sum_i^{N/2} -m_1^z(-2S_i^z + m_1^z) \\
&= 2D\sum_i^{N/2} m_1^z(2S_i^z - m_1^z),
\end{aligned} \tag{1.11}$$

where the symmetry of the system $\sum_i S_i^z = -\sum_j S_j^z$ was used to express everything in terms of sublattice 1, and $m_z = \langle S_i^z\rangle = \langle \vec{S}_i\rangle \cdot \hat{z} = \vec{m}\cdot\hat{z}$. The spin Hamiltonian in zero external magnetic field then becomes

$$\mathcal{H} = Jq\sum_i^{N/2} \vec{m}_2 \cdot (2\vec{S}_i - \vec{m}_1) + 2D\sum_i^{N/2} m_1^z(2S_i^z - m_1^z). \tag{1.12}$$

This Hamiltonian can be rewritten in terms of an effective field acting on the spin at lattice site i as

$$\begin{aligned}
\mathcal{H} &= Jq\sum_i^{N/2} \vec{m}_2 \cdot (2\vec{S}_i - \vec{m}_1) + 2D\sum_i^{N/2} m_1^z(2S_i^z - m_1^z) \\
&= Jq\sum_i^{N/2} (\vec{m}_2 \cdot 2\vec{S}_i - \vec{m}_2\cdot\vec{m}_1) + 2D\sum_i^{N/2}(2m_1^z S_i^z - (m_1^z)^2) \\
&= J\frac{N}{2}qm^2 + Jq\sum_i^{N/2} 2\vec{m}_2\cdot\vec{S}_i - 2D\frac{N}{2}(m_1^z)^2 + 2D\sum_i^{N/2} 2m_1^z S_i^z \\
&= (\frac{1}{2}JNqm^2 - DN(m_1^z)^2) + (2Jq\vec{m}_2\cdot\sum_i^{N/2}\vec{S}_i + 4Dm_1^z\hat{z}\cdot\sum_i^{N/2}\vec{S}_i),
\end{aligned} \tag{1.13}$$

where q is the number of nearest corner to body center site neighbors, which is equal to 8 for the rutile crystal structure of MnF_2. The effective field acting

on the spin at lattice site i is then

$$\vec{h}_{\text{eff}} = 2Jq\vec{m}_2 + 4Dm_1^z\hat{z}. \tag{1.14}$$

Up until this point, the system has been treated as only having one type of magnetic ion, but the effective field can be modified for a solid solution where the mean-field acting on the spin of ion P at lattice site i has contributions from two types of ions A and B

$$\vec{h}_P = 2\sum_{Q=A,B}(J_{PQ}q_Q\vec{m}_{Q,2}) + 4D_P m_{P,1}^z\hat{z} = 2\sum_{Q=A,B}(J_{PQ}q_Q\langle\vec{S}_{Q,2}\rangle) + 4D_P(\langle\vec{S}_{P,1}\rangle\cdot\hat{z})\hat{z} \tag{1.15}$$

where the single-ion anisotropy term is omitted from the sum over Q because it only depends on the single ion at site i and has no interactions with its neighbors. The effective field is further simplified by making the mean-field assumption that the spins can only lie in the y-z plane [26]. Then the effective field can be split into y and z contributions

$$\begin{aligned}
\vec{h}_P &= 2\sum_{Q=A,B}(J_{PQ}q_Q\langle\vec{S}_{Q,2}\rangle\cdot\hat{y})\hat{y} + \left(2\sum_{Q=A,B}(J_{PQ}q_Q\langle\vec{S}_{Q,2}\rangle\cdot\hat{z}) + 4D_P(\langle\vec{S}_{P,1}\rangle\cdot\hat{z})\right)\hat{z} \\
&= 2\sum_{Q=A,B}(-J_{PQ}q_Q S_Q\sin\theta_Q)\hat{y} + \left(2\sum_{Q=A,B}(-J_{PQ}q_Q S_Q\cos\theta_Q) + 4D_P S_P\cos\theta_P\right)\hat{z} \\
&= Y_P\hat{y} + Z_P\hat{z}.
\end{aligned} \tag{1.16}$$

The term q_Q, the number of nearest neighbors of ion type Q, can be expressed as $q_Q = qp_Q$, where p_Q is the stoichiometric percentage of ions of type Q in the solid solution. The angle θ_P that the ion P on lattice site i makes with

respect to the z axis is given by

$$\tan(\theta_P) = \frac{Y_P}{Z_P}. \tag{1.17}$$

Then the equation for the tangent of the angle of an ion of type A is

$$\tan\theta_A = \frac{-q(J_{AA}p_A S_A \sin\theta_A + J_{AB}p_B S_B \sin\theta_B)}{-q(J_{AA}p_A S_A \cos\theta_A + J_{AB}p_B S_B \cos\theta_B) + 2D_A S_A \cos\theta_A} \tag{1.18}$$

And similarly for ion B:

$$\tan\theta_B = \frac{-q(J_{BB}p_B S_B \sin\theta_B + J_{AB}p_A S_A \sin\theta_A)}{-q(J_{BB}p_B S_B \cos\theta_B + J_{AB}p_A S_A \cos\theta_A) + 2D_B S_B \cos\theta_B}. \tag{1.19}$$

In 1969, G. K. Wertheim *et al* developed a MFT model for the transition temperature of a mixed solid solution AF, the expression for the transition temperature is [27]

$$T_N(x) = [p_A T_A + p_B T_B]/2 + \left(\frac{1}{4}[p_A T_A + p_B T)_B]^2 + p_A p_B (T_{AB}^2 - T_A T_B)\right)^{1/2}, \tag{1.20}$$

where T_A and T_B are the transition temperatures of the pure systems, and p_A and p_B represent the relative stoichiometries of the two mixed systems. Fitting the measured transition temperatures to this equation yields a value for T_{AB} which can then be used to calculate the exchange integral J_{AB} between the elements of the mixed system, according to the expression

$$|J_{AB}| = \frac{3k_B T_{AB}}{16[S_A(S_A+1)S_B(S_B+1)]^{1/2}}, \tag{1.21}$$

where S_A and S_B are the spin values for the magnetic elements.

1.2.2 Topological insulators

Topology refers to the mathematical study of objects that are insensitive to smooth, continuous deformations. The objects involved can take many different forms, but the simplest elucidating case may be found in considering a sphere and a donut. One can imagine taking a sphere of clay and smoothly deforming it into several other shapes: a disk, a cylinder, a cube, but it cannot be shaped into a donut without puncturing its surface or combining two ends together, two kinds of discontinuous changes. Likewise, a donut can be smoothly deformed into other shapes, even a coffee mug, but cannot be transformed into a sphere without some discontinuous change. In geometric topology, the sphere and the donut are distinctly defined by the genus g, which can be naively understood as the number of holes the object has.

The concept of topology can be applied to the electronic band structure of crystalline solids, but instead of deforming the shape of a geometric object, the deformations here refer to adiabatic changes of the Hamiltonian describing the band structure of a crystal. Just as the sphere and the donut are topologically distinct from one another, so too are certain materials topologically distinct from one another. Their electronic band structures cannot be adiabatically transformed into one another. To do so would require a discontinuous phase change. In this way, electrical insulators can be generally split into two topologically distinct categories defined by the $\mathbb{Z}_2$ invariant, the calculation of which is a topic of study unto itself [28–30]. When this value is even, the system is an ordinary insulator, but when it is an odd value, the system is a topological insulator (TI), with unique properties that result from this topological distinction.

The 3D TI is distinguished from its trivial insulator counterpart by the presence of topologically protected 2D electronic surface states. In momentum

space, these surface states exist in the bulk band gap between the conduction and valence bands, where they form an odd number of Dirac cones, as shown in Fig. 1.5. The topological protection of these surface states comes as a consequence of Kramer's theorem, which prohibits time-reversal-symmetric perturbations, such as electrically charged defects, from scattering a spin 1/2 particle, electrons in this case, into its time reversed conjugate, or Kramers pair. In a trivial insulator with an even number of Kramers pairs, the electrons are able to scatter into time reversed conjugates belonging to another Kramers pair, leading to total localization of the states. In a TI, the odd number of Kramers pairs means that there will always be at least one pair that is preserved because it is protected from scattering into its own time reversed conjugate except by mechanisms that break time reversal symmetry [31]. In addition to robust, protected electronic surface states, the topology of the TI requires that the edge states, in the case of a 3D TI these are the 2D surface states, described by the Dirac Hamiltonian

$$\mathcal{H} = \hbar\nu_F(k_x\sigma_y - k_y\sigma_x), \tag{1.22}$$

where ν_F is the Fermi velocity, and $\sigma_{x,y}$ represent spin matrices. The Dirac nature of these surface states endows them with two unique properties, one being a linear dispersion relation ($E \propto k$) and the other being spin momentum locking ($k_x\sigma_y$, $k_y\sigma_x$) where the spin of the charge carrier is always orthogonal to the momentum of the charge carrier. Notably, an energy gap can be opened at the Dirac point (where the conduction and valence bands meet) by applying an external magnetic field or inducing a ferromagnetic moment and breaking time reversal symmetry in the state. These characteristics result in several interesting properties of the 3D TI for research and device applications, among them electrically conducting surface states with very long coherence lengths due to

protection from time-reversal-invariant backscattering, photon-like relativistic electron transport, and the generation of spin currents from spin-momentum locking in the surface states.

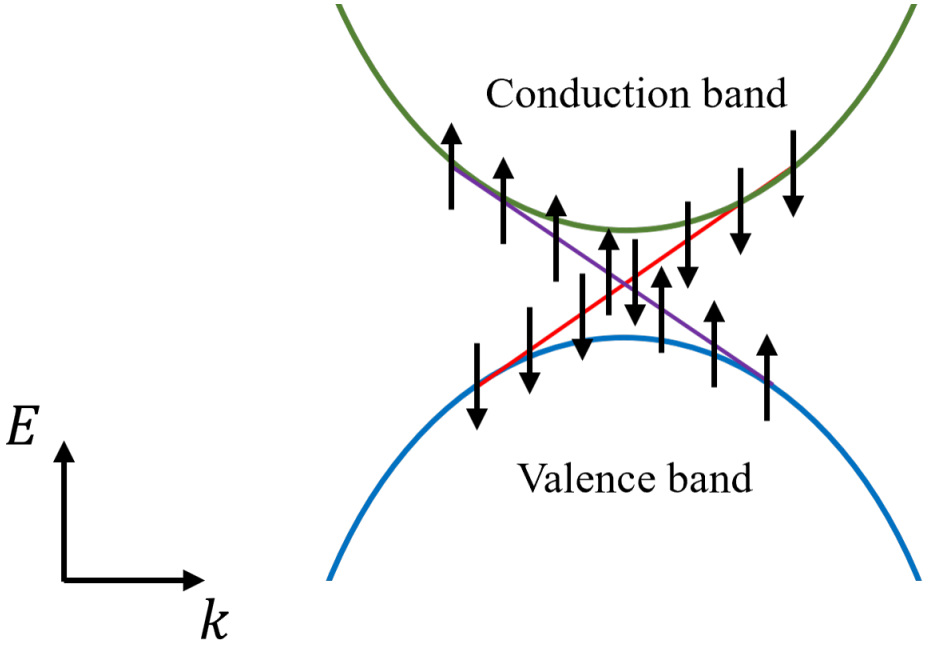

Figure 1.5: Cartoon diagram of 3D TI band structure (projected onto a 2D plane) near the bulk band gap.

1.2.3 Magnetoconduction

There is an interesting phenomenon that develops in the electronic transport of 2D or quasi-2D systems at low temperatures as a function of the magnetic field applied normal to the conducting surface and the direction of current flow. Depending on the system, there will either be a positive or negative magnetoconductance cusp near zero applied magnetic field, in contrast to the expected magnetoconductance for ordinary metals that goes approximately as $-B^2$. These changes to the magnetoconductance are due to quantum localization effects of the electrons as they scatter off of impurities in the sample. In the case of negative contributions to the magnetoconductance, the effect is

known as weak localization (WL), while positive contributions to the magnetoconductance are known as weak antilocalization (WAL). The origin of these effects comes from the accumulation of a Berry phase in the wavefunction of the electrons as they scatter. Consider an electron that takes a closed path in parameter space as it scatters. Assuming the electron stays in the adiabatic approximation, meaning that its Hamiltonian changes sufficiently slowly with time that there is no transition to another energy eigenstate, then the final wavefunction can be described by its initial state plus an accumulated Berry phase [31]

$$|\psi(t_f)\rangle = e^{-(i/\hbar)\int_{t_i}^{t_f} E(t')dt'} e^{i\gamma} |\psi(t_i)\rangle, \tag{1.23}$$

where γ is the Berry phase.

Equation 1.23 describes the Berry phase in terms of the time evolution of the energy eigenvalue as the electron travels around a closed path, but the Berry phase can also be expressed as a time independent integral over a path in parameter ($\boldsymbol{\lambda}$) space

$$\gamma = i \oint \langle \psi(\boldsymbol{\lambda}) | \nabla_\lambda | \psi(\boldsymbol{\lambda}) \rangle \cdot d\boldsymbol{\lambda}. \tag{1.24}$$

This accumulated Berry phase is responsible for the two types of localization effects observed in 2D transport. In systems that lack strong SOC, backscattering electrons will constructively interfere with themselves and the rate of backscattering will increase, causing a decrease in the magnetoconductance. In systems with strong SOC, the accumulated Berry phase causes the electrons to destructively interfere with themselves and the backscattering channel is suppressed, resulting in enhanced magnetoconductance. The application of an external magnetic field causes an additional phase to be accumulated as the electrons travel a closed loop and therefore destroys the localization behav-

iors, and if the electron wavefunction coherence length is not long enough to make it around the closed loop before it decoheres then the localization effect will not present. These are the reasons that the effect is only observed at low temperatures, where coherence lengths are longest, and small or zero magnetic fields.

In 1980 the Hikami-Larkin-Nagaoka (HLN) model was developed to describe the quantum correction to the magnetoconductivity of a quasi-2D system near zero applied magnetic field [32, 33]

$$\Delta\sigma = -\frac{\alpha e^2}{\pi h}\left[\ln\frac{\hbar}{4el_\phi^2 B} - \psi\left(\frac{1}{2}+\frac{\hbar}{4el_\phi^2 B}\right)\right], \tag{1.25}$$

where ψ is the digamma function, l_ϕ is the phase coherence length, and α is a dimensionless parameter that describes the type of localization occurring and nominally takes on one of three possible values: $\alpha = 1$ is known as the orthogonal case that occurs when there is no SOC and no magnetic scattering, weak localization occurs in the orthogonal case. $\alpha = 0$ is the unitary case where there are no localization effects and the change to the ordinary magnetoconductivity is zero. $\alpha = -1/2$ is the symplectic case and corresponds to strong SOC and no magnetic scattering, weak antilocalization occurs in the symplectic case. It is worth noting that in 2D transport, the electrical conductivity, defined as $\sigma = \frac{1}{R}\frac{l}{wt}$, has the same units as the electrical conductance, defined as $G = \frac{1}{R}$ because there is no channel thickness t in a 2D film.

The HLN model is commonly utilized to describe the magnetoconductivity and localization effects of TI materials, but it is not perfectly accurate to the physics of the TI surface states. The HLN model describes quasi-2D scattering in a system of electrons that have a parabolic dispersion relation (the energy is proportional to the square of the momentum p^2). These qualities differ from

those present in the surface states of a TI, where the conducting surface states are truly 2D and are described by the Dirac Hamiltonian, which causes the electrons to have a linear dispersion relation (the energy is directly proportional to the momentum p). Theoretical work by P. Adroguer et al. sought to solve for the localization effects for the 2D Dirac states present in the TI surface states, as described in the following paragraph [34].

The Dirac Hamiltonian for the 2D surface states of a TI with both scalar and spin-orbit scatterers can be expressed as

$$\mathcal{H} = \hbar\nu_F(k_x\sigma_x - k_y\sigma_y) + V(\vec{k}, \vec{k'}), \tag{1.26}$$

where ν_F is the Fermi velocity and $\sigma_{x,y}$ are Pauli matrices. The disorder potential $V(\vec{k}, \vec{k'})$ is defined as

$$V(\vec{k}, \vec{k'}) = U \sum_I e^{-i(\vec{k}-\vec{k'})\cdot\vec{R}_I}[\mathbb{1} + i\lambda(\vec{k} \times \vec{k'}) \cdot \vec{\sigma}], \tag{1.27}$$

where $\vec{R}_I$ represents the locations of impurities, $\mathbb{1}$ represents a 2×2 identity matrix in spin space. Solving for the magnetoconductivity corrections near zero applied field, they found that the 2D Dirac states always belong to the symplectic symmetry class, corresponding to WAL and $\alpha = -0.5$ in the HLN model, regardless of the spin-orbit scattering strength. This prediction matches the observed behavior of non-magnetic TIs, where WAL is always present, but it fails to capture the behavior of doped magnetic TIs, where there is often a suppression of WAL or even a crossover to WL [35]. The failure of this theory to describe the symmetry class of the surface states in the magnetic TI is due to the fact that the spontaneous moment in these materials breaks time reversal symmetry and opens an energy gap at the Dirac point, even at zero applied external field. Therefore the Dirac Hamiltonian no longer properly describes

the behavior of the system and the localization phenomenon deviates from the predicted symplectic symmetry class. In any case, this model is still useful for describing the 2D states in the non-magnetic TI. The magnetoconductivity correction has contributions from three different propagation modes, and are expressed as

$$\delta\sigma(B) = \frac{e^2}{\pi h} \ln \frac{\tau_\phi}{\tau_e} \sum_{i=1}^{3} a_i w_i g_i(B), \tag{1.28}$$

where

$$\begin{aligned} a_1 w_1 g_1(B) = &\left[\left(\frac{1}{2} - \tilde{\lambda} + \frac{3}{2}\tilde{\lambda}^2 \right) / \ln \frac{\tau_\phi}{\tau_e} \right] \times \\ &\left[\psi \left(\frac{1}{2} + \frac{\hbar(1+\frac{1}{2}\tilde{\lambda}^2)}{4\nu_F^2 \tau_e^2 B} \right) - \psi \left(\frac{1}{2} + \frac{\hbar(1+\frac{1}{2}\tilde{\lambda}^2)}{4\nu_F^2 \tau_e \tau_\phi B} \right) \right], \end{aligned} \tag{1.29}$$

$$\begin{aligned} a_2 w_2 g_2(B) = &\left[\left(\tilde{\lambda} - 2\tilde{\lambda}^2 \right) / \ln \frac{\tau_\phi}{\tau_e} \right] \times \\ &\left[\psi \left(\frac{1}{2} + \frac{\hbar\tilde{\lambda}}{8\nu_F^2 \tau_e^2 B} \right) - \psi \left(\frac{1}{2} + \frac{\hbar\tilde{\lambda}}{8\nu_F^2 \tau_e \tau_\phi B} \right) \right], \end{aligned} \tag{1.30}$$

$$\begin{aligned} a_3 w_3 g_3(B) = &\left[\frac{1}{2}\tilde{\lambda}^2 / \ln \frac{\tau_\phi}{\tau_e} \right] \times \\ &\left[\psi \left(\frac{1}{2} + \frac{\hbar\tilde{\lambda}^2}{8\nu_F^2 \tau_e^2 B} \right) - \psi \left(\frac{1}{2} + \frac{\hbar\tilde{\lambda}^2}{8\nu_F^2 \tau_e \tau_\phi B} \right) \right], \end{aligned} \tag{1.31}$$

and where τ_ϕ and τ_e represent the spin-orbit and elastic scattering times respectively, $\tilde{\lambda}$ represents the relative strength of the scalar and spin-orbit coupled disorder, and ν_F represents the Fermi velocity. The spin-orbit scattering time τ_ϕ is the time between electron scattering events that cause the phase of the electron wavefunction to decohere. In this way it is related to the phase coherence length l_ϕ, the distance the electron travels before it decoheres, by the Fermi veloctiy ν_F, the speed that electrons at the Fermi surface are moving, by the expression $l_\phi = \nu_F \tau_\phi$.

Quantum corrections to the magnetoconductivity can also develop as a function of an external magnetic field applied parallel to the direction of current flow. In the early 1980s, Al'tshuler and Aronov calculated the low temperature magnetoconductivity in this configuration to be

$$\Delta\sigma = \frac{-1}{2\pi} \ln\left(1 + \frac{4\pi^2 a^2 l_\phi^2 H^2}{12\Phi^2}\right), \tag{1.32}$$

where a is the thickness of the film and Φ is the magnetic flux quantum, with the stipulation that the film thickness a is small in comparison with the phase coherence length l_ϕ [36–38].

The phase coherence length l_ϕ is particularly useful for determining the dimensionality of the charge transport. When measured as a function of temperature, the phase coherence length has the following dependence [39]

$$l_\phi = (D\tau_\phi)^{1/2} \propto T^{-d/4}, \tag{1.33}$$

where D is the diffusion coefficient and d is the dimensionality of the charge transport.

These quantum corrections to the 2D magnetoconductivity manifest only at "weak" applied magnetic fields. The strength of the magnetic field in this context is related to the parameters of the thin film sample itself, where the field ceases to be weak when the magnetic length becomes shorter than the phase coherence length. The expressions describing this cut-off for a magnetic field applied parallel to the plane and perpendicular to the plane are given in CGS units as [36]

$$H_{\text{par}} \geq \frac{c\hbar}{2eal_\phi}, \tag{1.34}$$

and

$$H_{\text{perp}} \geq \frac{c\hbar}{2el_{\phi}^2}. \tag{1.35}$$

1.2.4 Electron-electron interactions

At room temperature, electron scattering processes in conductors are dominated by electron-phonon interactions due to the large population of excited phonon modes commonly present in materials at this temperature. As the temperature of the conductor decreases, these phonon modes begin to freeze out, having insufficient thermal energy in the lattice. The freezing out of these phonon modes is the reason that, in general, the conductivity of conductors increases as the temperature decreases, as there are fewer phonons for the conducting electrons to scatter off of. At very low temperatures, below a tenth of the Debye temperature, the population of phonons is very low and almost no electron-phonon scattering takes place. In 1980, B.L. Al'tshuler, A.G. Aronov and P.A. Lee addressed the theoretical problem of electron-electron interactions in a disordered 2D conductor [40]. The result is a correction to the conductivity as a function of temperature

$$\delta\sigma = \frac{e^2}{4\pi^2\hbar}(2 - 2F)\ln(k_B T\tau/\hbar), \tag{1.36}$$

where F is the averaged screened Coulomb interaction and τ is the electron relaxation time related to the free mean path and Fermi velocity. This theory is borne out in experimental observations of electrical conductivity in 2D systems, which exhibit logarithmic decreases in the conductivity at low temperatures (roughly 10 to 20 K).

As discussed earlier, at low temperatures electron localization effects also come into play, therefore any accurate theoretical description of the conductivity

must account for electron-electron interaction effects that decrease the conductivity, and localization effects that may increase (in the case of WAL) or decrease the conductivity (in the case of WL). Accounting for these effects, the temperature dependent correction to the conductivity can be expressed as

$$\Delta\sigma(T) = \sigma(T) - \sigma(T_0) = \frac{e^2}{2\pi^2\hbar}\alpha p \ln(\frac{T}{T_0}) + \frac{e^2}{4\pi^2\hbar}(2-2F)\ln(k_B T\tau/\hbar), \quad (1.37)$$

where α is the same dimensionless parameter from Eq. 1.25, p is another dimensionless parameter that depends on the dominant collision mechanism. [41]. This expression for the quantum conductivity corrections can be particularly useful characterizing transport in a 2D film in a small and large applied magnetic field, as in a large field $\alpha = 0$ and only the second term applies, while in a small magnetic field both terms will contribute to the conductivity.

Chapter 2

Experimental methods

2.1 Molecular beam epitaxy

The thin film crystals studied in this work were grown with a technique known as molecular beam epitaxy (MBE). In this process, pockets containing solid, high purity source material (for example, Bi, Te, or MnF_2, often in the form of powders or pellets), are heated until the solid source material begins to sublimate, where individual atoms or molecules transition directly from the solid phase to the gas phase without transition to the liquid phase. This process takes place in an ultra high vacuum (UHV) chamber at pressures below 1×10^{-8} Torr (for reference, air pressure at sea level on Earth is 760 Torr), which serves to both reduce the amount of contaminants in the growth chamber and cause the sublimated source material to travel ballistically (without significant scattering and broadening) in a molecular beam. The molecular beam of sublimated source material is directed at a substrate crystal, which is a specially chosen crystal on which the thin film is grown. As the molecular beam encounters the substrate crystal, the atoms and molecules adsorb onto the substrate surface and feel atomic forces associated with the struc-

ture of the substrate crystal lattice. In order to minimize the free energy at the interface between the substrate and the growing thin film, the adsorbed atoms and molecules will tend to grow in a crystal lattice that matches the structure of the substrate crystal lattice. For example, a molecular beam of MnF_2 molecules adsorbed onto a tetragonal MgF_2 (110) substrate will grow as a thin film with tetragonal crystal structure in the (110) orientation. This phenomenon is known as epitaxial growth. The substrate crystal is usually heated to some elevated temperature during the growth process, in order to endow the adsorbed atoms and molecules with enough thermal energy to be sufficiently mobile to find the lowest energy crystallographic state. A cartoon diagram of the MBE growth chamber is shown in Fig. 2.1.

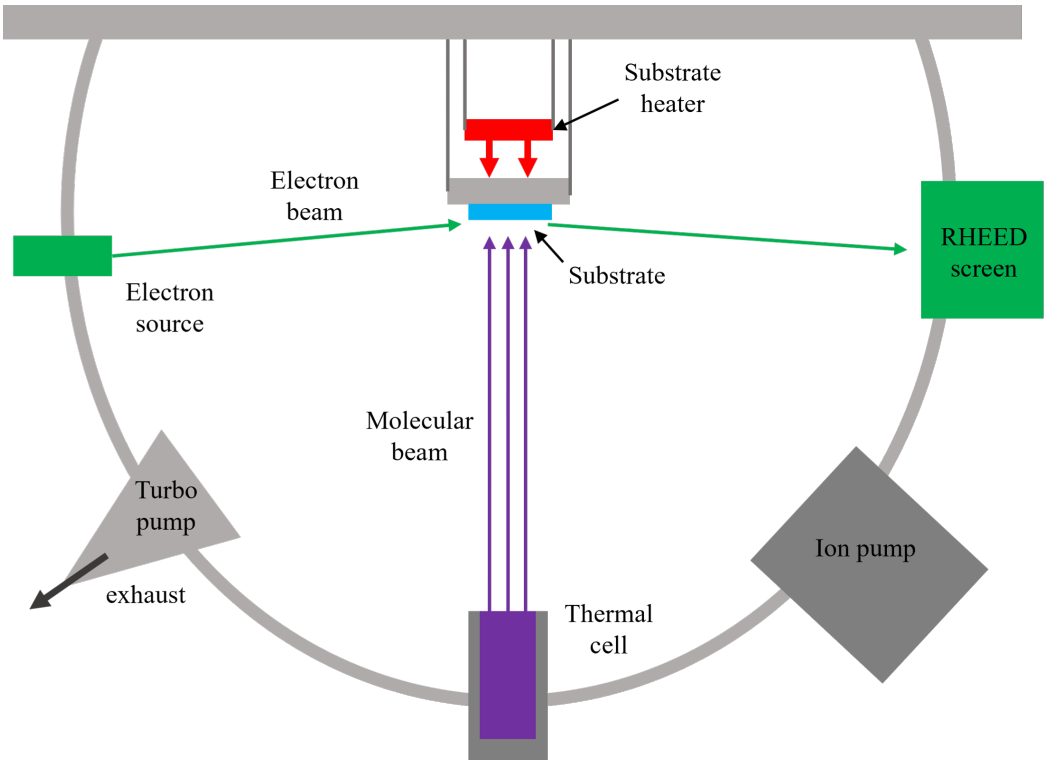

Figure 2.1: Cartoon diagram of MBE growth chamber.

In order to reach UHV pressures, the growth chamber must be kept isolated from the atmosphere as much as possible. In order to load and remove substrates from the growth chamber, a separate load lock chamber is used. The

load lock chamber is rated for higher high vacuum pressures (below 1×10^{-5} Torr), has a gate valve to isolate it from the growth chamber and a door that allows it to be opened to atmosphere to load and remove samples. To pump the load lock chamber down from atmospheric pressure (760 Torr) to high vacuum, a roughing pump (often a scroll or rotary vein pump) is first used to pump the chamber down to the millitorr range, at which point a high vacuum pump (usually a turbo pump, but possibly an ion pump) is used to reduce the pressure into the high vacuum range. Once the pressure difference between the two chambers is less than 1×10^{-3} Torr, the gate valve between the chambers is opened and a manual or automatic transfer arm is used to move the sample between the chambers. The ballistic nature of the molecular beams at UHV pressures can be shown with a simple calculation of the mean free path of a particle before it collides with another particle. Consider the mean free path l of a particle of radius r traveling through a volume V filled with N number of point-like particles [42],

$$l = \frac{1}{4\pi r^2}\frac{V}{N}. \tag{2.1}$$

In order to calculate the mean free path of a particle in a UHV chamber, we will use the ideal gas law and solve for the number of moles at UHV conditions,

$$\begin{aligned} PV &= NkT \\ \frac{N}{V} &= \frac{P}{kT} \\ \frac{N}{V} &= \frac{133 \times 10^{-9}\,\mathrm{Pa}}{(1.38 \times 10^{-23}\,\mathrm{m^2\,kg\,s^{-2}\,K^{-1}}) \times (293\,\mathrm{K})} \\ \frac{N}{V} &= 0.329 \times 10^{14}\,\mathrm{particles/m^3} \\ \frac{V}{N} &= 3.04 \times 10^{-14}\,\mathrm{m^3/particle}. \end{aligned} \tag{2.2}$$

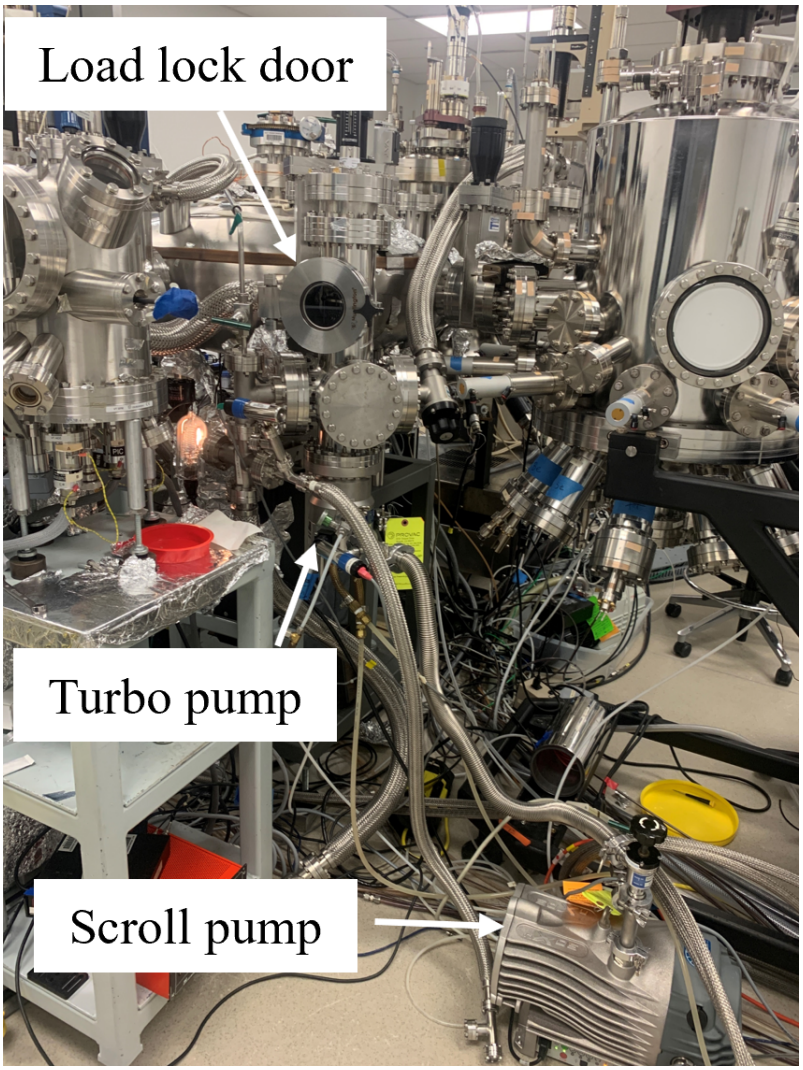

Figure 2.2: Picture of MBE system load lock chamber in the Lederman Lab at UCSC.

Then using equation 2.1 and an approximate radius for our molecule of 0.5 angstroms,

$$l = 967\,\text{km}. \tag{2.3}$$

Therefore individual atoms in a molecular beam can travel distances vastly larger than the length of the growth chamber before scattering off of other atoms.

The source cells used in MBE are often thermal cells that use a conducting

coil to generate heat and raise the source temperature well above 1,000 K in high temperature models. For some applications, depositing Pt for example, a directed electron beam is used to heat the source material as the electrons impart a large amount of kinetic energy into the material. In some of these processes the source material actually melts and the molecular beam is generated from evaporation instead of sublimation. An image of one of the MBE growth chambers in the Lederman Lab at UCSC is shown in Fig. 2.3.

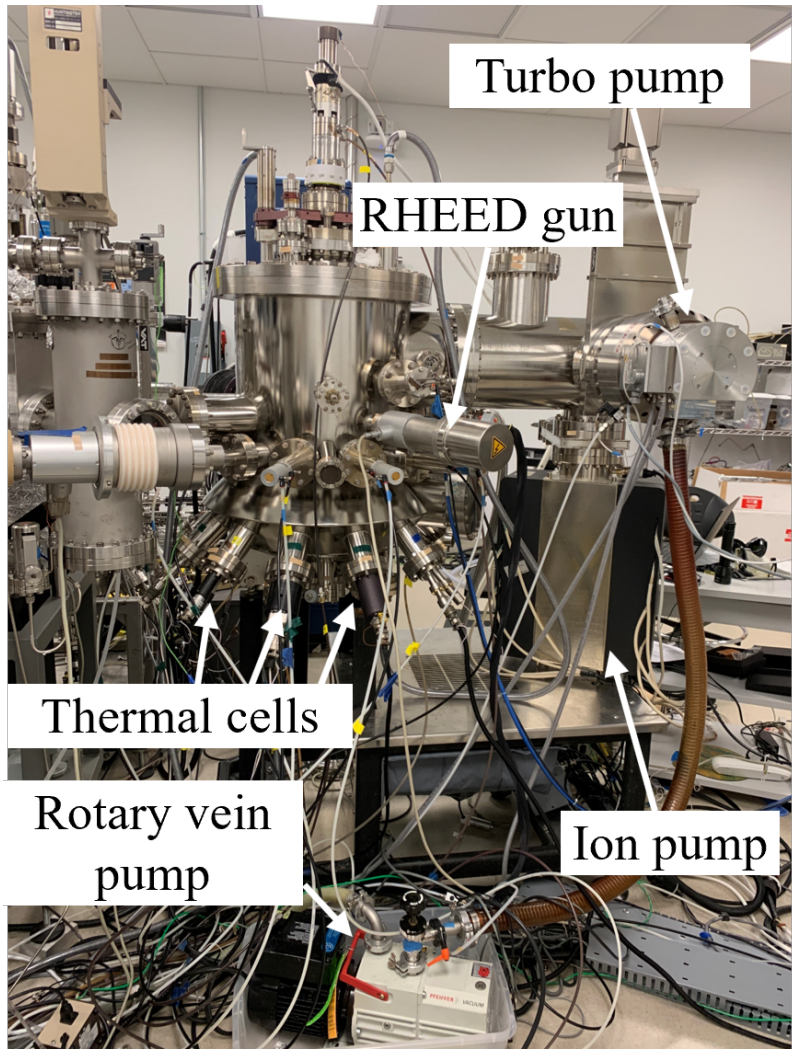

Figure 2.3: Picture of MBE system growth chamber in Lederman Lab at UCSC.

Substrate crystal preparation is critical for the growth of a high quality thin

film. Substrates are often cut from large single crystals with very few defects and polished such that the surface is atomically smooth. There are several commercial companies that specialize in producing substrate crystals for thin film growth, such as the MgF_2 and Al_2O_3 substrates used in this work, which were purchased from MTI Corporation. Before the substrates are loaded into the growth chamber, they are sonicated for several minutes in an acetone bath and then an isopropyl alcohol bath to remove debris or organic contaminants on the surface. The substrate is then mounted on a sample plate that will be loaded into the growth chamber. The substrate is adhered to the sample plate with silver paint to create good thermal conduction between the substrate and the sample plate, an important step because the substrate heater applies heat from the backside of the sample plate and not directly to the substrate itself. The substrate is also held in place with clips to keep it secured as it is mounted upside down in the growth chamber. An image of a sample plate and substrate after growth of a thin film is shown in Fig. 2.4.

The transition metal fluoride and TI thin films studied in this work were grown in a custom build MBE system in the Lederman Lab at the University of California Santa Cruz (UCSC), with a separate UHV chamber for the fluorides and for the TIs, connected by a UHV transfer chamber to enable movement of samples between the growth chambers without breaking vacuum, which was important for growth of the AF insulator-TI bilayers studied in this work. The fluoride growth chamber had a base pressure of nearly 1×10^{-9} Torr while the TI growth chamber had a lower base pressure of 1×10^{-10} Torr.

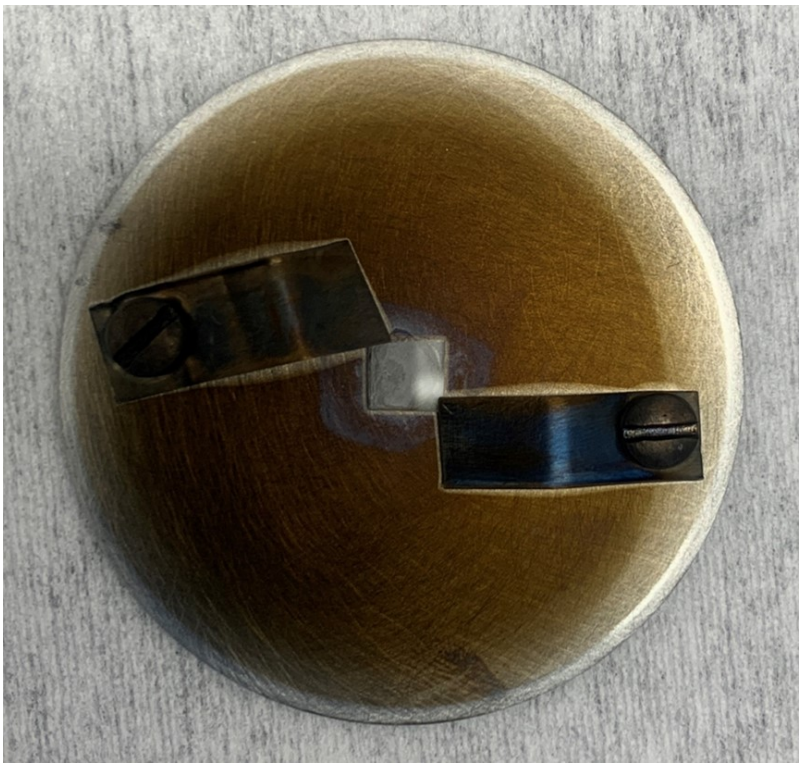

Figure 2.4: An MBE sample plate with sample after growth of a MnF_2-BST thin film.

2.2 Thin film crystallography

2.2.1 Reflection high energy electron diffraction

The MBE system used in this work included apparatus to perform in-situ reflection high energy electron diffraction (RHEED) measurements of the thin film before, during, and after growth. Performing RHEED measurements involves firing a beam of high energy (approximately 10-20 keV) electrons at grazing angle incidence on the sample. At this shallow angle of incidence, the electrons do not penetrate more than a few atomic layers into the film and therefore are mostly sensitive to the surface crystallinity alone. The surface of a crystal is periodic only in two dimensions and can be described in terms of a 2D lattice, with the 3D unit cell replaced by a 2D unit mesh that combine to form a 2D net describing the lattice structure. A useful construction of the diffraction conditions for the 2D net is the Ewald sphere with its radius defined as the momentum vector of the scattered electrons. In this construction, the 2D reciprocal net points are extended out of the 2D plane to form reciprocal lattice rods, and constructive interference occurs wherever the Ewald sphere intersects one of these rods. As the electrons diffract off of the crystal surface, they are directed at a fluorescent screen that glows when it absorbs electrons, allowing the electron diffraction pattern to be observed optically [43].

In a very high quality crystal, with an atomically smooth surface and single phase orientation without crystal domains, the RHEED pattern will take the form of bright spots oriented along an arc, and potentially include Kikuchi lines that arise from two-scatterer processes [43, 44]. If the crystal surface is atomically smooth but has several crystal domains of the same crystal structure, then the reciprocal space rods are broadened and the RHEED spots become bright streaks instead. If the crystal surface is sufficiently rough, consisting

of islands of material that break the 2D description of the surface, then the electron beam will actually transmit through the islands and the RHEED pattern will show many transmission spots. Of course if the crystal is actually not crystalline at all, then there is no diffraction condition to be found and RHEED will show no constructive interference at all. Figure 2.5(a) shows the RHEED pattern of a MgF_2 subsrate that exhibits the Kikuchi lines pattern, while Fig. 2.5(b) shows the RHEED pattern of a NiF_2 thin film exhibiting the bright, sharp diffraction streaks associated with a very smooth and crystalline film with some single phase domains.

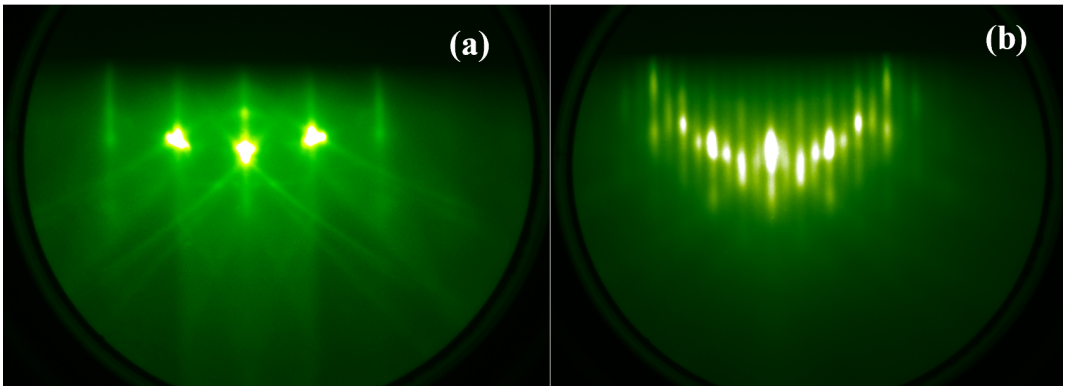

Figure 2.5: (a) RHEED pattern of MgF_2 substrate with Kikuchi lines visible. (b) RHEED pattern of a very smooth and crystalline NiF_2 thin film.

In addition to probing the crystal structure of the surface of material, RHEED in conjunction with MBE can be used to observe the layer by layer growth of a crystal layer. In MBE, the growth rate of a thin film crystal can be low enough that the crystal is grown in a single layer at a time, with the adsorbed atoms not constructing the next layer until the one below is completed. Because RHEED is sensitive to the surface crystal structure, this layer by layer growth can be detected through oscillations in the RHEED intensity. Consider RHEED of a crystal substrate before deposition of a new layer. The RHEED intensity is at a maximum here because the crystal has the maximum number

of coherent crystal planes from which the electrons will constructively interfere. As deposition of a new layer begins, the new surface becomes disordered as the adsorbed atoms are mobile, still settling into their stable low energy configuration, and the RHEED intensity drops because there are fewer coherent crystal planes to diffract off of. The RHEED intensity will drop for some time as the new layer is deposited, until it begins to increase again as more and more of the layer is formed, eventually reaching a local maximum when the layer is fully formed, before dropping again as sequential layer is deposited on the newly formed layer [45]. Experimental observation of these intensity oscillations is shown in Fig. 2.6 for a Bi_2Te_3 thin film. In this way, RHEED intensity oscillations can be used to observe the growth of individual layers of the crystal.

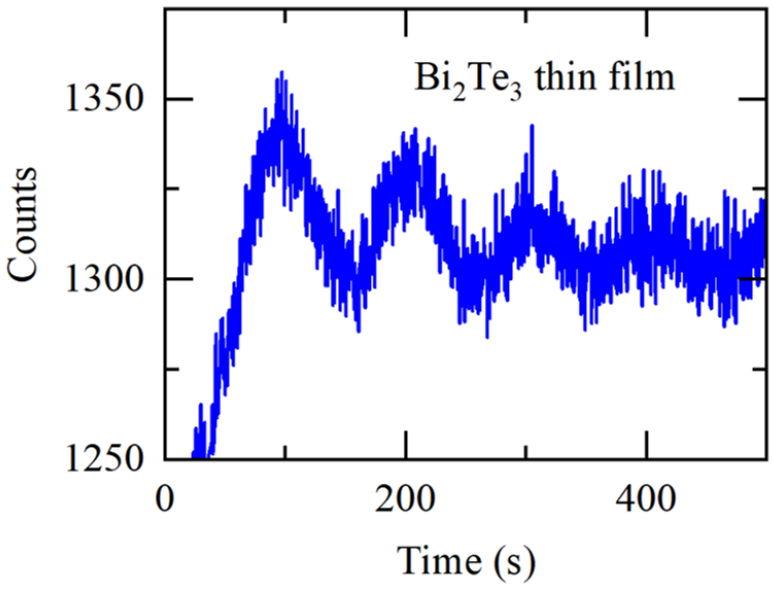

Figure 2.6: RHEED oscillations of Bi_2Te_3 thin film

When properly utilized RHEED measurements can provide very useful information for thin film crystal growth. RHEED of the crystal substrate before growth is often used to check the smoothness and crystallinity of the substrate, as a high quality substrate is an important part of a high quality thin film.

RHEED is also used during the growth of the film itself, to both observe the surface quality of the thin film and to record RHEED intensity oscillations and quantify the layer by layer growth. After the growth is completed in-situ RHEED is an important tool as it permits characterization of the film surface before vacuum is broken and the sample is potentially exposed to air or other harmful conditions. The MBE system in the Lederman lab utilized in-situ RHEED to study the thin films before, during, and after growth, at electron energies between 15 and 18 keV.

2.2.2 X-ray diffraction

X-rays are an invaluable tool to crystallographers due to their wavelength when compared with the distances involved in crystal lattices. Distances between atomic planes in a crystal are often on the scale of a few angstroms, which means the several thousand angstrom wavelength of visible light will never be sensitive to diffraction between atomic planes. X-rays however can have wavelengths on the order of a single angstrom, as is the case with commonly used Cu K_α and Mo K_α x-rays, which wave wavelengths of 1.54 Å and 0.71 Å respectively. At these small wavelengths, x-rays can diffract between the individual atomic planes of a crystal and interfere constructively in a way that is utilized by x-ray diffraction (XRD) measurements.

From a geometrical perspective, the mathematics describing XRD is relatively straightforward. As x-rays penetrate a crystal, a small number of them are reflected at each crystal plane and come back out of the crystal. At certain incident angles, the phase difference between each successive plane reflection will equal 2π and the reflected x-rays will interfere constructively, creating a peak in the reflected x-ray intensity. The constructive interference condition depends on the wavelength of the incoming x-rays (λ), the angle of incidence

with the crystal planes (θ), and the spacing between the crystal planes (d), and is expressed by the Bragg equation,

$$n\lambda = 2d\sin(\theta). \tag{2.4}$$

Each crystal has a unique XRD pattern, acting essentially like a fingerprint that can be used to precisely identify the crystal. From the XRD pattern of peaks as a function of θ the lattice structure can be determined, because different structures will have certain symmetries or reflections that are forbidden. For instance the body-centered cubic lattice structure forbids the (100), (300), (111) and (221) diffraction peaks, among others. The face-centered cubic lattice forbids peaks whose hkl are mixed even and odd, and the hexagonal close packed lattice will have 6-fold symmetry in contrast to the 4-fold symmetry of the cubic lattices when rotated about the primary crystallographic axes. From the angular distance between diffraction peaks the lattice spacing d can be determined, and the orientation of the crystal faces can be determined by performing XRD about different normal directions to the sample.

When working with diffraction effects, it is often useful to describe the periodic lattice and the scattering vectors in reciprocal space instead of real space. Consider the function $n(x)$ that describes a 1D lattice with period a. The real space periodic function $n(x)$ can be expanded in a Fourier series [46]

$$n(x) = \sum_p n_p e^{i2\pi px/a}, \tag{2.5}$$

where p is an integer, and $2\pi p/a$ is a point on the reciprocal space lattice. In 3D, the reciprocal lattice spacing $2\pi p/a$ is replaced by the reciprocal lattice

vector $\mathbf{G}$

$$n(\mathbf{r}) = \sum_{\mathbf{G}} n_{\mathbf{G}} e^{i\mathbf{G}\cdot\mathbf{r}}. \tag{2.6}$$

As it turns out, the scattering condition for constructive interference from diffraction is satisfied when the phase difference between the incident and diffracted wavevectors is equal to a reciprocal lattice vector $\Delta\mathbf{k} = \mathbf{G}$. This feature of reciprocal space is useful in describing the Bragg condition, as the phase difference can be described in terms of the scattering vector $\mathbf{Q}$, where

$$\mathbf{Q} = \Delta\mathbf{k} = \frac{4\pi}{\lambda}\sin\theta. \tag{2.7}$$

It is often easier to work in reciprocal space than in real space when dealing with diffraction. In XRD measurements for example, when plotting the diffraction pattern as a function of 2θ, the distance between successive diffraction peaks is non linear and goes as $2\theta = 2\sin^{-1}(\frac{n\lambda}{2d})$. In contrast, when plotting the diffraction pattern as a function of the scattering vector Q, each distance between each successive diffraction peaks is linear and goes as $Q = \frac{2\pi n}{d}$. This has the benefit of making peaks belonging to the same crystal structure easily identifiable, as they will be separated by the same value of Q, as shown in Fig. 2.7(b), where the separation between successive diffraction peaks of the MgF_2 {110} substrate (where the curly bracket notation refers to the family of {110} peaks) in Q can be calculated according to $Q = \frac{2\pi}{3.268\ \text{Å}} = 1.922\ \text{Å}^{-1}$.

The XRD measurements presented in this work were primarily performed using Cu K_α x-rays in a Rigaku Smartlab thin film x-ray diffractometer located in the Chemistry Department at UCSC, although some later measurements were performed in a newer Rigaku Smartlab thin film x-ray diffractometer in the Lederman Lab. Peak fitting of the XRD data was performed with OriginPro software from OriginLab, using built in peak fitting functions.

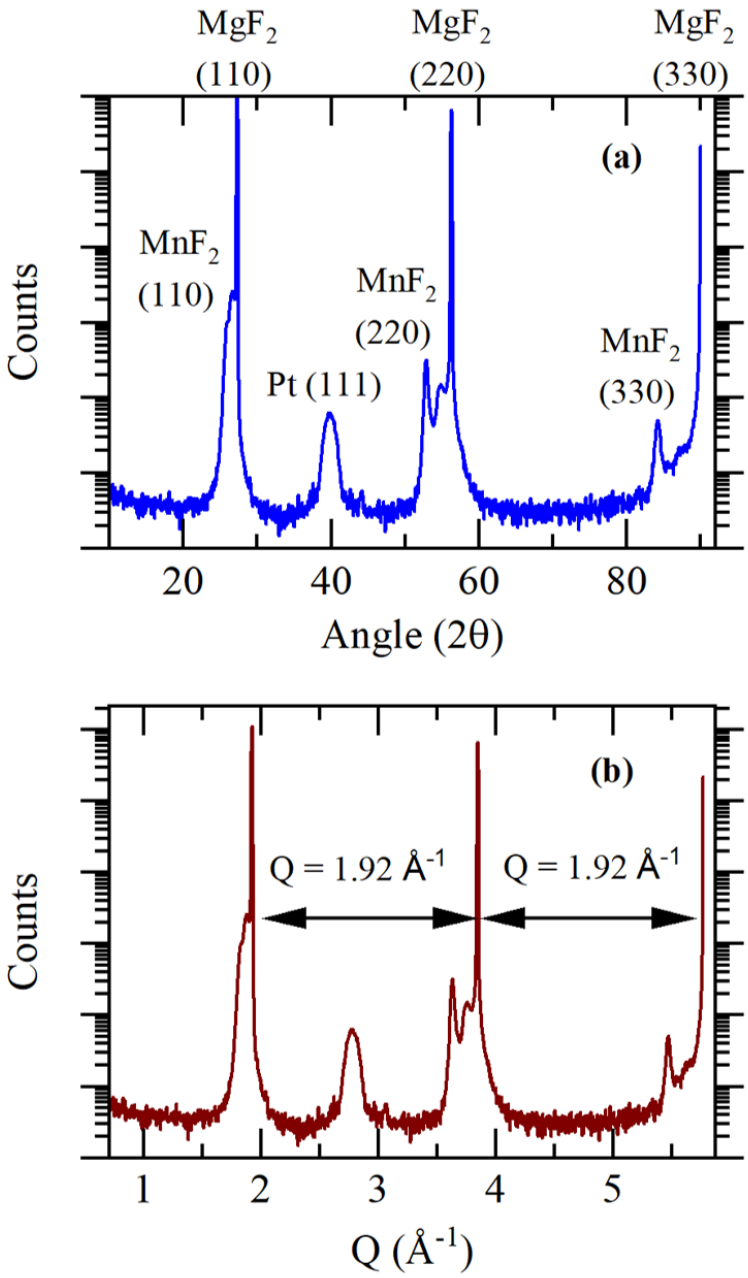

Figure 2.7: (a) Example XRD pattern of MnF_2 - Pt bilayer grown on a MgF_2 (110) substrate plotted as a function of the incident angle 2θ, with peaks identified. (b) The same XRD pattern as in (a) but plotted as a function of the scattering vector Q. The constant spacing between successive MgF_2 110 peaks is shown in the plot.

2.2.3 X-ray reflectivity

In sufficiently thin films, there can arise interference patterns from reflections off of the top and bottom surfaces of the film. This can be observed optically in thin oil slicks on the surface of water, as under the right conditions, an iridescent pattern will develop due to interference patterns among the different wavelengths of visible light. A similar effect can occur in x-rays directed at sufficiently thin film at shallow angles. Constructive and destructive interference oscillations, known as Kiessig fringes, will develop in the reflected x-rays, and the technique used to generate and study these reflections is known as x-ray reflectivity (XRR). In contrast to XRD which is sensitive to the lattice planes of the crystal, XRR is sensitive to the interfaces between materials with different electron densities. The number, intensity, and pattern of the intensity oscillations depends on the thickness of the thin film, the number of interfaces, the roughness of those interfaces, and the electron density of the layers.

Measurements of XRR are very similar to XRD measurements and therefore x-ray diffractometers can often also perform XRR. The XRR patterns in this work were measured on the same Rigaku Smartlab thin film x-ray diffractometers that were used for XRD. The analysis of the XRR data was performed using non-linear least squares fits with an optical model in the GenX software package [47].

2.3 Magnetometry

In order to measure the magnetic moment of any material, it is necessary to both control the temperature of the material, so that measurements can be made above and below the transition temperature, and to record the magnetization of the material itself. This is accomplished using an instrument known

as a magnetometer.

The thin film magnetization measurements presented in this work were performed using a Quantum Design MPMS XL superconducting quantum interference device (SQUID) magnetometer. This instrument enables precise control of the applied magnetic field to the sample and of the temperature of the sample while measuring the magnetic moment of the sample. It is capable of applying external magnetic fields as high as 7 Tesla by employing a superconducting solenoid immersed in a liquid helium dewar. The liquid helium bath is used to both keep the superconducting solenoid below its critical temperature and to cool the sample space to temperatures as low as 2 K while keeping the sample in an inert helium gas atmosphere. Heaters are used to warm the helium exchange gas and the sample space itself. The SQUID magnetometer used in this work has only the longitudinal sensing option installed, which means the magnetic moment is always measured along the same direction as the applied magnetic field and not perpendicular to it.

When measuring the magnetic moment of a thin film, the magnetometer must be very sensitive to very small moments, as the films can be as thin as just a few nanometers and only a few square millimeters in surface area. The SQUID magnetometer accomplishes this by utilizing a Josephson junction, which is constructed of a superconductor loop joined by a thin layer of an insulator, where the insulating layer is thin enough that electric current can flow through it by tunneling through the barrier. It can be shown that the tunneling current through the insulator is dependent on the phase difference between the superconducting wavefunctions on either end of the insulator junction. When the superconducting loop is placed in a magnetic field, an inductive electromagnetic force is generated that changes the phase difference between the superconducting wavefunctions at the Josephson junction and changes the

Figure 2.8: Picture of the Quantum Design MPMS XL SQUID Magnetometer in the Lederman Lab at UCSC.

tunneling current in a way that is measurable. By first calibrating the SQUID in a known magnetic field, a magnetic sample can then be place in the center of the superconducting loop and any changes in the tunneling current can be attributed to the sample.

Measurements of the magnetic moment as a function of the sample temperature or the applied magnetic field are commonly used to characterize the magnetic proprieties of a sample. Temperature dependent measurements are useful for determining the critical temperature of the magnetic phases in a material and are often performed in three different variations; zero-field cooled (ZFC), field cooled (FC), and thermal remnant magnetization (TRM). A single measure-

ment sequence can't measure all three variations in a single experiment. First a sample is loaded into the magnetometer and cooled to the lowest desired temperature without the application of any external magnetic field, this is known as zero-field cooling. Once the sample has reached the desired temperature, an external magnetic field is applied (in order to provide a preferred spin orientation and help align the local magnetic moments together) and the moment of the sample is measured as it is warmed to the highest desired temperature. This is the ZFC measurement of the magnetic moment and can show distinct features from the other measurements because some disorder can be locked in by cooling through the critical temperature without application of an external field. Once the ZFC measurement is completed, the field remains on and the moment of the sample is measured as it is cooled back down to the lowest desired temperature in the FC variant of the measurement. Finally, once the sample is back at its lowest temperature, the external field is turned off and the moment of the sample is measured as it is warmed back up to the highest desired temperature. In this TRM variant, the spontaneous magnetic moment that persists even in zero applied field is observable, without contributions from paramagnetic moments. A temperature dependent measurement of a NiF_2 thin film is shown in Fig. 2.9, where the ZFC and FC measurements had an applied field of $\mu_0 H = 1$ kOe in plane perpendicular to the c-axis, and the magnetic phase transition at the critical temperature is seen at approximately $T = 80$ K. The ferromagnetic signal in the NiF_2 film is due to canted AF moments. Each of these variations of the temperature dependent magnetic moment yield different information about the magnetic properties of the sample.

If the goal is to measure magnetic hysteresis (the field at which a ferromagnetic moment goes through zero) or the saturation moment (the moment when all

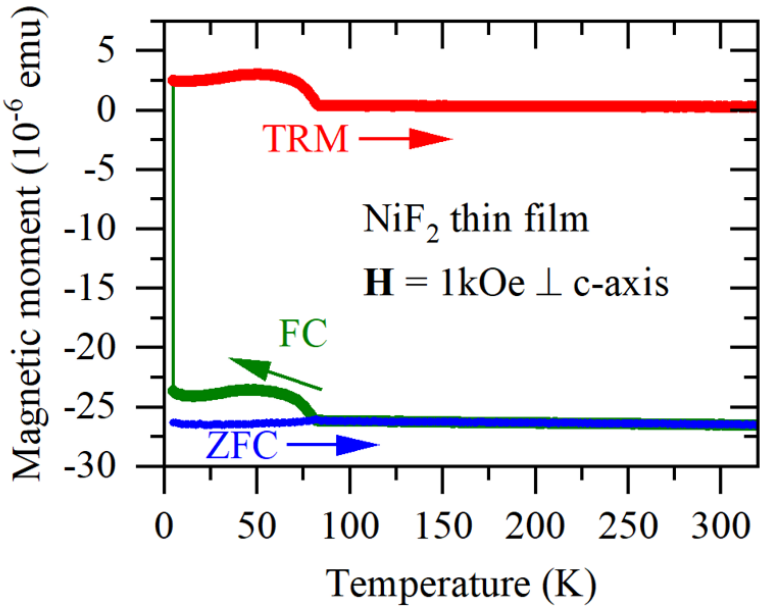

Figure 2.9: ZFC-FC-TRM measurement of NiF_2 thin film. The ZFC and FC measurements had an applied field of $\mu_0 H = 1$ kOe in plane perpendicular to the c-axis.

the magnetic domains are aligned in the same orientation), then measurements are performed as a function of the applied magnetic field. In these measurements the sample temperature is fixed as the applied magnetic field is swept and the resulting measurement reveals how the magnetic domains flip from one orientation to the antiparallel orientation, as shown in Fig. 2.10. The field dependent measurement can also be performed in ZFC and FC variants.

Several different mathematical models are used to fit to measurements of magnetization. The software used to perform these fits is OriginPro from OriginLab. Simple linear fits are used to calculate parameters such as saturation moment and hysteresis, but more specific, custom models are written into the built-in fitting function builder, such as the model for rounded transition

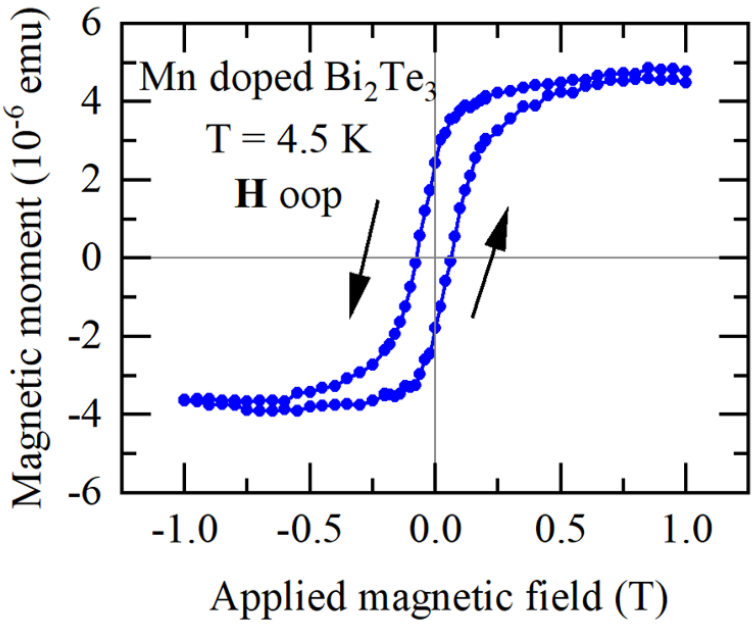

Figure 2.10: M vs H of Mn doped Bi_2Te_3 at $T = 4.5$ K with the field applied out-of-plane. The black arrows indicate the direction of field sweeping.

temperatures

$$m(T) = \frac{C}{\sigma_c\sqrt{2\pi}} \int_T^\infty (1 - T/T_c')^\beta e^{-(T_c - T_c')^2/2\sigma_c^2} dT_c', \tag{2.8}$$

where C is a scaling parameter, σ_c is the rounded width of the transition, T_c is the average critical temperature of the sample, β is the critical exponent, and T_c' is a dummy variable in the integral for the transition temperature distribution [48]. Fit parameters and their errors are produced by the software upon fitting the model.

2.4 Device fabrication

In order to measure the electronic transport properties of the TI films and bilayers, the samples were fabricated into a Hall bar device configuration. The basic Hall bar design utilizes sets of measurement arms aligned parallel to

the flow of current (to measure longitudinal conductance) and perpendicular to the flow of current (to measure Hall conductance). The Hall bar design used in this work is a bi-directional construction, that is essentially two Hall bars oriented 90° to each other and joined at a common current source pad. This perpendicular construction enables electronic measurement along two orthogonal crystallographic directions of the film on the same device, which will become relevant when studying bilayers on magnetic crystals with specific easy axes.

2.4.1 Photolithography

To create the bi-directional Hall bar device pattern on the TI thin films, photolithography processes were used. Lithography in general is a printing process where selected areas are covered with a greasy substance that prevents ink from adhering to those areas. Photolithography is similar, but instead of using grease and ink to create a pattern, special light-sensitive polymers called photoresists and ultraviolet (UV) light is used to create a pattern of the photoresist material. The process begins by coating the sample film in the liquid photoresist material by means of a spin coater device, which spins the sample at high speed to create a thin, uniform film of the photoresist. The sample is then heated to evaporate the solvent in the photoresist and harden the material. The next step is the exposure step, where the photoresist is exposed to ultraviolet light that will change the chemical bonds in the photoresist polymers. In a positive resist, the areas exposed to UV light become soluble in certain chemical solutions known as developers and the unexposed areas become inert. In negative resists the opposite is true, the areas exposed to UV light become inert and unreactive with the developer and the unexposed areas will remain soluble. The photomask is the tool that holds the pattern that

will be printed into the photoresist. It is often made of UV transparent quartz or soda-lime glass with the device pattern bonded to the glass in an opaque metal such as chromium. The mask aligner is used to orient the mask and the sample together and to hold them in place while a UV lamp exposes the sample to a certain amount of energy specific to the photoresist being used. In the case of a positive Hall bar, the Hall bar pattern is left unexposed by the mask while the rest of the sample is exposed to the UV lamp. The exposed sample is then placed in a solution of developer which removes the unwanted areas of photoresist and leaves behind only the desired pattern.

The Hall bar devices used in this work were created using the KL IR LO photoresist from KemLab that can be used as either a positive or negative photoresist. The initial Hall bar pattern is created by following the manufacturer supplied parameters for exposure energy, bake time and bake temperature, which vary with the type of photoresist being used. A positive resist pattern is exposed using a Karl Suss mask aligner with a 365 nm exposure bulb. The film is then baked and developed using a solution of TMAH-0.26N. In Hall bar devices that had dielectric top gates deposited on them, the top gate pattern was created using the KL IR LO photoresist in the reverse photoresist mode, which involves an additional bake step and a flood exposure where the entire film is exposed to UV light. The Karl Suss mask aligner used for this process is shown in Fig. 2.11. The yellow tinting is due to filtered light to prevent blue light from reacting with the photoresists.

2.4.2 Wet etching

In the case of the Hall bars used in this study, the objective of the photolithography process is to create a layer that will protect the film underneath the photoresist while the unwanted film is removed. The process of removing un-

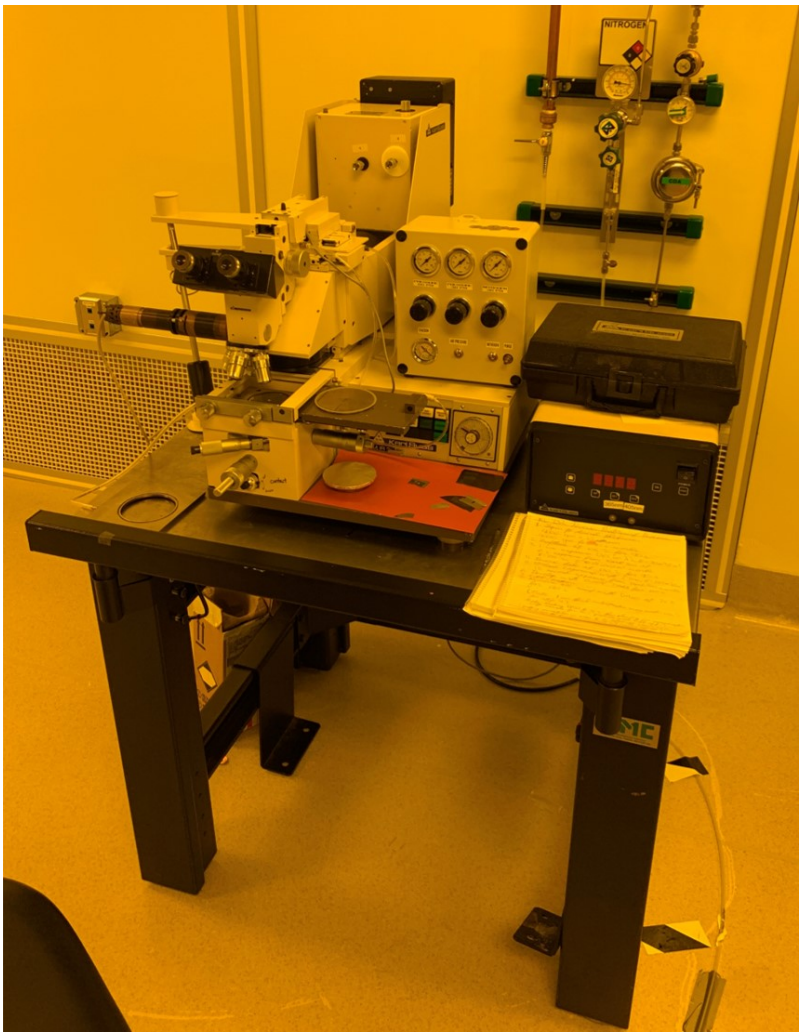

Figure 2.11: Picture of the Karl Suss mask aligner in the nanofabrication cleanroom in the Lederman Lab at UCSC.

wanted film is known as etching, and there are several ways to etch. There are dry etching processes that use plasmas or ion bombardment to remove material, and there are wet etching processes that use acids and bases. In both of these etching methods, the photoresist is mostly resistant to the etch and will protect the material beneath it, enabling selective removal of material. For the TI films used in this study, a wet etch process was used that utilized a mixed acid solution of nitric and hydrochloric acid that is famous for its ability to dissolve noble metals, lending it the colorful name of aqua regia. The wet etch

process itself is fairly straightforward, acid resistant plastic tweezers are used to hold the sample while it is immersed in the aqua regia solution consisting of 1 part nitric acid, 3 parts hydrochloric acid, and 4 parts water, for approximately 5 seconds. Once the film has been removed, the sample is removed from the aqua regia and dipped in de-ionized water to end the etching process. The remaining photoresist can then be removed in the solvent DMSO and all that is left is the film layer in the desired pattern.

2.4.3 lift-off

In some cases, instead of using etching processes to remove material from a film, it is desirable to use the photoresist itself to remove the unwanted material. This process involves first developing a negative photoresist pattern onto the sample and then depositing the thin film. Then when the photoresist is removed, any material deposited on the resist will also be removed in a process known as lift-off. This technique is especially useful for depositing conducting pads or insulating gates on top of preexisting devices, but is only effective when the photoresist layer is much thicker than the layer being lifted off. The thickness of the photoresist layer is determined by the rotational speed of the spin coater and the type of resist used. In the case of the KL IR LO resist used in this work, the films were approximately 1.2μm thick, more than enough to lift off 100 nm of dielectric material.

2.5 Electronic transport measurements

The electronic transport properties of the TI Hall bar devices were measured in a JANIS SuperVariTemp X-Gas Superconducting Magnet System located in the Lederman Lab, shown in Fig. 2.13. This cryostat instrument utilizes a liquid helium dewar to both cool a superconducting solenoid capable of ap-

plying steady-state magnetic fields of 12 Tesla, and to cool the sample to temperatures below 2 K. The cryostat sample arm contains wiring that runs the length of the arm and electrically connects the sample to a break-out box with coaxial and triaxial BNC connectors that can be connected to voltage and current sources and multimeters. DC current was supplied to the sample Hall bars and the longitudinal and Hall voltages were measured using DC Keithley sources and digital multimeters. The current source was used in a delta mode measurement method to take voltage measurements of first the longitudinal component followed by the transverse component, with alternating pulses of DC current ranging from 2 to 10 μA, depending on the resistance of the film. The geometry of the delta mode measurement on the Hall bar is shown in Fig. 2.12.

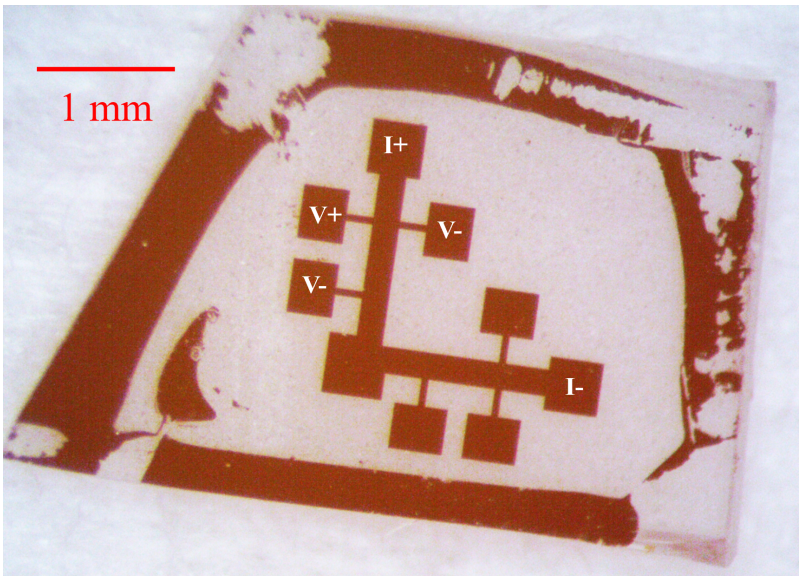

Figure 2.12: Diagram of transport measurement geometry of delta mode measurement on Hall bar devices.

From measurement of the longitudinal and Hall voltages, the corresponding values of resistance can be calculated from Ohm's law $V = IR$ because the current is held constant. Much like the measurements of magnetic moment, it

is useful to measure these voltages as a function of the sample temperature and of the external magnetic field. From measurements of the Hall resistance R_{xy} as a function of the applied magnetic field, the carrier density n of a conducting channel with cross sectional area A and length l is calculated according to

$$R_{xy}\frac{A}{l} = \rho_{xy} = \frac{\mu_0 H}{ne}. \tag{2.9}$$

From the carrier density of the channel, the Hall mobility μ is derived according to

$$R_{xx}\frac{A}{l} = \rho_{xx} = \frac{1}{ne\mu}. \tag{2.10}$$

Several different mathematical models are used to fit to measurements of electrical conductance. The software used to perform these fits is OriginPro from OriginLab. Simple linear and logarithmic fits are executed using fitting models included in the software, while more specific, custom models are written into the built-in fitting function builder and are described in Section 1.2. Fit parameters and their errors are produced by the software upon fitting the model.

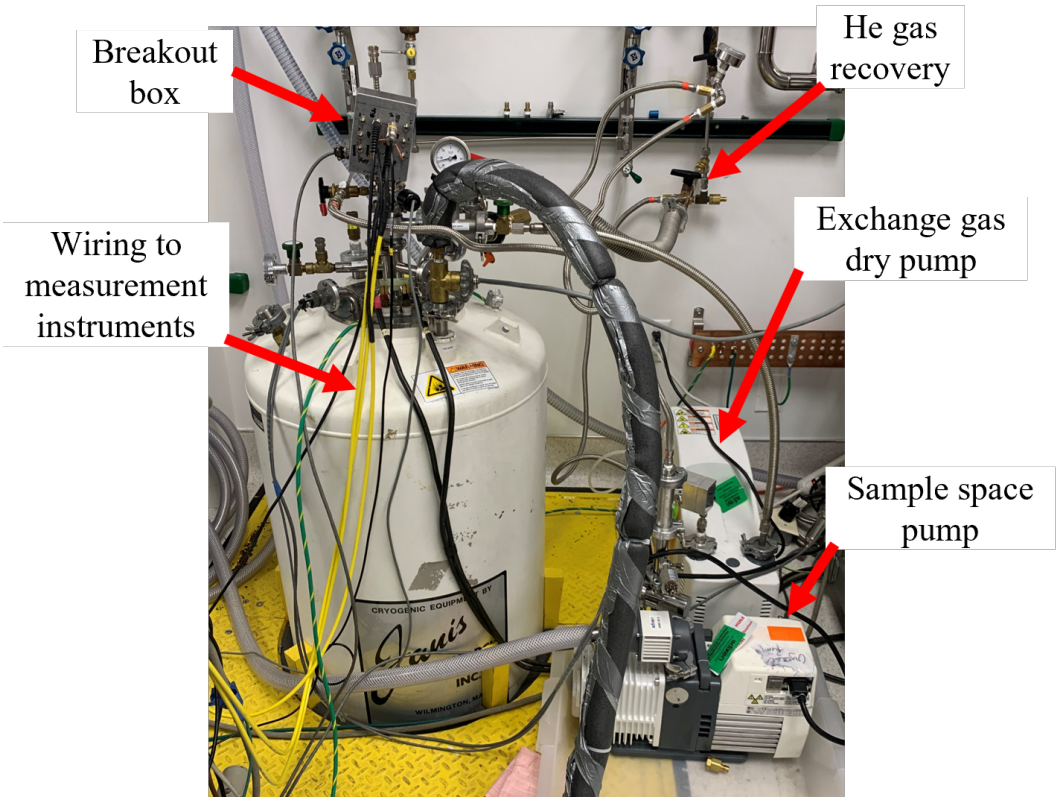

Figure 2.13: Picture of JANIS cryostat in the Lederman Lab at UCSC. The sample is attached to the end of the cryostat arm which is placed into the center of the system. The breakout box allows the sample on the cryostat arm to be connected to external Keithley source meters and multimeters to perform electrical measurements.

Chapter 3

Magnetic properties of MnF_2, NiF_2, and $Mn_xNi_{1-x}F_2$ thin film alloys

3.1 Introduction

NiF_2 and MnF_2 are model antiferromagnets (AFs) which share a rutile, tetragonal $P4_2/mnm$ space group crystal structure with similar lattice parameters [49], but which have different magnetic structures. NiF_2 is a (110) easy plane antiferromagnet with an effective Dzyaloshinskii–Moriya interaction (DMI) that causes the antiferromagnetically aligned moments to spontaneously cant in the easy plane, generating a weak ferromagnetic moment perpendicular to the Néel vector [8, 10, 11]. The DMI is an important ingredient for the development of stable helical spin textures, such as skyrmions and hopfions, which have promising applications in spintronic technologies [5, 50–53]. MnF_2 lacks a DMI, and its [001] easy axis is due primarily to dipole-dipole interactions resulting from the crystal structure of the material, making it a useful system

in which to study magnons in Ising-like systems [13, 54, 55]. MnF_2 also has a relatively small and accessible spin-flop field ($\sim$ 9.3 T), making it easier to perform steady-state measurements above the spin-flop transition [56, 57].

The $Mn_xNi_{1-x}F_2$ alloy system is interesting because of the competing single-ion magnetic anisotropies of the Ni^{2+} and Mn^{2+} ions, which are perpendicular and parallel to the [001] crystallographic direction, respectively, as shown in Fig. 1.4. The resulting random magnetic anisotropy can lead to new magnetic phases near the critical temperature of the material, where the single-ion anisotropy term dominates the spin Hamiltonian. One such material that possesses these characteristics, $Fe_xNi_{1-x}F_2$, has been studied previously and exhibited a unique magnetic phase diagram with evidence of a magnetic glassy phase due to random magnetic anisotropy [48]. MnF_2 is similar to FeF_2 in that it has the same rutile crystal structure and is an easy axis AF that orders along the *c*-axis, but it has a spin of 5/2 instead of 2 and importantly, it has a single-ion anisotropy energy that is nearly 10 times smaller than that of FeF_2 [49, 54, 58]. This makes the $Mn_xNi_{1-x}F_2$ alloy an interesting point of comparison with previous work on $Fe_xNi_{1-x}F_2$ as it demonstrates how differences in the single-ion anisotropy energy affect the magnetic properties of the system. Understanding how this parameter affects the system is essential to accurately predicting ordering behavior near the transition temperature because the single-ion anisotropy energy will dominate the spin Hamiltonian near this critical point [48].

This chapter presents a crystallographic and magnetic study of thin films of MnF_2, NiF_2, and $Mn_xNi_{1-x}F_2$ alloys. This study demonstrates that the $Mn_xNi_{1-x}F_2$ thin film alloys are mixed homogeneously and do not separate into their constituent NiF_2 and MnF_2 parts. XRD and magnetization measurements show that epitaxial MnF_2 thin films grown on MgF_2 are highly

strained, which has the effect of lowering the AF transition temperature due to piezomagnetism [59–61]. This epitaxial strain induced piezomagnetism is verified in a relaxed MnF_2 thin film grown using a $(MnNi)F_2$ graded buffer layer, demonstrating that when epitaxial strain is eliminated, the transition temperature of the relaxed MnF_2 thin film matches the expected bulk value. Magnetization measurements of $Mn_xNi_{1-x}F_2$ thin film alloys show that the system has a rich magnetic phase diagram, including an emergent ordered unidentified phase in a narrow temperature range near the transition temperature. Mean-field theory (MFT) equations using the true random magnetic anisotropy are presented and are compared with the experimentally derived phase diagram and exchange energies of the thin film alloys.

3.2 Methods

The $Mn_xNi_{1-x}F_2$ alloy thin films in this study were all grown in an ultra-high vacuum molecular beam epitaxy (MBE) system (base pressure $< 10^{-8}$ Torr) by sublimation of commercially purchased NiF_2 and MnF_2 powders ($> 99\%$ purity) onto commercially purchased MgF_2 (110) substrates. Before starting the growth process, the substrate was annealed at $T = 300°C$ in the growth chamber for a minimum of 1 hour. Reflection high-energy electron diffraction (RHEED) patterns were acquired after annealing the substrate to ensure satisfactory surface smoothness and crystallinity before deposition. A retractable crystal monitor inside the growth chamber was used to calibrate the molecular flux of the NiF_2 and MnF_2 beams and to set the desired stoichiometry of each sample. All $Mn_xNi_{1-x}F_2$ thin films, including the $x = 0$ (pure NiF_2) and the $x = 1.0$ (pure MnF_2) films, were grown to a thickness of 30 nm after growing an epitaxial 1 nm thick NiF_2 buffer layer between the substrate and the alloy film, in order to reduce lattice mismatch and create a higher-quality film [48].

MnF_2 films with reduced strain were grown using a 20 nm thick $(MnNi)F_2$ graded buffer layer, where $Mn_xNi_{1-x}F_2$ was first deposited with $x = 0$ (pure NiF_2) and then the MnF_2 flux was slowly increased while the NiF_2 flux was gradually decreased simultaneously until the top of the film was $x = 1$ (pure MnF_2), at which point a 30 nm MnF_2 film was grown. RHEED patterns of all films were then acquired before removing the films from the vacuum system.

X-ray diffraction (XRD) measurements of the thin films were performed using Cu K_α radiation from a Rigaku SmartLab thin film x-ray diffractometer. The value of the (110) lattice parameter out of the plane of the sample was calculated from the XRD peak positions of the peaks according to Bragg's law, $2d_{hkl}\sin(\theta_{hkl}) = \lambda$, where d_{hkl} is the lattice constant corresponding to planes defined by the Miller indices (hkl), θ_{hkl} is the measured Bragg diffraction angle corresponding to the (hkl) plane, and $\lambda = 0.15406$ nm is the x-ray wavelength used.

Magnetic properties of the films were studied using a Quantum Design MPMS XL superconducting quantum interference device (SQUID) magnetometer by measuring magnetic moment as a function of temperature. The transition temperature of each sample was determined by fitting magnetic moment as a function of temperature near the critical point to a distribution of sharp transition temperatures due to disorder or other factors given by Eq. 2.8.

3.3 Results and discussion

3.3.1 Thin film crystallography

Before the samples were removed from the growth chamber, RHEED patterns of the films were collected to check the crystal quality of the surface, as shown in Fig 3.1. The bright and sharp streaks in the diffraction pattern of the pure

NiF_2 sample in Fig 3.1(a) indicate a smooth and highly oriented surface. There are even faint Kikuchi lines that are only present in very smooth, single phase crystal surfaces. The NiF_2 films grow well on MgF_2 substrates due to the good lattice match between the thin film and the substrate, as shown in the lattice parameters in Table 3.1. In the $Mn_xNi_{1-x}F_2$ films, the RHEED pattern remains sharp and streaky in films with low MnF_2 doping, indicated by the value of x, but the RHEED pattern becomes spotty as x increases, indicating that the surface is becoming rougher. The decreasing surface quality with increasing MnF_2 concentration is likely due to the significant lattice mismatch between MnF_2 and the MgF_2 substrate, as shown in Table 3.1. This is evidenced by comparing the RHEED pattern in Fig 3.1(e), which was grown directly on a MgF_2 substrate, to that in Fig 3.1(f), which was grown on a $(MnNi)F_2$ graded buffer layer. By using the $(MnNi)F_2$ graded buffer layer to gradually increase the lattice parameters from NiF_2 values to MnF_2 values, the lattice mismatch is reduced and strain in the MnF_2 film is eliminated. The result is a MnF_2 film with improved surface smoothness, as indicated by the improved RHEED pattern shown in Fig 3.1(f).

XRD rocking curve measurements of the MnF_2 thin films also show evidence that the $(MnNi)F_2$ graded buffer layer improves the structural quality of the MnF_2 film. The diffraction peak broadening in a rocking curve measurement is related to the crystallite size by the Scherrer equation [62]

$$\tau = \frac{K\lambda}{\beta \cos\theta}, \tag{3.1}$$

where τ is the crystallite size, K is a dimensionless crystal shape constant, λ is the x-ray wavelength, β is the full width half maximum (FWHM) of the peak, and θ is the Bragg angle. The Scherrer equation is only applicable to crystallites below a few hundred nanometers across, as is likely the case in

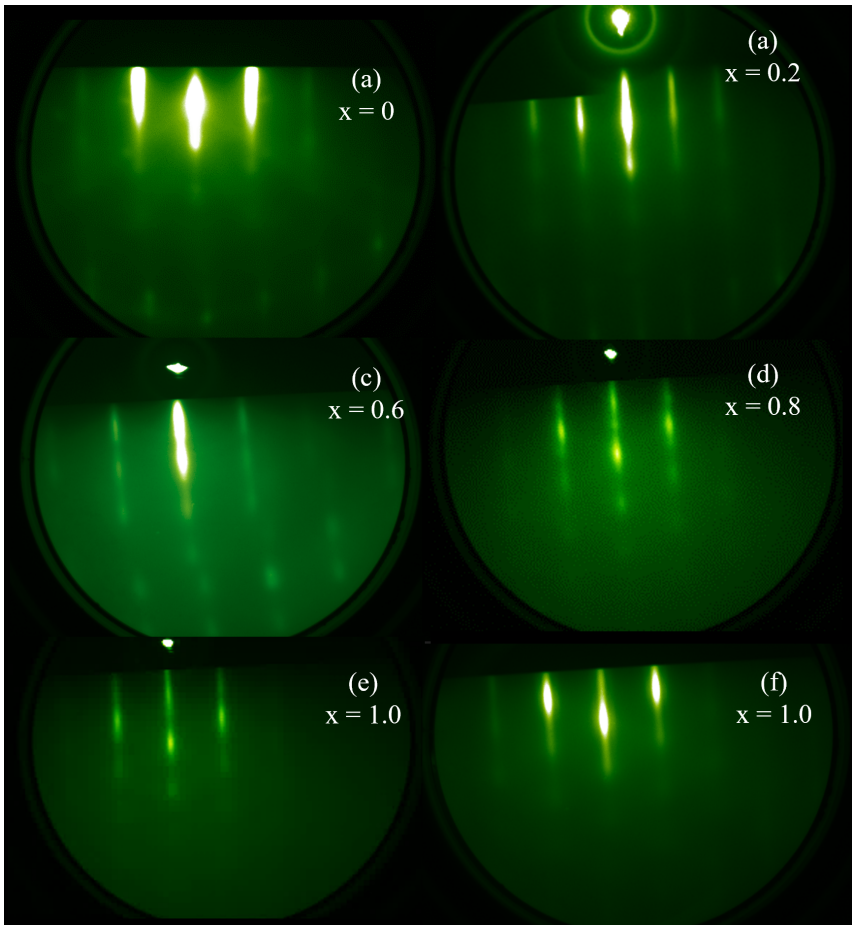

Figure 3.1: RHEED patterns of six representative NiF_2, MnF_2, and $Mn_xNi_{1-x}F_2$ thin films. The MnF_2 film shown in (e) was grown directly on a MgF_2 substrate, while the MnF_2 film shown in (f) was grown with the aid of graded $(MnNi)F_2$ buffer layer.

these MnF_2 thin films, and states an inverse relationship between the FWHM broadening the crystallite size. Rocking curves of the (220) diffraction peak of the strained and relaxed MnF_2 films are shown in Fig 3.2. Gaussian fits to the peaks to extract the FWHM indicate a 20% improvement to the crystallite size in the relaxed MnF_2 films grown with the aid of the $(MnNi)F_2$ graded buffer layer. Further discussion of the strain difference between these two types of films is presented layer in this section.

XRD measurements of the $Mn_xNi_{1-x}F_2$ thin films showed that the films grew

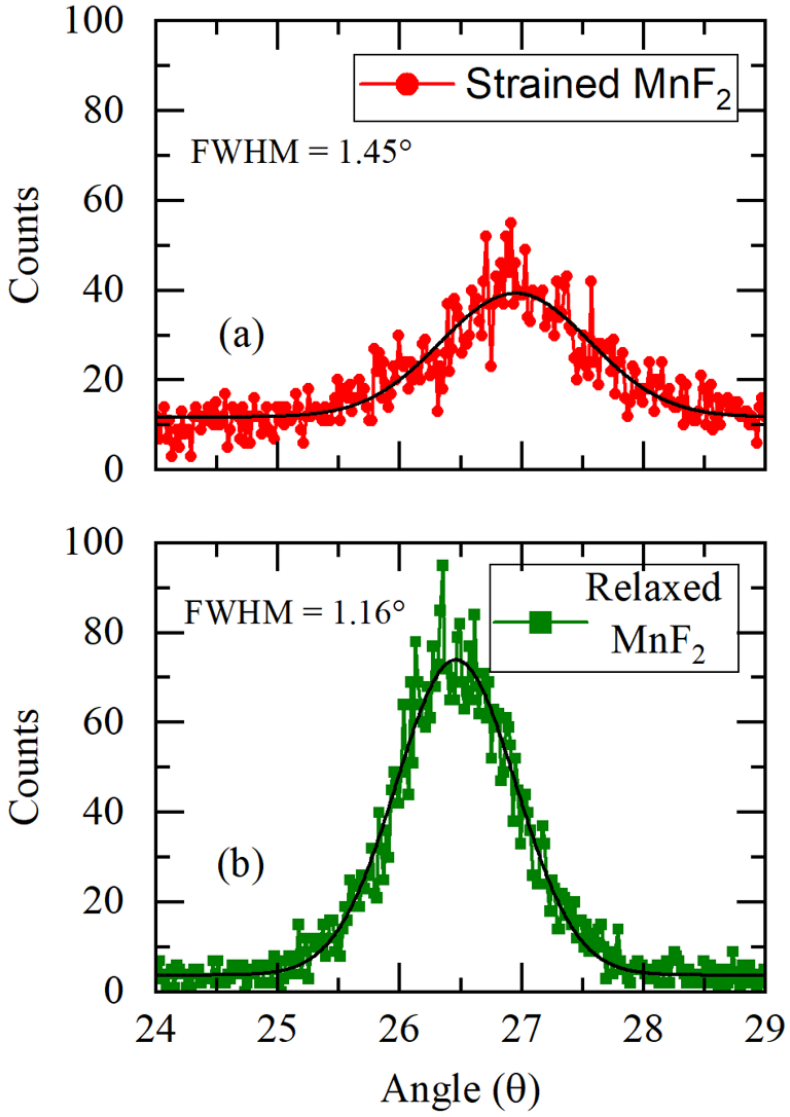

Figure 3.2: Rocking curve measurements of the (220) diffraction peak of (a) strained MnF_2 thin film and (b) relaxed MnF_2 thin film grown with the aid of a $(MnNi)F_2$ graded buffer layer. The black line represents a Gaussian fit to the the data from which the FWHM values were derived.

in the [110] crystal orientation without any evidence of additional peaks that would indicate phase separation of the alloys into NiF_2 and MnF_2 domains, as shown in Fig 3.3. The large, narrow peaks at 27.27° and 56.27° are the (110) and (220) diffraction peaks of the MgF_2 substrate. The pure MnF_2 sample ($x = 1.0$) was measured on a more powerful Rigaku X-ray diffractometer and

thus has better signal to noise than the other samples shown. The very small peak at 44° is from the stainless-steel sample stage. The position of the (110) peak shifted to smaller angles with increasing x as shown in Fig. 3.4(a). This behavior is consistent with a smoothly mixed $Mn_xNi_{1-x}F_2$ crystal alloy, where the (110) lattice parameter corresponds to the stoichiometric average of the constituent MnF_2 and NiF_2 constituents. The (110) out-of-plane lattice parameters measured for the $Mn_xNi_{1-x}F_2$ thin films are plotted in Fig. 3.4(b), along with the the expected (110) lattice parameters of bulk MnF_2 and NiF_2 [49, 63]. The calculated lattice parameter values are consistent with the claim that there is no phase separation in the $Mn_xNi_{1-x}F_2$ thin film alloys, as the calculated values fit nicely along a linear trend line between the $x = 0$ and $x = 1$ thin films, shown as the solid red line in Fig. 3.4(b).

Table 3.1: Bulk lattice parameters of MgF_2, NiF_2, and MnF_2, from ref [49, 64] and calculated values of d_{110} in thin films from out-of-plane XRD. Lattice units are in Å.

Material	bulk d_{110}	bulk d_{001}	film d_{110}
MgF_2	3.268	3.052	N/A
NiF_2	3.289	3.084	3.300 ± 0.002
MnF_2	3.446	3.310	3.426 ± 0.007

Note that the lattice parameters of the pure NiF_2 and MnF_2 endpoint samples in Fig. 3.4(b), are different from the lattice parameters of their respective bulk values. This lattice strain in the thin film samples is due to epitaxial growth on the MgF_2 substrate, which has a smaller unit cell than either NiF_2 or MnF_2. Our XRD measurements indicate that there is tensile strain along the [110] growth direction in NiF_2 (110) thin films grown on MgF_2 (110), in agreement with previous studies [65]. The NiF_2 film experiences in plane compressive strain along the c axis due to epitaxial growth on the smaller MgF_2 substrate, while it expands slightly along the [110] direction to accommodate this compression.

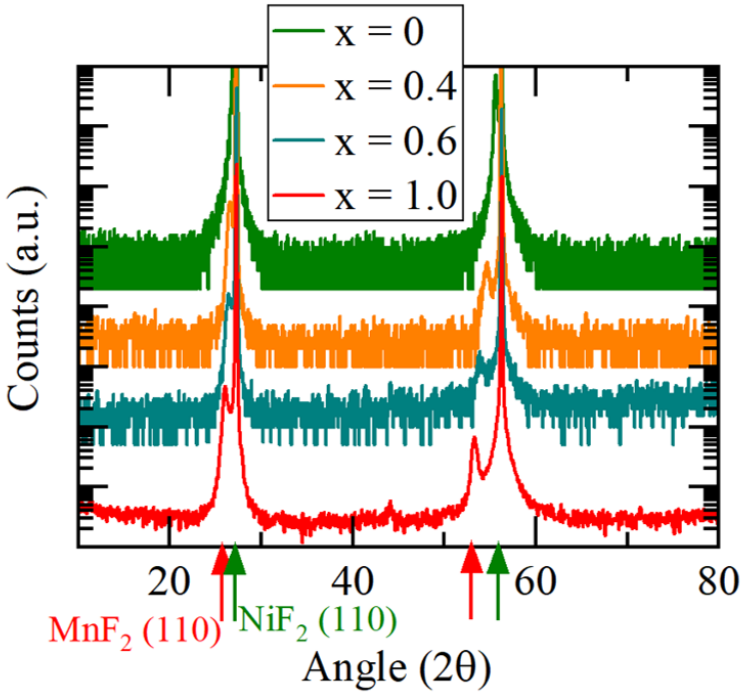

Figure 3.3: XRD pattern of four representative $Mn_xNi_{1-x}F_2$ thin films grown on MgF_2 without a graded buffer layer. The red and green arrows indicate the expected positions of the (110) and (220) diffraction peaks of MnF2 and NiF2, respectively. The very small peak at approximately 44° in the $x = 0$ sample is due to stainless-steel from the XRD stage.

Something unusual happens in the case of MnF_2 grown on MgF_2, as XRD measurements indicate that the crystal compresses along the [110] direction, contrary to the behavior observed in NiF_2. Careful x-ray measurements of the out-of-plane diffraction peaks [the (110) peak] and peaks with in-plane components of the scattering vector [the (111) and (211) peaks, shown in Fig 3.5] allowed us to calculate all three unit cell axes. These values are given in Table 3.2. Our results indicate that the MnF_2 thin film is compressed along all three crystallographic directions due to epitaxial growth on the MgF_2 substrate. This is unusual as the expected behavior from crystals under strain is that the lattice will expand along some axes to compensate for compression

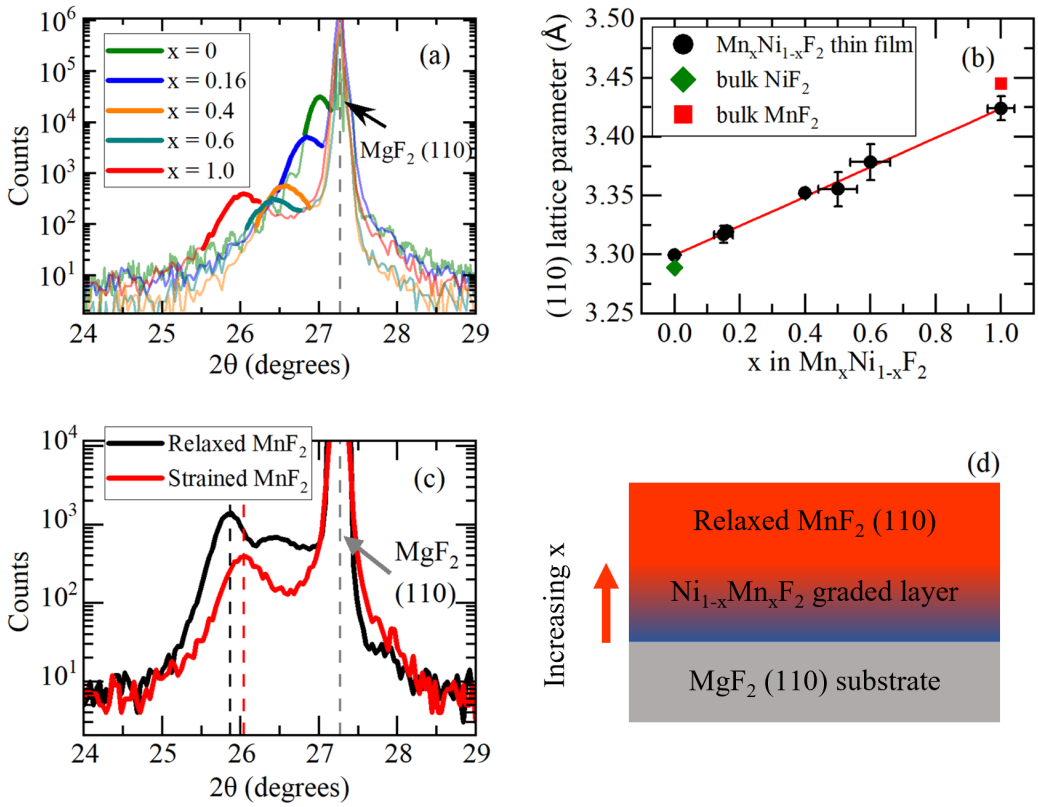

Figure 3.4: (a) XRD pattern near the (110) peak of the MgF_2 substrate and $Mn_xNi_{1-x}F_2$ thin films. (b) Calculated (110) lattice parameter as a function of Mn stoichiometry x. Solid red line is a linear fit to the thin film data. Bulk (110) lattice parameters of NiF_2 and MnF_2 are represented as the green diamond and red square, respectively. (c) XRD pattern near the (110) peak of strained and relaxed MnF_2 thin films. (d) Diagram of the relaxed MnF_2 thin film sample using a $(MnNi)F_2$ graded buffer layer.

along others in order to maintain the same unit cell volume. Our measurements indicate that the unit cell volume actually decreases by a small amount due to compressive strain along all axes. This behavior is possibly explained by the (110) crystal orientation epitaxial growth. The (110) face of the crystal has both the [001] and the $[1\bar{1}0]$ crystallographic directions lying in plane with the MgF_2 (110) substrate. The epitaxial growth could result in both the [001] and $[1\bar{1}0]$ axes feeling compressive strain at the interface and thus result in

a MnF_2 thin film crystal with a reduced unit cell volume. While these XRD measurements were performed at room temperature well above the magnetic transition, it is reasonable to assume that the difference in strain between the two MnF_2 thin films remains even at low temperature. Future work could investigate how the crystal structure changes as a function of temperature, particularly near the Néel temperature, to test this assumption. How this strain affects the magnetization of the MnF_2 film will be discussed below.

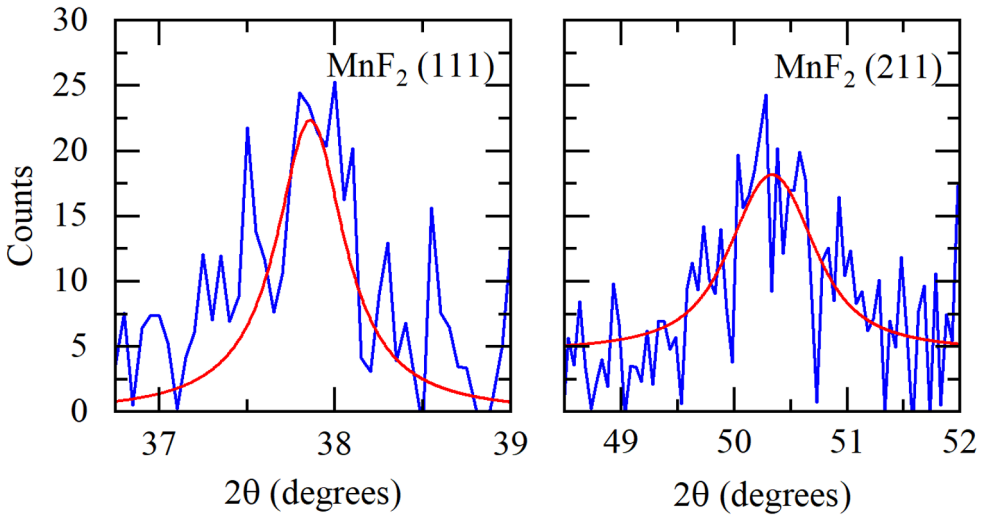

Figure 3.5: In-plane XRD peaks (111) and (211) of MnF_2 thin film grown on MgF_2, with the Voigt fit line shown in red.

Table 3.2: Lattice parameters of relaxed MnF_2 from reference [49] and strained thin film MnF_2 grown for this study. Lattice units are in Å.

Material	a	b	c
Bulk MnF_2	4.873	4.873	3.310
Thin film MnF_2	4.852 ± 0.007	4.848 ± 0.007	3.291 ± 0.004

Scans of reciprocal space near the in plane (111) peaks of the strained and relaxed MnF_2 thin films reveals an additional effect of the epitaxial strain. The reciprocal space map (RSM) of the strained MnF_2 film shown in Fig. 3.6(a) shows two MnF_2 (111) diffraction peaks due to crystal twinning in the plane. When the epitaxial strain is eliminated with the use of the $(MnNi)F_2$ graded

buffer layer and the MnF_2 thin film is relaxed, the twinning disappears, as shown in Fig. 3.6(b). The in plane crystal twinning in the strained film is likely a consequence of the lattice mismatch with the MgF_2 substrate and the corresponding epitaxial strain as the MnF_2 thin film tries to alleviate the strain by breaking into these twinned crystal domains.

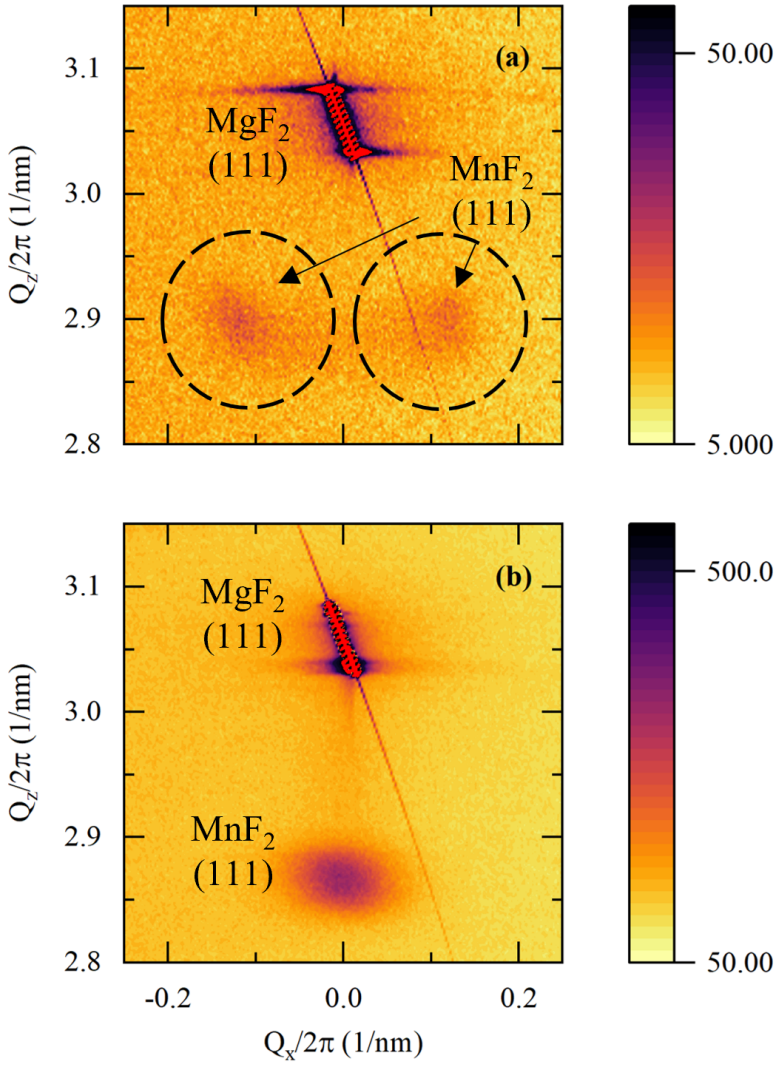

Figure 3.6: Reciprocal space map of the in plane (111) diffraction peak of (a) strained MnF_2 thin film grown on MgF_2 and (b) relaxed MnF_2 thin film grown with the use of the graded $(MnNi)F_2$ buffer layer.

In order to test if the observed strain was due to epitaxial growth on the smaller unit cell of MgF_2 and how this affects the magnetism of the film,

comparison with a relaxed MnF_2 thin film is necessary. The strain observed in MnF_2 thin films grown on MgF_2 can be eliminated by the use of a $(MnNi)F_2$ graded layer as a buffer between the substrate and the MnF_2 thin film, as shown in Fig. 3.4(d) and described in the Methods section above. By gradually increasing the Mn stoichiometry x in the buffer layer with increasing thickness, the lattice parameters of the buffer layer slowly increased, ultimately resulting in a relaxed MnF_2 thin film with improved crystallinity, as shown by XRD measurements in Fig. 3.4(c). It is unlikely that there is a sharp boundary between the $(MnNi)F_2$ graded layer and the pure MnF_2 layer, because the growth of the $(MnNi)F_2$ graded layer growth is designed in such a way that the layer smoothly transitions from NiF_2 to MnF_2 as it gradually changes the lattice parameter of the film to reduce strain between the substrate and the MnF_2 film, although further measurements such as transmission electron microscopy or x-ray photoelectron spectroscopy would be needed to verify the structure. A comparison of the magnetic behavior of the strained MnF_2 film with the relaxed film will be presented in the next section.

3.3.2 Magnetization

Field-cooled (FC) Magnetic moment measurements of the strained and relaxed MnF_2 thin films along the c-axis are shown in Fig. 3.7(a), revealing a shift in the transition temperature between these two films. FC measurements are performed by warming the sample above the Néel temperature to $T = 100$ K then setting the external magnetic field to $\mu_0 H = 0.1$ T and measuring the moment as the sample is cooled. Although it may be expected that MnF_2 would have no net magnetic moment along c-axis below the Néel temperature because it is an easy-axis antiferromagnet, it has been shown previously that strain in the crystal will cause a net moment to develop along the c-axis, as is observed

here [59, 61, 65]. Plotting the transition temperature as a function of the (110) lattice parameter in Fig. 3.7(b), demonstrates the existence of a piezomagnetic effect in MnF_2 thin films. In $\sim 0.5\%$ strained MnF_2, the transition temperature decreases by nearly 7 K. When the strain in the MnF_2 thin film was fully relaxed (by growing on a $(MnNi)F_2$ graded layer), the transition temperature matched the bulk value of 66.5 K. The graded buffer layer method used here suggests that the epitaxy-induced strain could be carefully tuned by controlling the final stoichiometry of the $(MnNi)F_2$ graded buffer layer, changing the lattice mismatch at the MnF_2 interface and permitting some control of the piezomagnetic behavior in thin film MnF_2. It is important to note here that it is difficult to differentiate magnetic moment contributions from the $(MnNi)F_2$ graded layer from the magnetic moment of the pure MnF_2 film itself. By its very nature, the $(MnNi)F_2$ graded layer has some thickness (less than 10 nm) that is either pure MnF_2 or lightly doped with NiF_2 that will contribute to the overall magnetization. It is unclear from these magnetic susceptibility measurements if the net moment in the relaxed MnF_2 film is due to interactions with the $(MnNi)F_2$ graded buffer layer or from some uncompensated strain in the MnF_2 thin film crystal. However, the fact that the transition temperature of the film agrees with the expected bulk value suggests that the magnetism is dominated by a relaxed, pure MnF_2 film. The other $Mn_xNi_{1-x}F_2$ thin films with fixed values of x, discussed below, were not grown with the $(MnNi)F_2$ graded buffer layer and therefore retain some epitaxial strain.

In order to study the magnetic properties of the $Mn_xNi_{1-x}F_2$ thin film alloys, two sets of in-plane, field-cooled (FC) thermoremanent magnetization (TRM) measurements were performed as a function of temperature. In the c-axis measurements, shown in Fig. 3.8(a), the samples were cooled from $T = 100$ K to $T = 4.5$ K in a small external field ($\mu_0 H = 0.1$ T) applied in the film of the

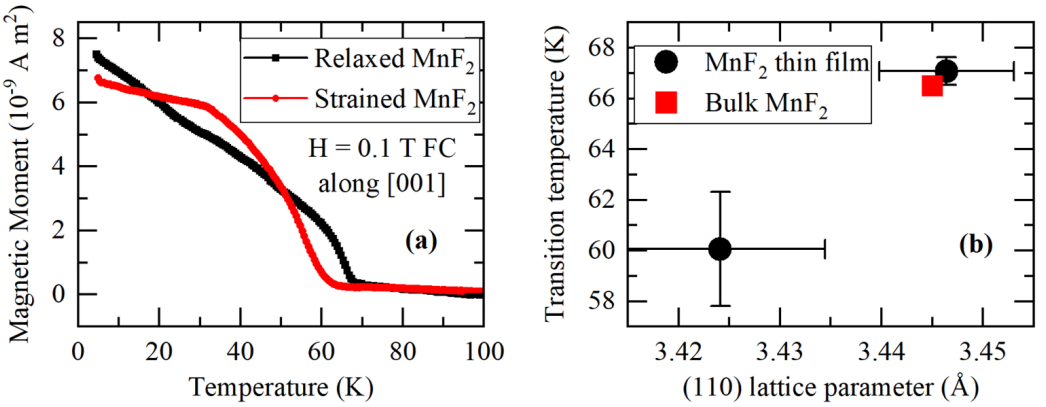

Figure 3.7: (a) Magnetic moment measurements of strained and relaxed MnF_2 thin films field-cooled (FC) in a $\mu_0 H = 0.1$ T external magnetic field applied along the c axis.(b) magnetic transition temperature of MnF_2 thin films, relaxed and strained, and bulk MnF_2 as a function of the (110) lattice parameter.

plane along the c-axis of the $Mn_xNi_{1-x}F_2$ thin film crystal. Upon reaching $T = 4.5$ K, the external field is turned off and the magnetic moment is measured along the c-axis as the temperature is increased. In Fig. 3.8(b), the samples are cooled and measured in the same way, but the external field and measured moment are oriented 90° in-plane relative to the [001] (c-axis) direction to measure the moment along the in-plane $[1\bar{1}0]$ direction of the $Mn_xNi_{1-x}F_2$ thin film crystal. Figure 3.8(a) shows the development of a net magnetic moment along the c-axis of the $Mn_xNi_{1-x}F_2$ thin film crystal as the stoichiometry x is varied. At small values of x, the film has little or no net moment along the [001] direction, as would be expected for a NiF_2 film [10, 65]. As the MnF_2 stoichiometry x is increased further, a net moment develops along the [001] direction due to strain in the thin film crystal [59, 61, 65]. In contrast, Fig. 3.8(b) shows the net magnetic moment along the in-plane $[1\bar{1}0]$ direction, which lies in the $a-b$ plane of the crystal. In this direction there is a large net moment even for small values of x due to the DMI induced canted moment in NiF_2 [8]. This net moment gradually decreases as x is increased and the thin

film alloy behaves more like pure MnF_2.

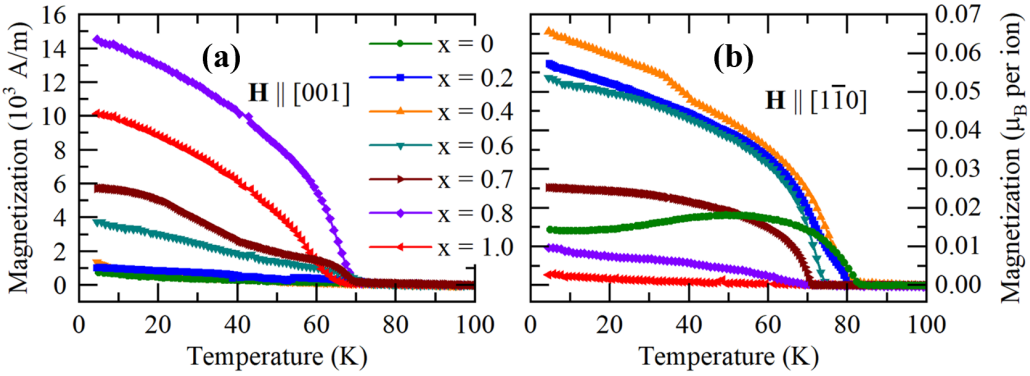

Figure 3.8: TRM as a function of temperature of $Mn_xNi_{1-x}F_2$ thin films (a) measured along the [001] (c-axis) and (b) along the [1$\bar{1}$0] in-plane crystallographic directions of the samples, both of which are in the plane of the samples. The cooling external field $\mu_0 H = 0.1$ T was applied along the direction of measurement.

Measurements of the magnetization while sweeping the applied magnetic field reveal unique hysteresis behavior in the $Mn_xNi_{1-x}F_2$ thin films with certain stoichiometries, as shown in Fig. 3.9, which shows the magnetization of the film with a linear paramagnetic background subtracted. The $Mn_{0.2}Ni_{0.8}F_2$ film shown in Fig. 3.9(a) exhibits an unusually large coercive field for this material, with the magnetic moment not fully saturating until nearly 2 T.

In addition to the ordinary AF transition in $Mn_xNi_{1-x}F_2$ thin films, magnetization measurements also show evidence of a second magnetic transition along the [1$\bar{1}$0] direction in some $Mn_xNi_{1-x}F_2$ samples. Figure 3.10 shows TRM and the first derivative of the TRM as a function of temperature for several stoichiometries of $Mn_xNi_{1-x}F_2$ films. Films shown in Fig. 3.10(a-d) are measured along the [1$\bar{1}$0] direction, while those shown in Fig. 3.10(e,f) are measured along the c-axis. A second magnetic transition can be identified by an inflection in the magnetization as a function of temperature, and is easily distinguished in

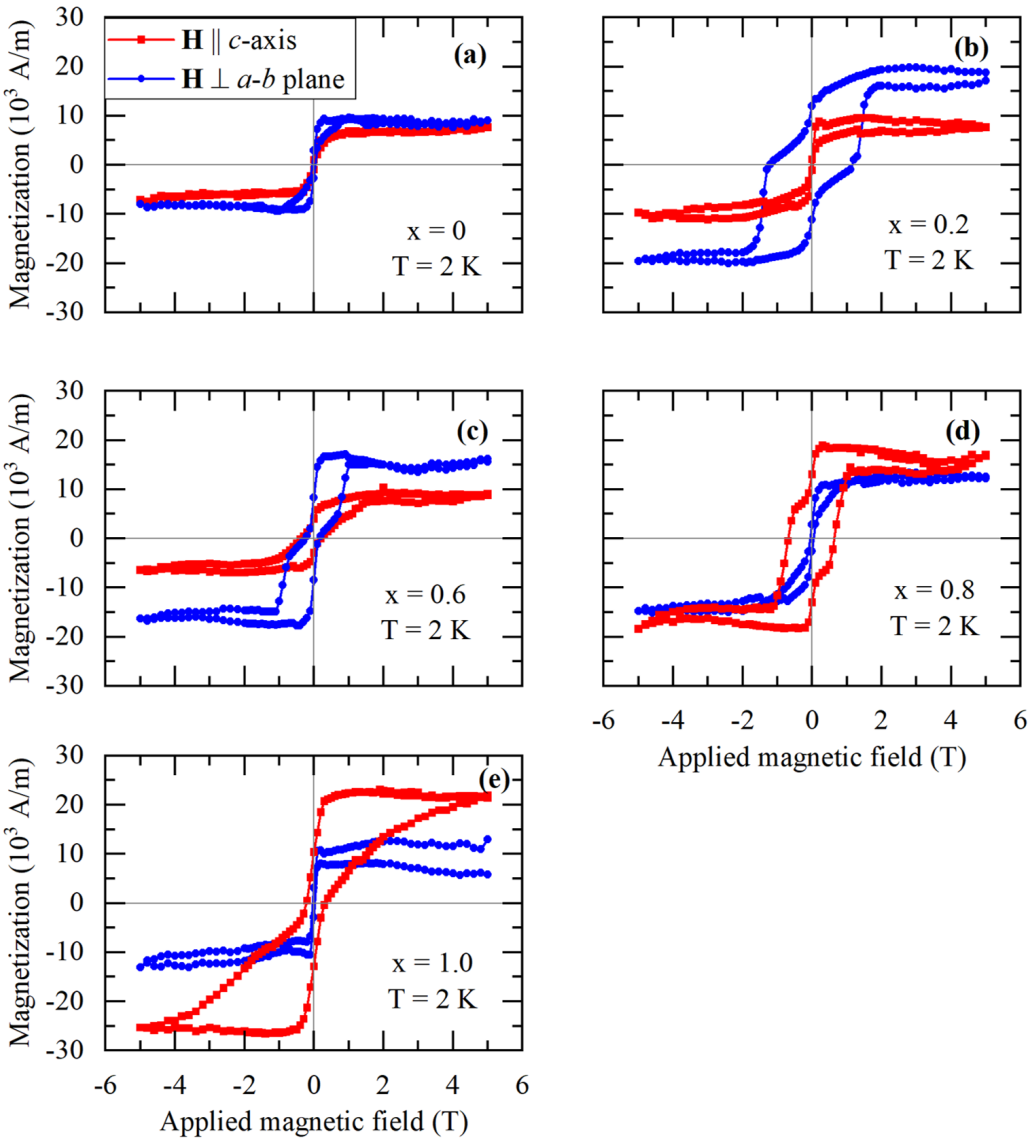

Figure 3.9: Magnetization along the two in plane directions as a function of the applied magnetic field for several $Mn_xNi_{1-x}F_2$ films at $T = 2$ K. A linear paramagnetic background has been subtracted from each sample.

the first derivative of the magnetization, as shown in Fig. 3.10(b), where two magnetic transitions are labeled. The ordinary AF transition is labeled as T_2, and the additional emergent phase is labeled as T_1.

The magnetization data can be understood in terms of the MFT approximation

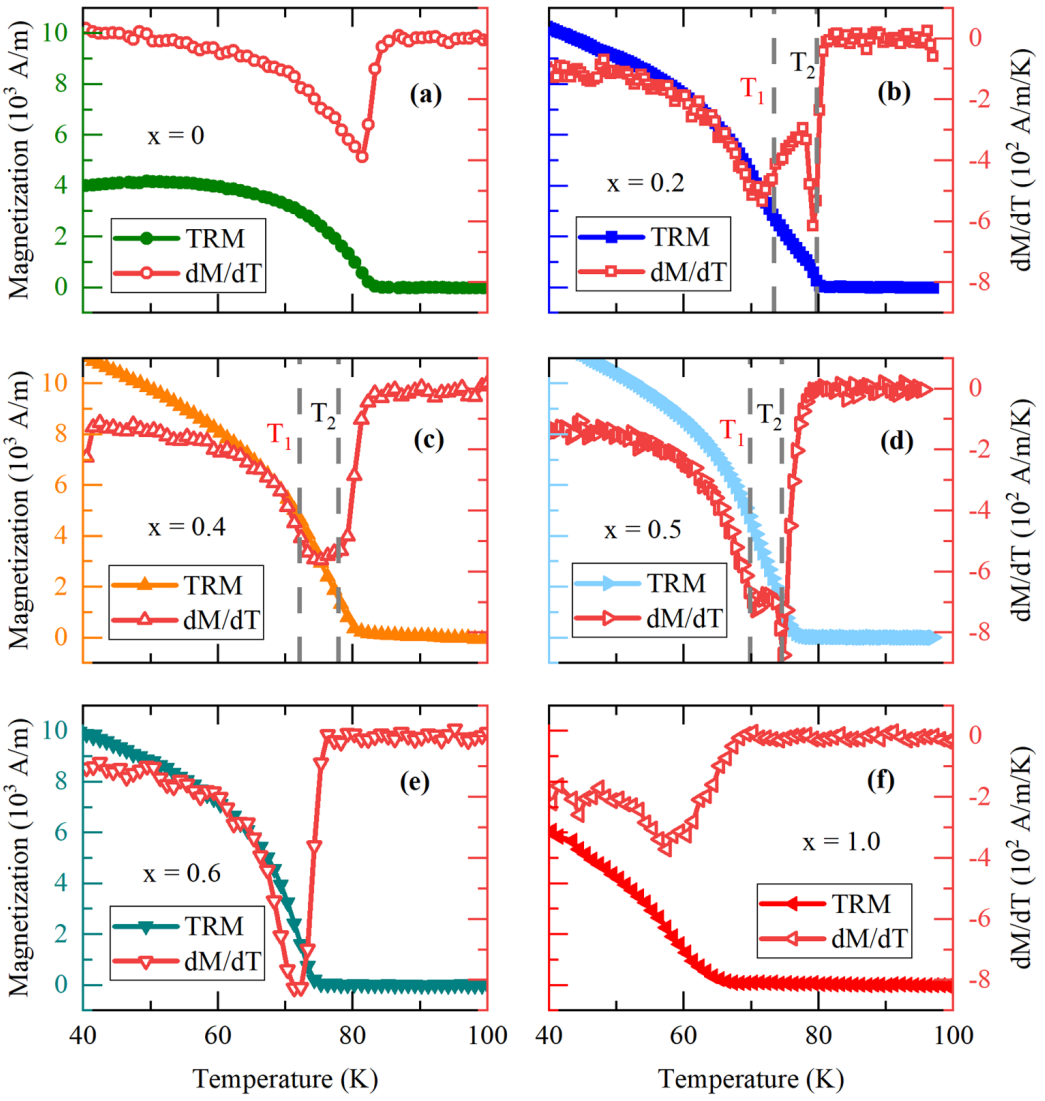

Figure 3.10: TRM and first derivative of TRM with respect to T of selected samples with different values of x. The sample with $x = 0.2$ (b), $x = 0.4$ (c), and $x = 0.5$ (d), show two inflection points in the TRM associated with a second magnetic transition.

presented in Section 1.2. First consider the spin Hamiltonian [10]

$$H = \sum_{i=1} \sum_{j=i+1} J_{ij} \mathbf{S}_i \cdot \mathbf{S}_j + D \sum_i (S_i^z)^2 + E \left[\sum_i (S_{ix}^2 - S_{iy}^2) - \sum_j (S_{jx}^2 - S_{jy}^2) \right], \tag{3.2}$$

where J_{ij} is the next nearest neighbor exchange energy between spins at lattice

sites i and j, D is the single-ion magnetic anisotropy energy, and E is an antisymmetric exchange energy that cants moments in the x-y plane. For the rutile structure, the z-direction coincides with the c-axis of the crystal. The known values of the spin, exchange and anisotropy energies for MnF_2, NiF_2, and FeF_2 are given in Table 3.3.

Table 3.3: Spin S of the transition metal ion and magnetic exchange energies J, single-ion anisotropy energies D, and the rhombic (DM) anisotropy energy E of MnF_2, NiF_2, and FeF_2 bulk crystals [54, 58, 66]. The mean-field value of $J\langle S^2\rangle = JS(S+1)/3$, which is proportional to the mean-field Néel temperature, is also included for reference. Energy units are in meV.

Material	S	J	$JS(S+1)/3$	D	E
MnF_2	5/2	0.304	0.887	-0.096	0
NiF_2	1	1.719	1.146	0.541	0.205
FeF_2	2	0.451	0.902	-0.801	0

Previous studies on $Fe_xNi_{1-x}F_2$ thin films have observed a similar emergent magnetic phase to that observed in Fig 3.10 in magnetization measurements as a function of temperature [48]. Neutron diffraction measurements of the magnetic (100) and (001) peaks showed that this state is neither the uniaxial ordering of FeF_2 (similar to that of MnF_2) nor the planar ordering of NiF_2 [48]. These observations indicate that the emergent phase could consist of a magnetic glassy state [48], or, another possibility that we propose here, a helical or skyrmion phase. A skyrmion phase is hypothetically possible in this system because NiF_2 is known to exhibit DMI, an antisymmetric or anisotropic exchange that tends to cant magnetic moments out of antiparallel alignment and is an important ingredient in the stabilization of chiral spin textures [5, 52, 67]. Verifying the latter hypothesis of a skyrmion phase requires further experimentation beyond the scope of this paper, but it could be investigated in the future with neutron scattering measurements, to check for the formation of a skyrmion lattice, or by Raman scattering measurements to check for additional magnon modes associated with either the skyrmion phase or a spin

glass phase.[6, 68, 69].

From the TRM measurements of the $Mn_xNi_{1-x}F_2$ samples, a magnetic phase diagram of the system is constructed and is shown in Fig. 3.11. The solid blue curve is a fit to Eq. 1.20. Fitting the measured transition temperatures to this equation yields a value for T_{AB} which can then be used to calculate the exchange integral J_{AB} between the elements of the mixed system, according to Eq. 1.21. This expression takes into account only the antiferromagnetic exchange between next-nearest-neighbors (between center and corner spins in the rutile structure), which is a reasonable simplification to make for MnF_2 and NiF_2 because the omitted nearest-neighbor coupling is nearly 10 times smaller than the next-nearest-neighbor coupling [54, 66]. From Eq. 1.21, the exchange constant between Mn and Ni ions on opposite sublattices in our films is calculated to be $J_{\text{Mn-Ni, film}} = 0.305 \pm 0.003$ meV. Assuming that the transition temperatures in the films are due to a modified value of the exchange constants resulting from strain and that the transition temperature varies linearly with the exchange constant, the values of the exchange constants in our samples are approximately $J_{\text{Mn-Mn, film}} = 0.274$ meV and $J_{\text{Ni-Ni, film}} = 1.897$ meV, compared to experimentally determined values of $J_{\text{Mn-Mn, bulk}} = 0.304 \pm 0.002$ meV in bulk MnF_2 [70] and $J_{\text{Ni-Ni, bulk}} = 1.719 \pm 0.045$ meV in bulk NiF_2 [66]. It is the exchange constant $J_{\text{Mn-Ni}}$ that is primarily responsible for the shape of the paramagnetic-AF transition in the phase diagram Fig. 3.11.

At low Mn stoichiometries ($x < 0.6$) and below the AF transition temperature T_2, the magnetic moments order antiferromagnetically in the *a*-*b* plane ($AF_{\text{a-b}}$), similarly to how they order in NiF_2. The $AF_{\text{a-b}}$ phase exists over a much larger range of stoichiometries than in the $Fe_xNi_{1-x}F_2$ system because of the difference in magnetic anisotropy energy D between the Ni and Mn ions, with D_{NiF_2} being more than 5 times larger than D_{MnF_2}. Within this range of

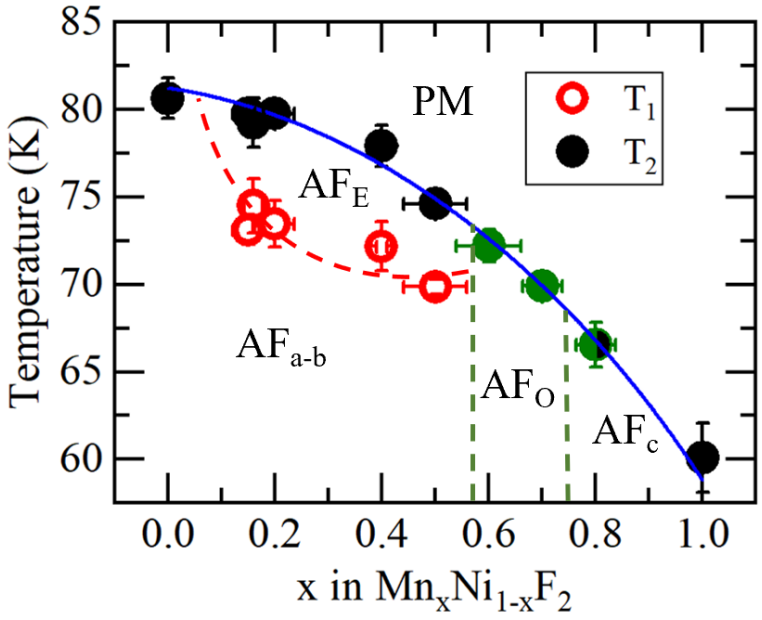

Figure 3.11: Magnetic phase diagram of $Mn_xNi_{1-x}F_2$ thin films divided into five regions for each phase: PM for the paramagnetic phase, $AF_{a\text{-}b}$ for antiferromagnetic ordering in the $a-b$ plane, AF_E for the emergent magnetic phase, AF_O for the oblique antiferromagnetic phase, and AF_c for antiferromagnetic ordering along the c-axis. Samples exhibiting oblique AF order (that is, having a strong signal with $\vec{H}$ applied both parallel and perpendicular to the c-axis, per the data in Fig. 3.8) are colored green. The solid blue curve represents a fit to MFT. The green dashed lines indicate the region where oblique AF order is predicted to exist from MFT using the parameters given in Table 3.4. The red dashed curve is a guide to the eye approximating the emergent magnetic phase boundary from TRM measurements.

$AF_{a\text{-}b}$ magnetic ordering, the emergent magnetic phase (AF_E) develops in the temperature range between T_1 and T_2, as indicated by the red dashed curve in Fig. 3.11. As Mn stoichiometry is increased, the AF ordering enters an oblique AF phase (AF_O), where competition between the mutually orthogonal magnetic anisotropies of MnF_2 and NiF_2 causes the Néel vector to point along some angle θ between 0° and 90° with respect to the a-b plane of the crystal.

Samples which have strong TRM along both the c-axis and perpendicular to it are samples which have the oblique phase, that is, samples with $x = 0.6$ and $x = 0.7$ in Fig. 3.8. The sample with $x = 0.8$ is close to the AF_O phase but the small TRM in the a-b plane relative to the TRM along the c axis leads us to conclude that this sample lies just outside the boundary of the AF_O phase. Beyond $x = 0.8$, the system transitions into the uniaxial AF state ordering along the c-axis (AF_c) as in pure MnF_2.

The oblique AF phase can be described theoretically by MFT as presented in the Section 1.2, following the MFT procedure used in references [26, 48]. The angles θ_A and θ_B that the ions A and B make with respect to the c-axis are given by the system of equations

$$\tan\theta_A = \frac{z(J_{AA}p_AS_A\sin\theta_A + J_{AB}p_BS_B\sin\theta_B)}{z(J_{AA}p_AS_A\cos\theta_A + J_{AB}p_BS_B\cos\theta_B) - 2D_AS_A\cos\theta_A} \tag{3.3a}$$

$$\tan\theta_B = \frac{z(J_{BB}p_BS_B\sin\theta_B + J_{AB}p_AS_A\sin\theta_A)}{z(J_{BB}p_BS_B\cos\theta_B + J_{AB}p_AS_A\cos\theta_A) - 2D_BS_B\cos\theta_B} \tag{3.3b}$$

where z is the number of next-nearest neighbors in the lattice. For the rutile crystal structure $z = 8$.

This general model of the easy axis for two anisotropic antiferromagnets successfully explains the oblique AF phase of $Fe_xNi_{1-x}F_2$ from reference [48], predicting a stoichiometric region of $0.09 \leq x \leq 0.21$. Using our experimentally-determined values for the exchange and anisotropy constants for the $Mn_xNi_{1-x}F_2$ system in this model predicts the existence of an oblique AF region in the stoichiometric region $0.40 \leq x \leq 0.58$, which is different from the experimentally observed oblique AF region of approximately $0.6 \leq x \leq 0.8$. One potentially important factor that is not captured by the MFT approximation is the unusual strain observed in the thin film MnF_2, where the crystal lattice is compressed

along all three crystallographic axes. It is known that changes in the lattice spacing and unit cell volume will affect the magnetic exchange energy J, [65, 71], but the location of the oblique phase is not very sensitive to the exchange constants, per our mean field calculations. On the other hand, the stoichiometric region of oblique AF order is sensitive to changes in the anisotropy energy D. Decreasing the magnitude of the Mn anisotropy energy has the effect of shifting the AF_O-AF_c phase transition to larger x, while increasing the magnitude of Ni anisotropy energy has the effect of shifting the $AF_{a\text{-}b}$-AF_O phase transition to larger x. Increasing the overall absolute value of anisotropy energy in the system has the effect of increasing the range of the oblique phase in x. By decreasing the Mn anisotropy energy to $D_{MnF_2} = -0.06$ meV and increasing the Ni anisotropy energy to $D_{NiF_2} = 0.74$ meV, MFT indicates the presence of an oblique AF phase in the region $0.58 \leq x \leq 0.75$ at $T = 0$, which agrees with the experimentally observed phase. It is possible that the compressive strain observed in thin film MnF_2 also affects the structure of the $Mn_xNi_{1-x}F_2$ alloy thin films as x increases and that this transition changes the anisotropy energy of the constituent Mn^{2+} ions. One possible reason is that in MnF_2 the single-ion anisotropy is primarily a result of dipole-dipole interactions because the orbital angular momentum of the ground state Mn^{2+} is zero [72], so changing the lattice parameters of the unit cell, and thus increasing or decreasing the strength of the dipole-dipole interaction between neighbors, could have a significant effect on the magnitude of the single-ion anisotropy. A summary of the parameters used to reproduce our experimental data are shown in Table 3.4.

The $Mn_xNi_{1-x}F_2$ system can be compared to a similar system, $Fe_xNi_{1-x}F_2$, to obtain some insight into the effects that the magnetic energy parameters have on the phase diagram of the system [48]. FeF_2 has the same rutile crystal

Table 3.4: Symbols, meaning, and values used to reproduce our experimental data from Eqs. 1.20, 1.21, and 3.3.

Symbol	Meaning	Value
S_A	S_{MnF_2}	5/2
S_B	S_{NiF_2}	1
J_{AA}	J_{MnMn}	0.274 meV
J_{BB}	J_{NiNi}	1.897 meV
J_{AB}	J_{MnNi}	0.305 meV
D_A	D_{Mn}	-0.06 meV
D_B	D_{Ni}	0.74 meV
p_A	x	0-1 range
p_B	$1-x$	1-0 range

structure and c-axis AF order as MnF_2, but the magnetic anisotropy energy is nearly 10 times larger than in MnF_2, as shown in Table 3.3. Note that the effective exchange interaction, proportional to $JS(S+1)/3$, is similar in MnF_2, NiF_2, and FeF_2, and therefore the overwhelming difference between the three systems is the single-ion anisotropy. This makes comparison between $Mn_xNi_{1-x}F_2$, where the anisotropy is small, and $Fe_xNi_{1-x}F_2$, where the anisotropy is large, enlightening because it illustrates the large effect that the single-ion anisotropy has in modifying the phase diagram. Specifically, the magnitude of the single-ion anisotropy energy appears to play a major role in the size of the oblique AF phase with respect to the stoichiometry. In $Fe_xNi_{1-x}F_2$, the oblique phase is relatively small, while in $Mn_xNi_{1-x}F_2$, with an order of magnitude smaller single-ion anisotropy, the oblique AF phase persists over a large range of stoichiometry. This behavior is both predicted by MFT and experimentally observed in magnetic susceptibility measurements of the two systems.

It is also interesting to note that as the oblique phase grows in phase space in $Mn_xNi_{1-x}F_2$, the emergent phase shrinks in phase space relative to $Fe_xNi_{1-x}F_2$ [48]. This implies some relationship between the two magnetic states, further suggested by the fact that in both systems, $Mn_xNi_{1-x}F_2$ and $Fe_xNi_{1-x}F_2$, there

exists a tricritical point between the emergent, oblique, and anisotropic AF phases, located at $x \approx 0.58$ and $x \approx 0.20$, in the $Mn_xNi_{1-x}F_2$ and $Fe_xNi_{1-x}F_2$, respectively [48].

3.3.3 Summary

In summary of the findings of this work, it has been demonstrated how an antiferromagnetic system composed of two species with competing single-ion anisotropies, embodied by $Mn_xNi_{1-x}F_2$ alloy thin films grown via MBE, has a rich magnetic phase diagram. The $Mn_xNi_{1-x}F_2$ thin film alloys retain their antiferromagnetic ordering as the magnetic transition temperature and lattice parameters vary with changing stoichiometry. At $x = 1.0$, the MnF_2 thin films are strained in all three directions due to epitaxial growth on MgF_2 substrates, and as a result the AF transition temperature is reduced by 7 K.

Using magnetization measurements of the $Mn_xNi_{1-x}F_2$ thin film alloys along their two in plane directions, $[1\bar{1}0]$ (in the a-b plane) and [001] (along the c-axis), a magnetic phase diagram was constructed. MFT fits to the antiferromagnetic transition temperature enable calculation of the magnetic exchange energy between the Mn and Ni ions to be $J_{\text{Mn-Ni}} = 0.305 \pm 0.003\,\text{meV}$. A MFT approximation was used to predict the existence of an oblique AF phase observed in the experimental magnetization measurements. Agreement with the experimental data also requires a decrease in the single-ion anisotropy in MnF_2 with respect to the bulk material, possibly as a result of the strain induced by the epitaxial growth of the films on the MgF_2. The oblique AF phase shares a tricritical point with the NiF_2-like anisotropic AF phase and an emergent magnetic phase with unidentified structure. This emergent magnetic phase could be a magnetic glassy phase or a helical (or possibly skyrmion) phase. Further experimental and theoretical work needs to be performed to identify

the structure of the emergent phase in this system.

Chapter 4

Magnetic topological insulator - antiferromagnetic insulator bilayers

4.1 Introduction

Topological insulators (TIs) are a fascinating group of materials that host a great variety of exotic quantum behaviors, such as spin Hall effects, electronic Dirac states, and weak antilocalization, among others. When the non-magnetic TI is exposed to a magnetic moment, either through an externally applied field or (more interestingly) by inducing intrinsic magnetic order in the TI itself, then there emerge yet more quantum behaviors with interesting and potentially useful applications. One such quantum state manifests in the widely studied quantum anomalous Hall effect (QAHE) [23, 24]. The QAHE is an analog to the quantum Hall effect that exhibits a quantized Hall resistance and dissipation-less edge states but without the need to apply a large external magnetic field, instead relying on the spontaneous magnetic moment of the

system to create the observed effects. Another of these special quantum states discovered in a magnetic TI is observed via the topological Hall effect (THE), which is associated with the formation of a skyrmion-like magnetic phase at the surface of the material [24, 73]. The QAHE and THE both have potential technological applications in topological spintronics [4]. The discovery of these states suggests a rich parameter space in which to probe quantum mechanical effects in the magnetic TI, with sample geometry, chemical potential, and magnetic ordering all playing important roles.

There have emerged three primary strategies for inducing a spontaneous moment in the surface states of TI, each with perceived strengths and weaknesses. The first is by proximity to a magnetic insulator, usually through the fabrication of a heterostructure of two different materials with an atomically smooth interface which creates some overlap in the electronic and spin states of the two systems. Inducing magnetism by proximity effects has the advantage of maintaining a high crystal quality of the TI, but is limited by a perceived lack of materials that have magnetic and topological properties and which can also support the growth of the TI-magnetic insulator heterostructure [74]. The second method involves the search for, and growth of, novel TI materials that have some magnetic order as a consequence of their crystal structure, such as in $MnBi_2Te_4$ [75]. These materials have the great advantage of being ordered crystals, meaning there are no defects associated with inducing magnetism, however they seem to be very rare and difficult to produce. The third method is by doping the TI with magnetic impurities, usually transition metals such as Cr [23, 76, 77], Mn [78], or Fe [79]. Although the ferromagnetic moment in these systems only orders at low temperatures and the crystal quality is somewhat degraded by the introduction of magnetic dopants, this method of inducing a magnetic moment in the TI has shown the most success in mani-

festing the quantum states associated with the QAHE and the THE [23, 24], and it is these doped TI materials that this study will focus on.

Understanding the mechanism of magnetic ordering in these doped TI materials and how it is affected by microscopic and macroscopic parameters is critical to the development of these materials into technologically useful systems. In the case of ferromagnetic Mn-doped Bi_2Te_3, which has a ferromagnetic moment pointing along the [0003] crystallographic direction of the crystal (using a hexagonal basis) and a Curie temperature of $T_C \approx 16$ K, the mechanism responsible for the magnetic ordering in these materials is unclear. In Mn-doped TI films, proposed mechanisms include Mn clustering [80], Van Vleck-type susceptibility [81], and Ruderman–Kittel–Kasuya–Yosida (RKKY) interactions, either through bulk conduction channels or two dimensional (2D) surface states [73, 82, 83].

To gain insight into the mechanism of ferromagnetic ordering in the Mn-doped Bi_2Te_3 system and its behavior in parameter space, magnetic, electronic, and structural measurements are presented on a series of $Mn_{0.14}Bi_{1.86}Te_3$ (MBT) thin film crystals. Samples were grown on three different types of insulating substrates: non-magnetic Al_2O_3 and MgF_2, and antiferromagnetic NiF_2. Results show that subtle, but significant, differences in electronic and magnetic properties develop even between samples that are nominally identical in their growth conditions. By keeping the Mn concentration, film thickness, and other growth parameters constant throughout a series of thin film growths, the dependence of the magnetic and electronic properties of this system on variations in TI-substrate interface, Hall mobility, and charge carrier density are probed. This process produces evidence that the ferromagnetic ordering in this system is, in large part, electronic charge carrier mediated and that the antiferromagnetic NiF_2 interface acts to reduce magnetization in the MBT

film.

This chapter also demonstrates advancements in the fabrication novel TI-antiferromagnetic insulator bilayers using crystallographic, magnetic, and electronic characterizations of MBT films grown on epitaxial thin films of the antiferromagnetic insulator, NiF_2. Evidence is presented that single phase, (0001)-oriented hexagonal MBT films can be grown on the (110) face of tetragonal NiF_2 and MgF_2 substrates despite the significant lattice mismatch and difference in crystal structure. XRD and XRR show that the MBT films grown on NiF_2 and MgF_2 have nearly identical crystallographic properties compared to those grown on hexagonal Al_2O_3 (0001). These results suggest the existence of a much wider range of potential TI bilayer constructions with unique proximity effects that may emerge at those interfaces.

4.2 Methods

MBT films were grown via molecular beam epitaxy (MBE) in an ultra-high vacuum (UHV) chamber (base pressure $< 10^{-10}$ Torr) by sublimating from separate elemental sources of 99.999% pure Mn, Bi, and Te. Flux ratios and film thickness was determined by measuring the elemental flux rate with a retractable crystal monitor located at the same position as the sample substrate. Reflection high energy electron diffraction (RHEED) oscillations associated with layer by layer growth were measured and used to calibrate the elemental flux to film thickness ratio. Film thickness was measured using x-ray reflectivity (XRR), an independent measurement which reveals that the film thickness calibration from elemental flux had a random error of about 4%. Each sample was grown under identical conditions, keeping the Mn/Bi flux percentage at $7 \pm 1\%$ and film thickness to 13.6 ± 0.5 nm, approximately 12 quintuple layers (QL). Mn percentage was calculated by a combination of partial pressure ratios

during growth and by x-ray fluorescence measurements after growth. Seven distinct MBT samples were grown in a series of five growths or batches over the span of about five months.

For the MBT films grown on Al_2O_3 (0001), using the hexagonal close packed basis, and MgF_2 (110), commercially purchased single-crystal substrates were used. For the MBT/NiF_2 bilayers, a separate UHV chamber was used to first grow the epitaxial NiF_2 (110) film on a MgF_2 (110) substrate to a thickness of approximately 30 nm, before MBT film growth. NiF_2 MBE growths were performed using thermal sublimation of commercially available NiF_2 source material as described in Chapter 2 and elsewhere [65]. In situ RHEED patterns of all MBT films show similarly smooth, single phase, thin film crystals. All substrates were annealed at $T = 300°$ C for several hours before MBT growth to prepare a clean surface. After MBT film growth, but before removing the sample from the UHV chamber, a 5 nm thick layer of polycrystalline, insulating, non-magnetic MgF_2 was deposited at room temperature to protect the surface of the film from oxidation in atmosphere.

X-ray diffraction (XRD) and XRR measurements were performed using Cu K_α radiation from a Rigaku Smartlab thin film x-ray diffractometer. XRD measurements confirmed that all MBT films have the (0001) hexagonal crystal structure of Bi_2Te_3. The XRR data were analyzed quantitatively by performing non-linear least squares fits using an optical model with the GenX software package [47] to obtain layer thickness and interface roughness parameters. The magnetic moments of the films were measured using a Quantum Design MPMS XL superconducting quantum interference device (SQUID) magnetometer by applying an external magnetic field $\mu_0 H = 0.05$ T and measuring as a function of temperature from $T = 100$ K to $T = 4.5$ K.

X-ray fluorescence (XRF) was measured using using a XR-100CR Si detector

from Amptek using a monochromated 8.04 keV x-ray emmission from the Cu K_α radiation source used for XRD and XRR measurements. XRF measurements were performed on the two MBT films grown on MgF_2, the fluorescence spectra are shown in Fig. 4.1(a). These two films were chosen for this measurement because they represent samples at both the high and low ends of carrier density of samples in this study and because they have the same substrate, which this technique is sensitive to. Bi $M_{\alpha 1}$ and Mn $K_{\alpha 1}$ peaks were fit to a Gaussian line shape and the count ratios were compared to calculate a Mn percentage range between the two samples, which is in good agreement with the range calculated from Mn/Bi partial pressure during growth, ±1% Mn percentage, Fig. 4.1(b). XRF measurements also suggest that the differences in carrier density between samples may be due to variations in Mn percentage, where the Mn dopants are acting as electron acceptors. While variations in Mn concentration can change the magnetization of the films, the small variation here (±1%) is unlikely to be responsible for the large changes in magnetization (by a factor of two or more) observed in this study.

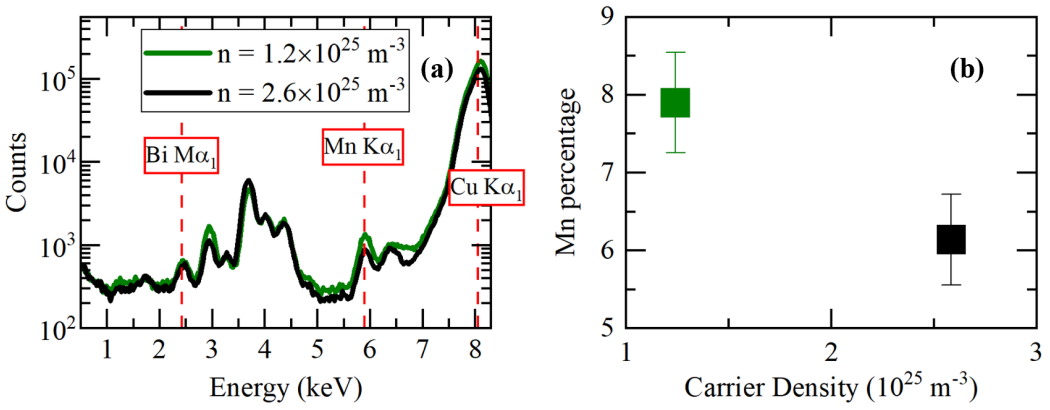

Figure 4.1: (a) XRF as a function of x-ray energy of two MBT samples grown on MgF_2. (b) calculated Mn percentage from relative intensity of Mn and Bi peaks. Unmarked peaks between 3 and 5 keV correspond to elements in a corning glass backing slide.

Seven different samples from five different growths, of which two were grown on Al_2O_3 (0001), two on MgF_2 (110), and three on NiF_2 (110), were made into Hall bars for transport measurements by first developing a Hall bar pattern using photolithography, followed by a wet etch in an aqua regia solution to remove the unwanted film. The main channel of the Hall bar between the sensing pads is 200μm wide by 500μm long. A microscope image of the etched Hall bar is shown in Fig. 4.2(a). The finished Hall bars were then adhered to chip carriers using commercially available conducting silver paint. Electrical contacts were made between the Hall bar pads and the chip carrier contacts using conducting silver paint and thin copper wire. The wired Hall bar is shown in Fig. 4.2(b).

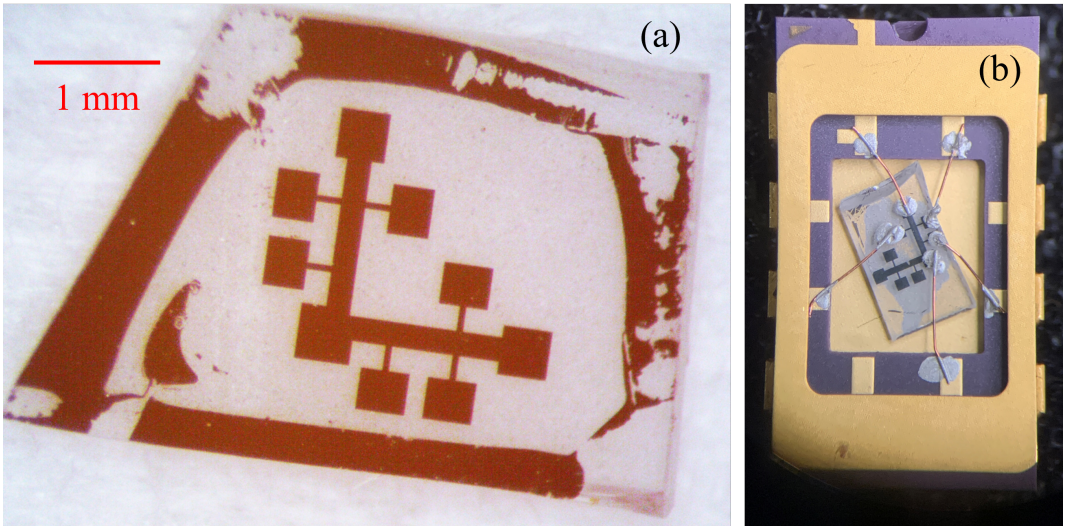

Figure 4.2: (a) Microscope image of MBT Hall bar before wiring into cryostat. (b) image of MBT Hall bar wired into cryostat chip carrier.

An MBT Hall bar with a dielectric top gate was also fabricated for this study. The thin film structure of the gated Hall bar device differs very slightly from that of the other MBT films studied, as it includes an undoped Bi_2Te_3 spacer layer, but the transport and magnetization properties are nearly identical to that of the previously described MBT films. A picture of the top-gate

MBT Hall bar and a cross section diagram of the film structure are shown in Fig 4.3(a) and (b) respectively. The dielectric Al_2O_3 top gate is sputter deposited onto the MBT Hall bar, and a photolithography lift off process is used to remove the dielectric from everywhere except for the conducting channel. To create a conducting contact to the dielectric top gate, 7 nm of Cr, then 30 nm of Au are deposited on the device via thermal evaporation and a second photolithography lift off process is performed to remove the unwanted metal film.

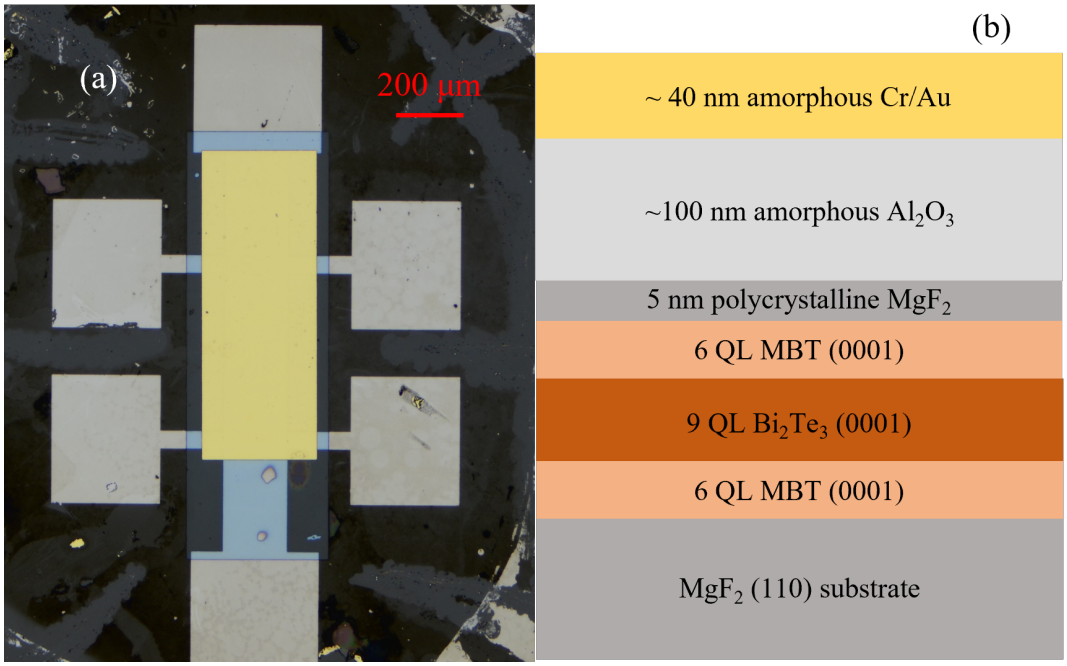

Figure 4.3: (a) Microscope image of MBT hall bar with Al_2O_3 top gate. (b) Cross section diagram of MBT top gate Hall bar device structure.

The Hall bar samples were loaded into a Janis 12TM-SVM Super VariTemp liquid helium cooled cryostat and measured in magnetic fields of up to 11 T and temperatures ranging from 300 K to 2 K. Electronic measurements were made using DC Keithley sources and meters, using a delta mode measurement method to take voltage measurements at each point with alternating pulses of ± 10 μA current.

Calculations of the anomalous Hall effect (AHE) and carrier density were done by performing a linear regression fit to the measured Hall resistance at $T = 2$ K in the magnetic field range between $\mu_0 H = \pm 3$ T and $\mu_0 H = \pm 1$ T, in order to probe only the AHE saturated regions. The intercept on the Hall voltage axis of this fit was used to determine the magnitude of the AHE while the slope, along with the film thickness, was used in the calculation of carrier density. The Hall mobility μ was calculated from the measured longitudinal resistivity ρ_{xx} of the device together with the carrier density n determined from the transverse resistivity excluding the AHE, $\rho_{xy} = \mu_0 H/ne$, using $\rho_{xx} = 1/ne\mu$, where e is the charge of the electron. The transition temperature of the MBT films was calculated by fitting the magnetic moment as a function of temperature, and the AHE as a function of temperature to the equation $m = a(1 - T/T_c)^{\beta} + b$.

4.3 Results and discussion

4.3.1 Crystallographic characterization

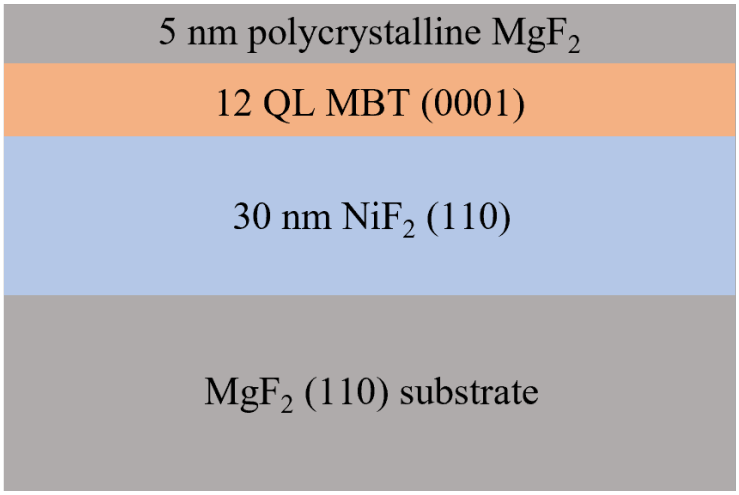

Figure 4.4: Diagram of MBT/NiF_2 thin film bilayer sample. Samples grown on MgF_2 (110) omit the NiF_2 (110) layer, while those grown on Al_2O_3 (0001) omit the NiF_2 (110) layer and have Al_2O_3 (0001) in place of MgF_2 (110).

The MBT thin films were grown on three types of substrates, hexagonal Al_2O_3 (0001), tetragonal MgF_2 (110), and tetragonal NiF_2 (110). A diagram of the sample structure is given in Fig. 4.4. XRD patterns of three representative MBT films grown on the three different substrates studied are shown in Fig. 4.5. The positions of the MBT diffraction peaks show no significant shifts relative to the expected (000ℓ) peaks of Bi_2Te_3, and no evidence of additional peaks that could be associated with other crystal structures or orientations. This result is consistent with a Bi_2Te_3 film with randomly distributed Mn dopants substituting at the Bi sites, rather than with the layered $MnBi_2Te_4$ family of crystals, which has a larger (0001) lattice parameter due to the addition of an ordered Mn layer [75]. RHEED patterns of the MBT films taken in-situ are shown in the insets of Fig. 4.5, and show bright, sharp streaks associated with smooth, single phase growth at the surface. It has been shown previously that attempting to incorporate too much Mn into the thin film crystal will degrade the structure significantly [81]. However, the result presented here is evidence that small amounts of Mn dopants, such as the $7 \pm 1\%$ doping of Mn used in this study, can be incorporated into the Bi_2Te_3 film without significant degradation of the crystal structure. Furthermore, MBT films grown on unconventional, tetragonal MgF_2 (110) and NiF_2 (110) films (which are themselves grown epitaxially on MgF_2 (110) substrates) are of very similar crystal quality to the film grown on Al_2O_3, as shown in Fig. 4.5. This conclusion is supported by rocking curve measurements of the MBT (00015) XRD peaks, where the calculated full-width-half-maximum values from Voigt line shape fits are $0.9° \pm 0.3°$, $1.5° \pm 0.5°$, & $1.8° \pm 0.7°$ for MBT on Al_2O_3, MgF_2 and NiF_2, respectively. We believe that the van der Waals bonding between adjacent layers of the MBT crystal makes it relatively insensitive to the lattice of the substrate it is grown on, so long as the substrate surface is sufficiently clean and smooth.

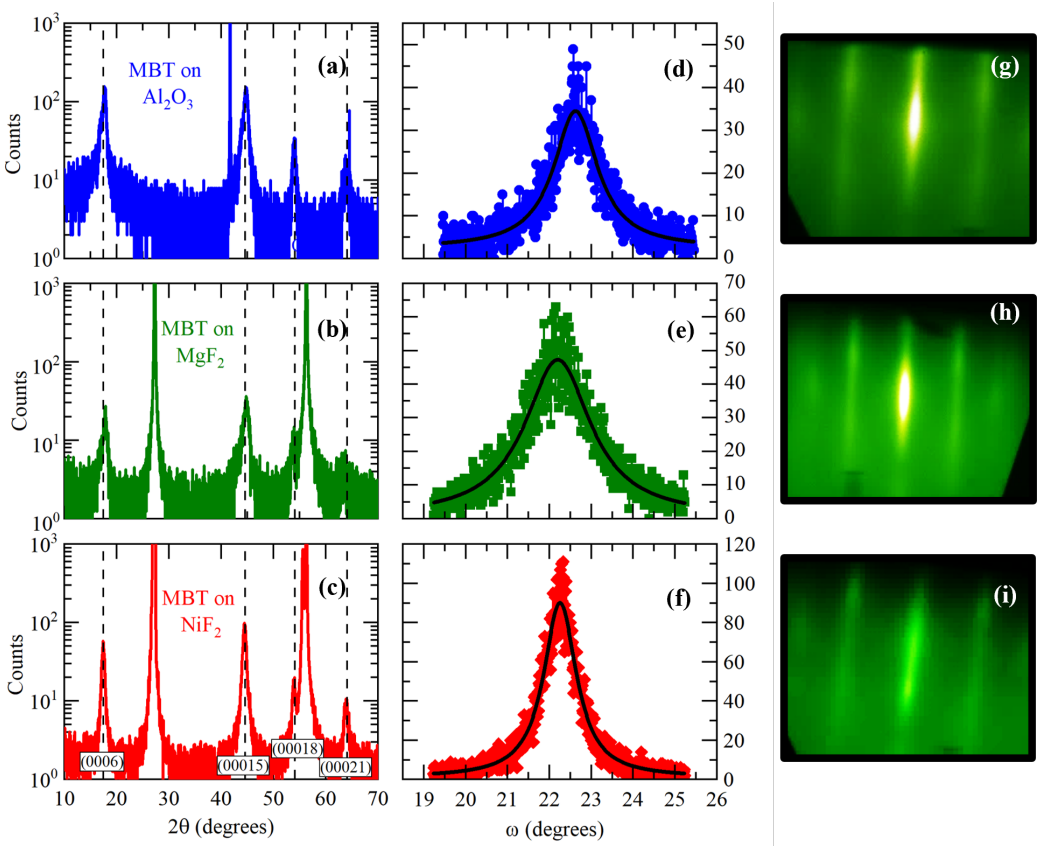

Figure 4.5: (a,b,c) XRD pattern of representative MBT films grown on (a) Al_2O_3 (0001), (b) MgF_2 (110), and (c) NiF_2 (110). Vertical black dashed lines indicate expected location of Bi_2Te_3 (000ℓ) diffraction peaks. Large, unmarked peaks correspond to the substrate diffraction peaks. (d,e,f) Rocking curve measurements and Voigt line shape fits to the (00015) diffraction peak of the representative films. (g,h,i) RHEED patterns of the corresponding MBT films obtained in situ after film growth but before MgF_2 capping layer deposition.

Raw XRR data and the fits to the data using GenX software are shown in Fig. 4.6 [47]. Table 4.1 shows the layer thickness and interface roughness values extracted from the fits. The MBT film thickness values are consistent with the expected thickness from calibration of molecular beam flux during growth, corresponding to approximately 12 QL of MBT. It is interesting to note that although the MgF_2 and NiF_2 substrates host MBT interfaces that

Table 4.1: Interface roughness (σ) and film thickness (t) parameters extracted from fits to XRR data shown Fig. 4.6 in units of nm. "sub" refers to the substrate, "cap" refers to the MgF_2 capping layer, "NA" = not applicable.

Substrate	σ_{sub}	t_{NiF_2}	σ_{NiF_2}	t_{MBT}	σ_{MBT}	t_{cap}	σ_{cap}
Al_2O_3 (0001)	0.7	NA	NA	12.7	0.1	4.8	2.3
MgF_2 (110)	1.5	NA	NA	13.8	0.2	4.5	1.7
MgF_2/NiF_2 (110)	1.2	22.7	1.8	13.3	0.4	4.9	1.6

are nearly twice as rough as the MBT interface with Al_2O_3, the final surface roughness of the MBT layer is not similarly as rough, likely due to Van der Waals bonding with the substrate, rather than epitaxial growth. These XRR data, in conjunction with XRD and RHEED data, offer compelling evidence that smooth, single phase MBT films can be grown on the tetragonal (110) surfaces of MgF_2 and NiF_2.

4.3.2 Magnetic Moment Measurements

While doping Bi_2Te_3 with a small amount of Mn does not significantly disrupt the crystal structure of the Bi_2Te_3 film, it does lead to the formation of a spontaneous ferromagnetic moment. Magnetization measurements as a function of temperature of the MBT films are presented in Fig. 4.7 with an applied field $\mu_0 H = 0.05$ T. Figure 4.7(a) shows data from a single run from all seven samples used in this study, with the magnetic moment measured perpendicular to the surface of the film, along the [0003] direction of the MBT film. A clear transition to a ferromagnetic state is observed in all MBT samples at an average temperature of $T_C = 15.5 \pm 1.0$ K, where the error is dominated by small variations in transition temperature between samples. We observed no clear correlation between the transition temperature and type of substrate used. Figure 4.7(b) shows the magnetic moment when the samples are rotated 90° to measure the moment in the plane of the film. In this direction, the ferromagnetic transition of the MBT film is more rounded and suppressed when

compared to the out-of-plane direction. This magnetic anisotropy and transition temperature of the MBT film is consistent with previous studies of Mn doped Bi_2Te_3, which has a magnetic easy axis along the [0003] crystallographic direction and a transition temperature around 15 K [78, 81]. It is important to note here that the magnetization values of the MBT/NiF_2 bilayers at $T = 4.5$ K are lower than the magnetization values of any of the MBT films on non-magnetic substrates. This behavior suggests that the NiF_2 may be acting to reduce the out-of-plane magnetization of the MBT films. More evidence of this effect will be presented below in measurements of the electronic transport of the films.

Measuring the magnetization along the in-plane direction reveals the magnetic behavior of the NiF_2 layer in the MBT/NiF_2 bilayers. While Al_2O_3 and MgF_2 are non magnetic, NiF_2 is an insulating antiferromagnet with a transition temperature of 73 K in bulk, and a Néel vector that orders in the *a*-*b* plane, preferentially along the [100] or [010] axes [10, 11]. NiF_2 also exhibits weak ferromagnetism due to a Dzyaloshinskii-Moriya interaction that causes a spontaneous canting of the antiferromagnetic moments in the *a*-*b* plane [10]. As a result, a ferromagnetic transition is evident in the MBT/NiF_2 bilayer, as shown by the magnetic response in Fig. 4.7(b). The NiF_2 transition temperature in these thin films is shifted from the expected 73 K bulk value to 78 K due to out-of-plane tensile strain in the NiF_2 thin film crystal resulting from the epitaxial growth on MgF_2 (110). The observed correlation between tensile strain in the [110] direction and transition temperature shown here is in agreement with previous studies of NiF_2 thin films grown by similar methods [65]. Magnetization measurements as a function of field at $T = 4.5$ K were also performed to measure the magnetic coercivity of the samples, as shown in Fig. 4.8. These measurements show magnetic hysteresis similar to that seen in

AHE measurements but are complicated by the fact that the SQUID magnetometer measurements are bulk sensitive, detecting the magnetization of the NiF_2 layer, which also has magnetic hysteresis in the [110] out-of-plane direction, in addition to the MBT film. This makes the magnetization of the MBT layer difficult to tell apart from the magnetization of the NiF_2 and substrate in this bulk sensitive measurement. The inability to distinguish between magnetic contributions from the MBT layer and the NiF_2 layer with this method demonstrates the value of electronic transport measurements in this situation, as transport measurements will only be sensitive to magnetic effects in the conducting MBT layer.

4.3.3 Electronic Transport Measurements

The MBT films were etched into Hall bars in order to perform electronic transport measurements. The normalized longitudinal resistance ΔR_{xx} of the MBT films and non-magnetic control films is shown in Fig. 4.9. Below 20 K, a large positive magnetoresistance develops in the MBT films as they transition from a paramagnetic state to a ferromagnetic state. This effect is in contrast to the control Bi_2Te_3 films grown on Al_2O_3 and NiF_2, which show only a small increase in magnetoresistance at low temperature due to enhance electron-electron interactions.

The development of ferromagnetic order in the MBT films is also observed in the Hall resistivity of the samples. Figure 4.10 shows the anomalous Hall resistivity as a function of temperature with an external magnetic field applied normal to the film surface of all seven MBT samples used in this study. From the onset of the AHE, the average transition temperature is calculated to be $T_C = 16.7 \pm 1.1$ K, with the error dominated by small variations of the transition temperature between samples. There is no evidence of an additional

AHE at $T = 78$ K, the transition temperature of the NiF_2, in the MBT/NiF_2 bilayers. The magnitude of the AHE is believed to be driven by carrier density, with lower carrier densities correlating with a larger AHE [77]. Discussion of the carrier density is presented below.

The Hall resistivity of each sample was measured at $T = 2$ K as a function of applied magnetic field and the results are shown in Fig. 4.11(a) for all seven MBT film samples and a control Bi_2Te_3 film. The carrier density of each sample was calculated from the ordinary Hall effect in regions where the AHE has saturated. The carriers in these films were found to be n-type, and the magnitudes of the carrier density for each sample are shown in Fig. 4.11(c,d). The variation in carrier density between samples is likely due to small differences in the exact film structure of each film, such as film thickness and the number of defects. Two measures of the magnetization strength of the films, the AHE resistivity and the coercive field, defined as the half width of the hysteresis of the AHE, are plotted as a function of the carrier density in Fig. 4.11(c) and (d) respectively. These figures demonstrate a correlation between the magnetic moment of the films and their carrier densities, where the magnetic moment increases as the carrier density decreases. It is not uncommon for metals to have ferromagnetic moments that are correlated with their carrier densities, but in cases of either RKKY interaction mediated long range order or Stoner criterion spin imbalance of conduction electrons, the magnetic moment would tend to decrease as the carrier density decreases, contrary to the behavior observed in these MBT films [84]. This apparent contradiction is resolved by considering the unique band structure of the TI film, where as the n-type carrier density decreases as the bulk conduction states are depleted as the Fermi level moves down in energy from the bulk conduction band into the bulk band gap. As the bulk conduction states are depleted, the conducting surface states in the

bulk band gap play a larger role in electronic conduction. The contradiction is therefore resolved by the presence of an RKKY interaction that takes place in the surface state conduction electrons, and not the bulk conduction electrons [76, 82, 83].

In the films studied here, the lowest carrier density was calculated to be 0.92×10^{25} m^{-3}, which suggests that the Fermi level of this film lies very close to the bottom of the bulk conduction band [81]. The relative proximity of the Fermi level to the bulk band gap in TI materials can be characterized by calculating the tangent of the Hall angle, defined as $\tan\theta_{\mathrm{H}} = \sigma_{xy}/\sigma_{xx}$. As the TI approaches the QAH state, the tangent of the Hall angle will increase until it eventually diverges, as the bulk longitudinal conductivity σ_{xx} approaches zero when the Landau levels are completely filled [23, 85]. The tangent of the Hall angle for the MBT samples studied here is given in Fig. 4.12, which shows how the tangent of the Hall angle increases with decreasing carrier density, indicating that the decrease in carrier density is being driven by the Fermi level moving from the bulk conduction band towards the bulk band gap. The values of $\tan\theta$ reported here are very small compared to films that exhibit the quantum Hall effect but are comparable to those observed in ferromagnetic TI films [85].

Hall effect measurements were performed on the sample shown in Fig 4.3(a) at $T = 2.5$ K. The results are shown in Fig 4.13. From the ordinary Hall effect shown in Fig 4.13(a), the carrier density is calculated for several values of the top gate voltage and is plotted in Fig 4.13(b). By applying a negative voltage to the top gate, the n-type carrier density is decreased, due to the fact that the Fermi level is being lowered from the bulk conduction band and towards the bulk band gap. The anomalous Hall resistance, the Hall resistance signal with the ordinary Hall effect subtracted, is shown in Fig 4.13(c), and the magnitude

of R_{AHE} as a function of the applied top gate voltage is shown in Fig 4.13(d). As a negative top gate voltage is applied, the magnitude of R_{AHE} increases, indicating that the magnetization of the MBT film is increasing. The result of this top gate measurement shows that the magnetization of the MBT film increases as the Fermi level approaches the bulk band gap, in agreement with the results of the previous experiment shown in Fig 4.11.

Figure 4.14 shows the magnetoresistance of the two lowest carrier density MBT films on non-magnetic substrates, and all three MBT/NiF_2 bilayers, at $T = 2$ K. The small peaks in resistivity at zero field are due to weak localization (WL), which increases the resistance of a 2D conducting state at zero applied external magnetic field. WL has been observed in ferromagnetic Cr-doped TI and is associated with the opening of the bulk band gap due to the spontaneous ferromagnetic moment breaking time reversal symmetry [32, 35, 73, 76, 86]. The WL seen here is relatively small, but it is entirely absent in the other samples with higher carrier density and in every MBT/NiF_2 bilayer, suggesting that the magnetic moment in these films is not sufficiently strong to open a large enough bulk band gap to induce WL.

The Hall mobility of the MBT samples was calculated from the longitudinal resistivity according to $\rho_{xx} = 1/ne\mu$. Plotting the AHE resistivity as a function of the mobility, as shown in Fig. 4.15 shows no clear correlation between the mobility and the AHE resistivity, indicating that the increased magnetic moment is not simply due to an increased mobility.

While ferromagnetic order survives in MBT films interfaced with antiferromagnetic NiF_2, the moment appears suppressed when compared to MBT films grown on non-magnetic substrates. In Fig. 4.11(d), the coercive field of the MBT/NiF_2 bilayers is significantly lower than the coercive field of MBT films on non-magnetic substrates. WL is similarly suppressed in all MBT/NiF_2 bi-

layers, as shown in Fig 4.14, suggesting an insufficient magnetic moment to open a bulk band gap. A similar effect is seen in the magnetization measurements shown in Fig. 4.7(a), where the magnetization at $T = 4.5$ K is lower in the MBT/NiF_2 bilayes than in the MBT films on Al_2O_3 or MgF_2. A possible mechanism responsible for the suppression of the ferromagnetic moment in MBT/NiF_2 bilayers is that the NiF_2 layer pins an interfacial layer of spins in the MBT to an in-plane orientation. It is known that ferromagnet/NiF_2 bilayers can exhibit exchange bias by a similar effect [65], and the MBT films studied here have a sufficiently weak magnetic anisotropy such that they can be, at least partially, rotated to an in plane orientation, as shown in Fig. 4.7(b). Another possible explanation is that the local NiF_2 moments at the interface are introducing additional magnetic scattering effects in the MBT surface states, which would explain the lack of localization effects in the magnetoresistance measurements as strong magnetic scattering is associated with the unitary case in the HLN model [32].

4.3.4 Summary

To summarize the findings of this chapter, it is shown how a spontaneous ferromagnetic moment below $T = 16$ K can be induced in $Mn_{0.14}Bi_{1.86}Te_3$ thin films by doping Bi_2Te_3 with Mn atoms that randomly substitute into the Bi sites. RHEED and XRD measurements are evidence of successful MBT thin film growths on tetragonal crystal substrates, MgF_2 (110) and NiF_2 (110). Electronic transport and magnetic moment measurements show how the magnetization of the MBT films is enhanced as the Fermi level moves from the bulk conduction band towards the bulk band gap. When taken alongside previous works [82, 83], this study provides evidence that the electronic surface states of the TI play an important role in mediating ferromagnetic order in this material.

This mechanism of magnetic ordering appears to be unique to the TI system, since the magnetization increases with decreasing volume carrier density, in contrast to the expected behavior in ordinary metals of the magnetization decreasing with reduced carrier density. MBT/NiF_2 bilayers show evidence of a suppressed ferromagnetic moment along the [0003] direction, evidence of a proximity effect at the ferromagnetic MBT/antiferromagnetic NiF_2 interface. The magnetic behavior of these systems and their interactions represent necessary advancements in the understanding of these systems for potential device applications and the study of novel quantum phenomena.

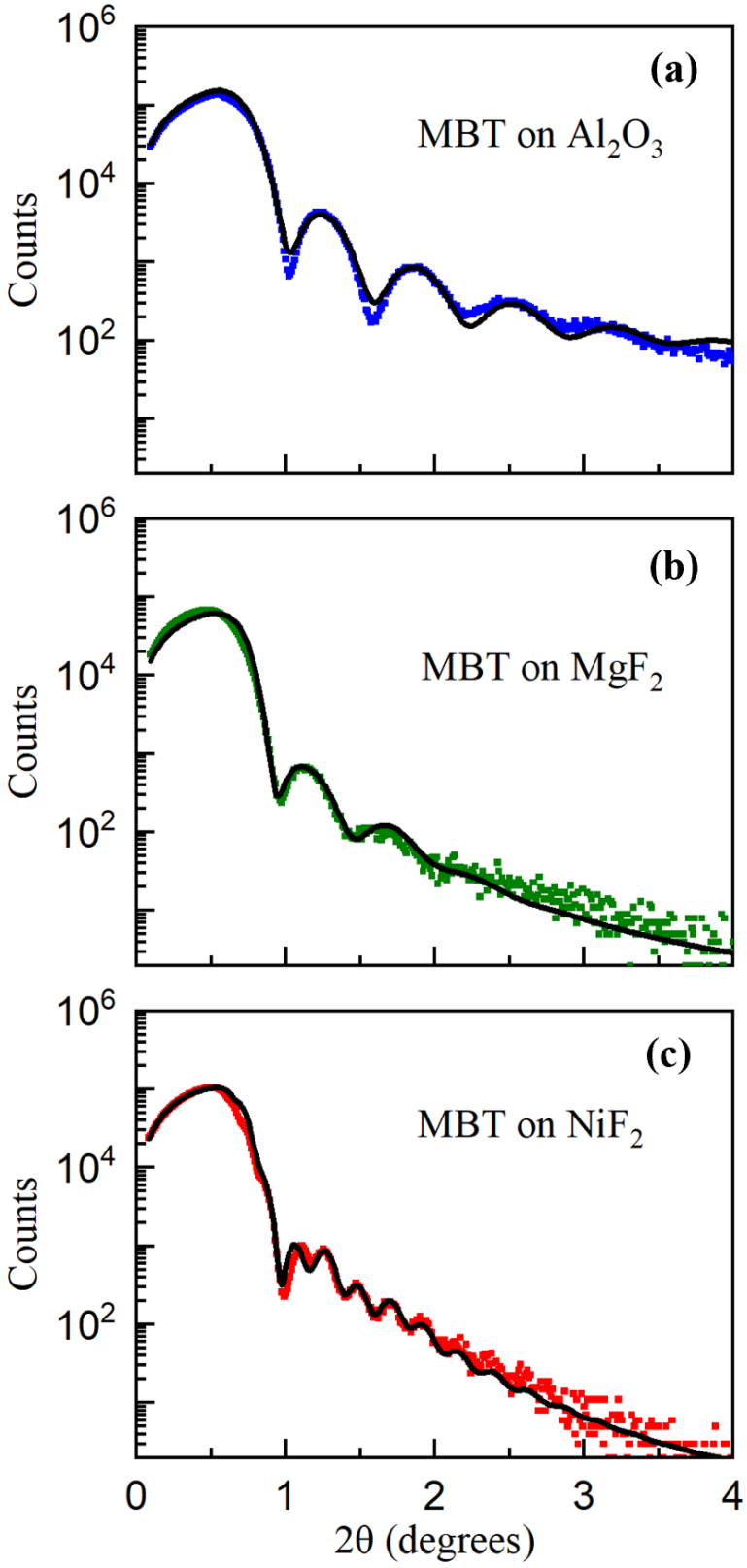

Figure 4.6: XRR pattern of MBT films grown on (a) Al_2O_3 (0001), (b) MgF_2 (110), and (c) MgF_2/NiF_2 (110). Solid black curves indicate fits to the measured data.

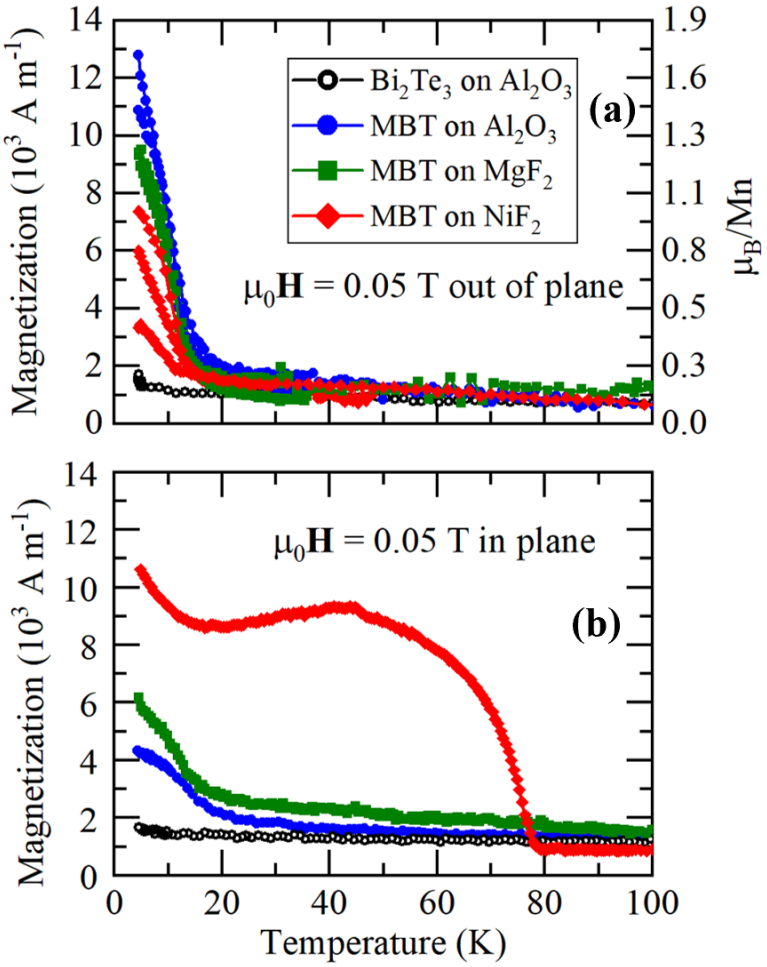

Figure 4.7: Field cooled magnetization as a function of temperature, measured along the same direction as the applied field, of a single run from several different MBT films grown on Al_2O_3 (shown in blue), MgF_2 (shown in green), and NiF_2 (shown in red), and undoped Bi_2Te_3 grown on Al_2O_3 (shown in black). (a) Magnetization measured measured perpendicular to the film surface, along the [0003] axis of the MBT and Al_2O_3 crystals, and the [110] direction of the MgF_2 and NiF_2 crystals, with $\mu_0 H = 0.05$ T. (b) Magnetization as a function of temperature of three representative MBT samples measured parallel to the film plane, along the $[1\bar{1}0]$ direction of the MgF_2 and NiF_2 crystals, with $\mu_0 H = 0.05$ T.

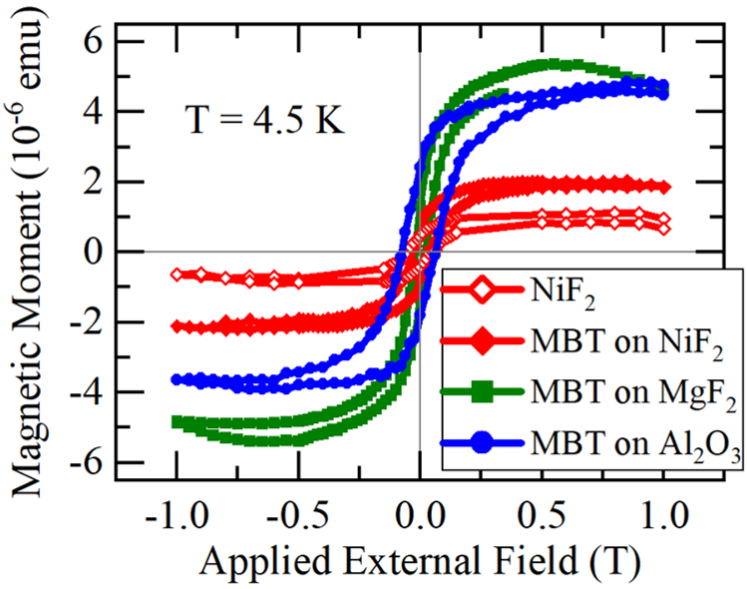

Figure 4.8: Magnetic moment as a function of applied field at $T = 4.5$ K, measured out-of-plane of representative samples.

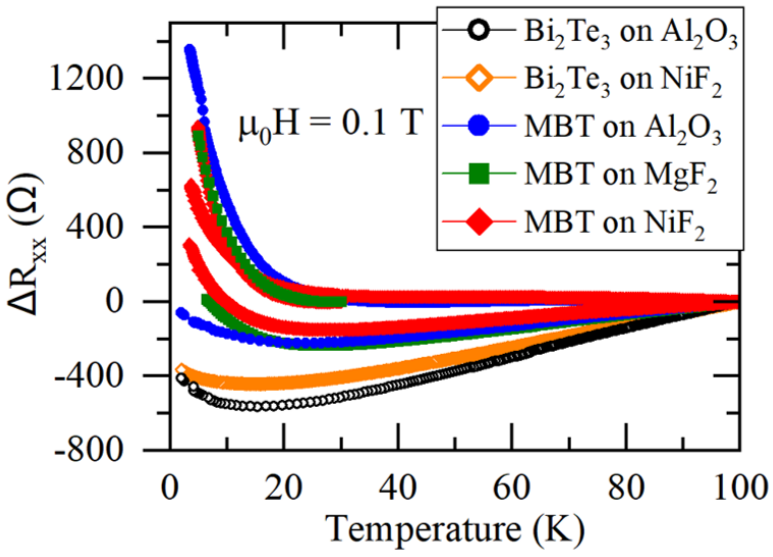

Figure 4.9: Normalized longitudinal resistance of MBT films and control films as a function of temperature in a small applied field μ_0H = 0.1 T.

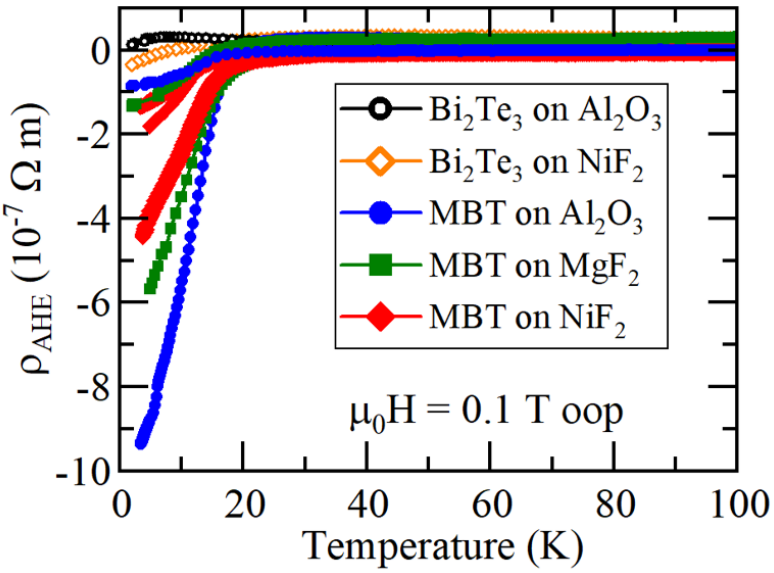

Figure 4.10: Anomalous Hall resistivity as a function of temperature with $\mu_0 H = 0.1$ T, applied normal to the film surface, from a single run of all seven MBT films and two Bi_2Te_3 control films.

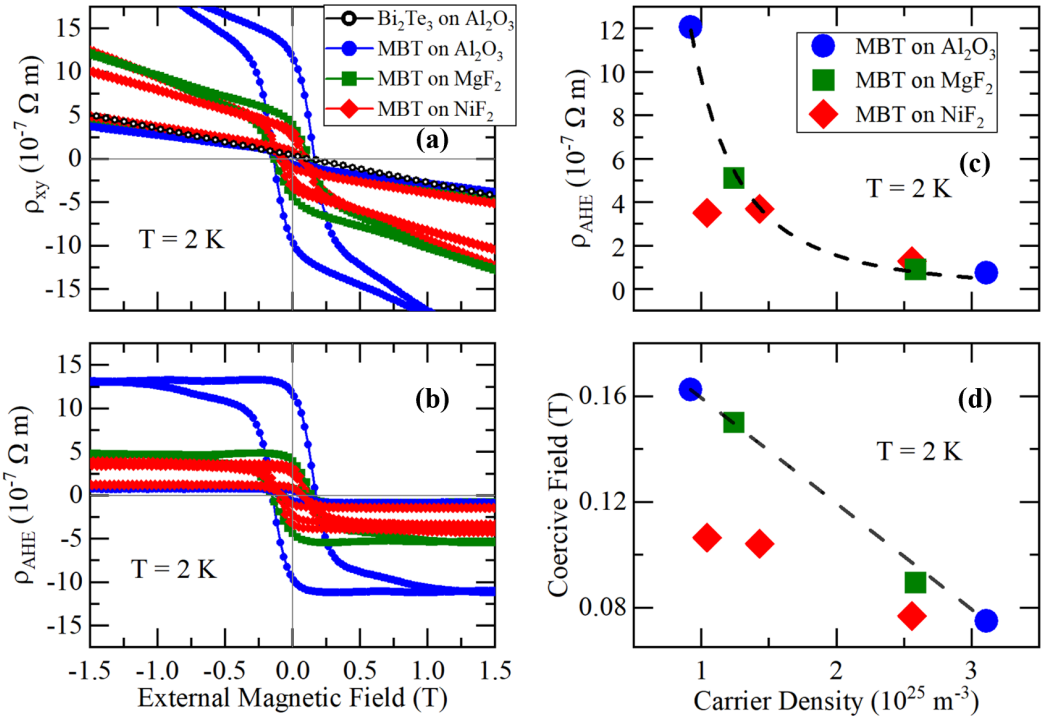

Figure 4.11: (a) Hall resistivity as a function of applied field at $T = 2$ K, from a single run of all seven MBT films and a Bi_2Te_3 control film. Undoped Bi_2Te_3 film, shown in black, MBT grown on Al_2O_3, shown in blue, MBT grown on MgF_2, shown in green, and MBT grown on NiF_2, shown in red. (b) Anomalous Hall resistivity after subtraction of the ordinary Hall effect linear background. (c) AHE resistivity as a function of carrier density of all seven MBT films used in this study. (d) Coercive field values calculated from anomalous Hall resistivity measurements at $T = 2$ K of all seven MBT films.

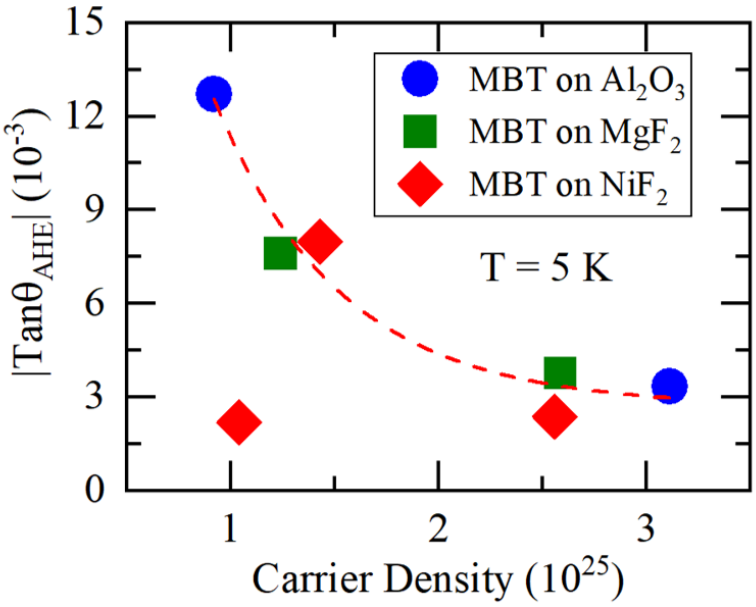

Figure 4.12: The tangent of the Hall angle as a function of carrier density. The red dashed line is a guide to the eye.

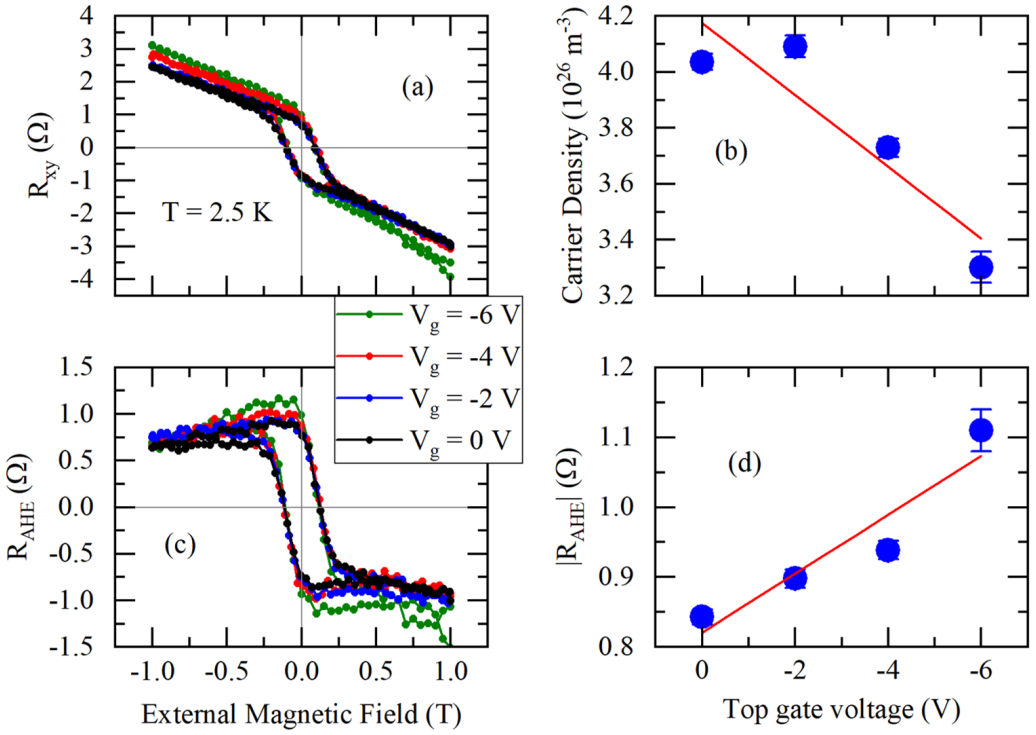

Figure 4.13: (a) Hall resistance at $T = 2.5$ K at several values of the applied top gate voltage. (b) Carrier density calculated from the ordinary Hall effect as a function of the top gate voltage. (c) Anomalous Hall effect resistance R_{AHE} at several values of the applied top gate voltage. (d) Magnitude of R_{AHE} as a function of the top gate voltage.

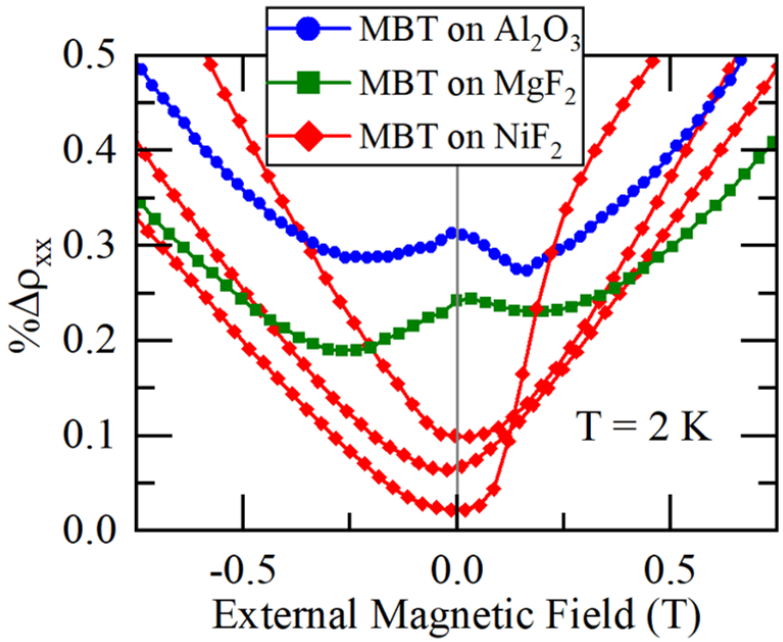

Figure 4.14: Longitudinal resistivity as a function of applied magnetic field of the lowest carrier density MBT films on Al_2O_3 and MgF_2, and all three MBT/NiF_2 bilayers.

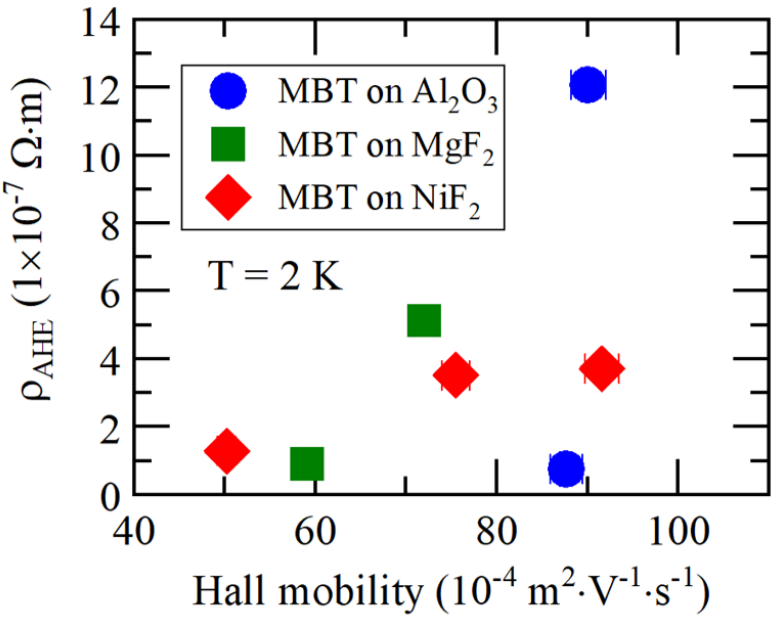

Figure 4.15: Anomalous Hall resistivity as a function of the carrier density at $T = 2$ K for the MBT films used in this study.

Chapter 5

Band structure engineering in $(Bi,Sb)_2Te_3$ - MnF_2 bilayers

5.1 Introduction

The interface between antiferromagnetic insulators and metals with strong SOC has yielded interesting spin interaction phenomena in recent years. In particular, studies MnF_2-Pt thin films have demonstrated the spin Seebeck effect, where a temperature gradient in the MnF_2 layer induces spin waves analogous to the electric voltage generated in the ordinary Seebeck effect. At the interface with Pt the spin waves inject some spin current into the Pt layer where it induces an electric voltage via the ISHE [13]. MnF_2-Pt bilayers have also exhibited spin pumping from magnon modes in the MnF_2 excited by subterahertz microwaves which then induce an electric voltage in the Pt overlayer [12].

These discoveries demonstrate that there is interesting and potentially useful physics occurring at the interfaces of these materials and has motivated work to enhance these spin interactions with novel materials. Topological insula-

tors are promising materials for these types of spin interaction devices due to their exceptional spin currents that result from spin-momentum locking in the surface states [87, 88]. A persistent problem with common 3D TI materials is the tendency of the Fermi level to shift out of the bulk band gap due to defects in the crystal. This has the undesirable consequence of creating a bulk conduction channel that effectively shunts the conducting surface states where the most useful phenomena exist.

In this chapter, it is demonstrated how co-doping Bi and Sb into the $(Bi,Sb)_2Te_3$ (BST) thin film crystal can be used to tune the Fermi level into the bulk band gap of the system. These $(Bi,Sb)_2Te_3$ films are then grown on MnF_2 thin films with the aid of a graded $(MnNi)F_2$ buffer layer and fabricated into bi-directional Hall bar devices to measure transport parallel and perpendicular to the easy axis of the MnF_2 film. Magnetization measurements of the sample stack show evidence of ordered magnetic moments corresponding to the $(MnNi)F_2$ graded layer and the MnF_2 thin film. Magnetoconductivity measurements of the BST film are performed with the external magnetic field applied normal and parallel to the plane of the film and fit to HLN, Al'tshuler-Aronov, and Dirac state models, from which phase coherence length, Fermi velocity, the HLN constant α, and transport dimensionality are calculated. From these measurements and fits, it is demonstrated how the co-doped $(Bi,Sb)_2Te_3$ films exhibit 2D transport and enhanced magnetic scattering when interfaced with MnF_2, indicating the viability of this system to exhibit further spin interaction phenomena. These results demonstrate the viability of next-generation experimental device architectures that utilize topological insulator overlayers on an insulating antiferromagnetic layer could exhibit coupling effects significantly larger than those observed in Pt overlayer devices.

5.2 Methods

The BST-MnF_2 thin film bilayer samples used in this study were grown via MBE in the Lederman lab. A 30 nm MnF_2 film was first grown with the $(MnNi)F_2$ graded buffer layer method as described in section 3.2. The MnF_2 film was then moved to a separate chamber for growth of the BST layer without breaking vacuum. A quartz crystal monitor was used to calibrate the flux ratio from 99.999% pure Bi, Sb, and Te thermal evaporation sources. The first 3 QL of BST were deposited at a lower growth temperature of 200° C, after which the sample was heated to 275° C and 6 more QL were deposited, for a final thickness of 9 QL of BST. The film was then allowed to cool back to ambient temperature before 3 nm of amorphous MgF_2 was deposited on the surface to protect the BST from oxidation in atmosphere.

XRD measurements of the films were performed using a Rigaku SmartLab X-Ray Diffractometer. A Quantum Design MPMS XL SQUID Magnetometer was used to perform magnetic moment measurements of the bilayer films and determine the direction of the *c*-axis of the MnF_2 film, in the same manner as described in Section 3.2.

Perpendicular magnetoconductivity measurements of the films were performed by etching the films into Hall bars and measuring in a liquid helium cooled superconducting cryostat as described in Section 4.2. Parallel magnetoconductivity measurements of the same films were performed by mounting the Hall bar devices onto a small plastic wedge via silver paint, which was then mounted onto the chip carrier, also by silver paint. The Hall bar was then wired into the chip carrier in the same manner as in the perpendicular magnetoconductivity measurements.

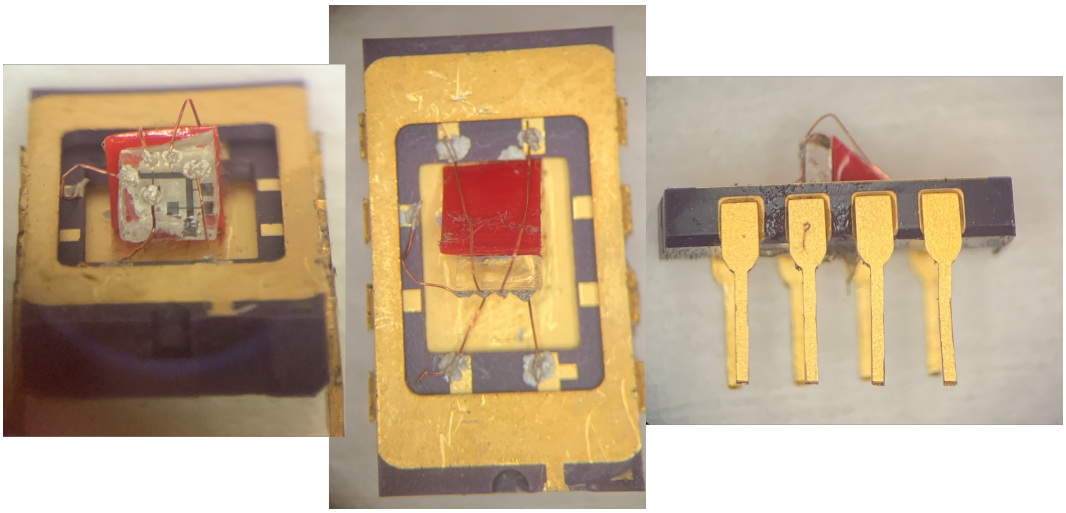

Figure 5.1: Images of BST Hall bar in parallel magnetoconductivity orientation

5.3 Results and discussion

5.3.1 Crystallography and magnetization

XRD measurements of the BST-MnF_2 thin film sample shows that single phase BST {003} can be grown on MnF_2 thin films via MBE. Figure 5.2 shows the XRD pattern of the sample stack, with BST and MnF_2 diffraction peaks labeled in red and green, respectively.

Magnetization measurements of the BST-MnF_2 thin film sample reveals intriguing magnetic behavior of the MnF_2-$(MnNi)F_2$ graded layer stack. Figure 5.3(a) shows the in plane field-cooled (FC) magnetization measurements of the BST-MnF_2 thin film sample, where the sample is cooled from $T = 100$ K to $T = 4.5$ K with an applied field of $\mu_0 H = 0.1$ T. The magnetization is measured along the same direction of the applied field, and the FC measurement is repeated twice, once with the field and magnetization measured along the in plane c-axis of the MnF_2 and once in plane perpendicular to the c-axis, corresponding to the $[1\bar{1}0]$ crystallographic direction. Figure 5.3(b) shows the thermal remnant magnetization (TRM) of same sample and two in plane di-

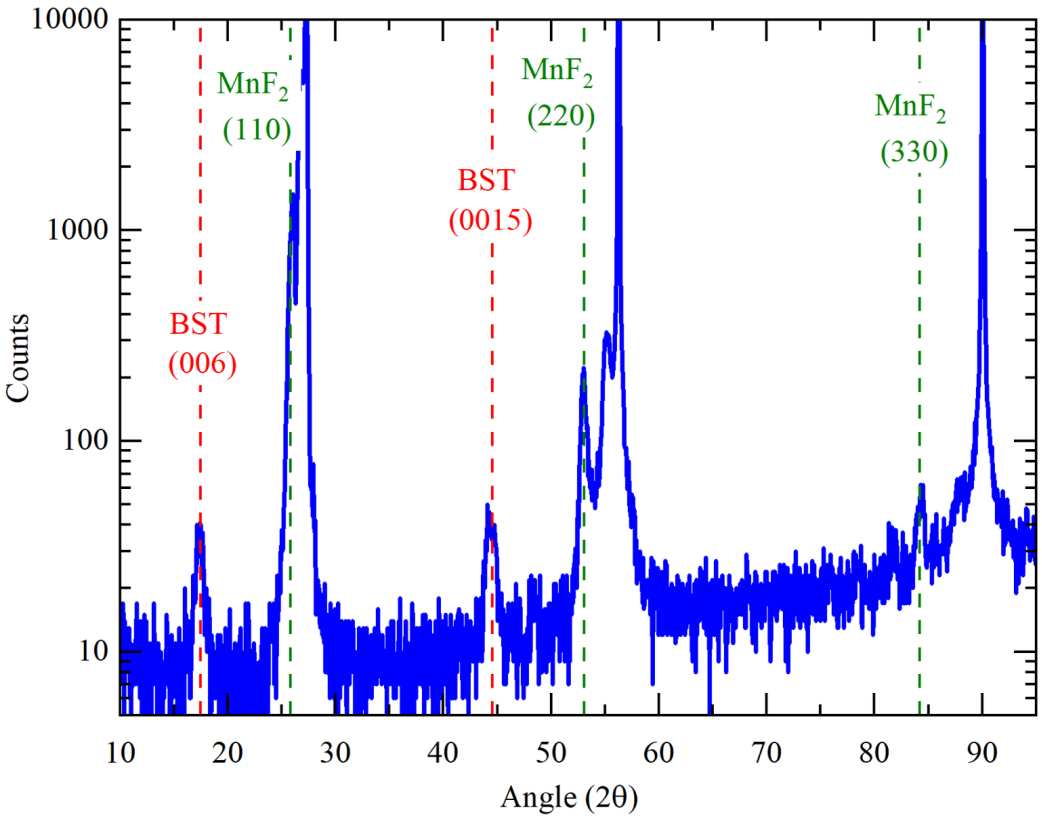

Figure 5.2: XRD pattern of 9 QL of BST (003) grown on 50 nm of MnF_2 (110) with the aid of a 20 nm $(MnNi)F_2$ graded buffer layer on a MgF_2 (110) substrate. The expected position of the diffraction peaks of BST {003} and MnF_2 {110} are denoted by the dashed red and green lines, respectively.

rections as in Fig. 5.3(a). The TRM measurements are performed immediately after the FC measurements, by setting the applied field to zero and measuring the magnetization as the sample is warmed from $T = 4.5$ K to $T = 100$ K.

The magnetization curves presented in Fig. 5.3 show evidence of two independent magnetic orderings. When the magnetization is measured along the c-axis of the MnF_2-$(MnNi)F_2$-MgF_2 system, there is a magnetic phase transition at $T = 67.3 \pm 0.7$ K, determined from the TRM curve in Fig. 5.3(b) fitted to Eq. 2.8. This transition corresponds to the bulk transition temperature of MnF_2, which is expected when measuring along the c-axis as is done here.

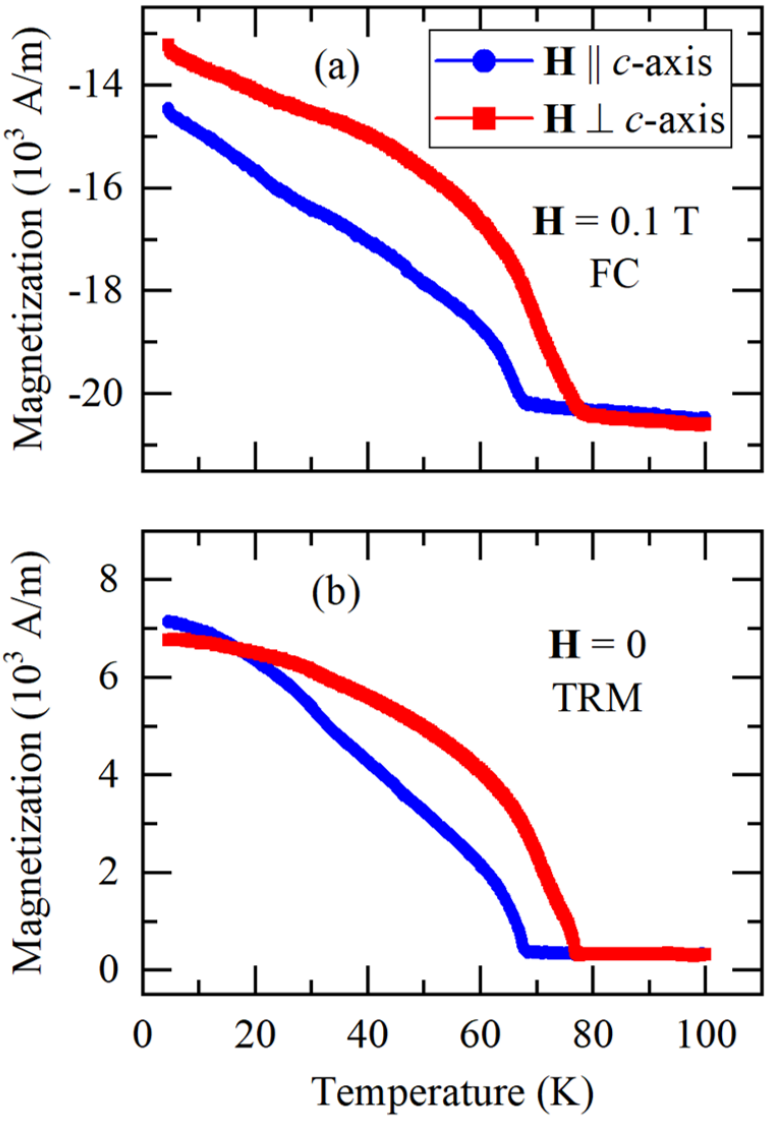

Figure 5.3: (a) field-cooled (FC) magnetization of BST-MnF_2 thin film sample with the applied field and magnetization measured in the plane of the film. The blue curve represents the applied field and magnetization along the c-axis of the MnF_2 thin film crystal, while the red curve represents the applied field and magnetization perpendicular to the c-axis, along the $[1\bar{1}0]$ direction. (b) Thermal remnant magnetization (TRM) of the BST-MnF_2 thin film sample measured along the same directions as in (a).

When the magnetization is measured in plane perpendicular to the c-axis, there is another magnetic phase transition at $T = 76.5 \pm 0.4$ K. The magnetization direction and transition temperature of this magnetic phase agrees with the solid solution $Mn_xNi_{1-x}F_2$ thin film alloys presented in Section 3.3.2 and therefore can be attributed to the $(MnNi)F_2$ graded buffer layer. The fact that these two magnetic phases order in different directions and at different temperatures suggests that they are magnetically de-coupled from each other. The higher magnetic transition temperature of the graded buffer layer is not influencing the magnetic phase transition of the MnF_2 layer, which has the expected properties and behaviors of a MnF_2 film free from crystal strain.

Figure 5.4 shows the in plane magnetization of the BST-MnF_2 thin film sample parallel and perpendicular to the c-axis as a function of the applied magnetic field at $T = 2$ K, with a linear paramagnetic background subtracted. When the applied field and magnetization are measured along the c-axis, the magnetic hysteresis loop shows evidence of two distinct magnetic sublattices. One soft sublattice flips its magnetization as the applied field goes through zero, while a second, hard sublattice does not flip until the field is roughly ± 2.8 T. When the applied field and magnetization are measured in plane perpendicular to the c-axis, there is again a soft sublattice that flips near zero field, and a second, hard sublattice that flips near ± 1.2 T.

5.3.2 Electronic properties

There are two primary ways of bringing the Fermi level into the bulk band gap, either by applying a gate voltage or by chemical doping. The method used here involves a co-doped alloy of p-type (Fermi level in the valence band) Sb_2Te_3 and n-type (Fermi level in the conduction band) Bi_2Te_3 [89]. The location of the Fermi level in the electronic band structure can be deduced by the carrier

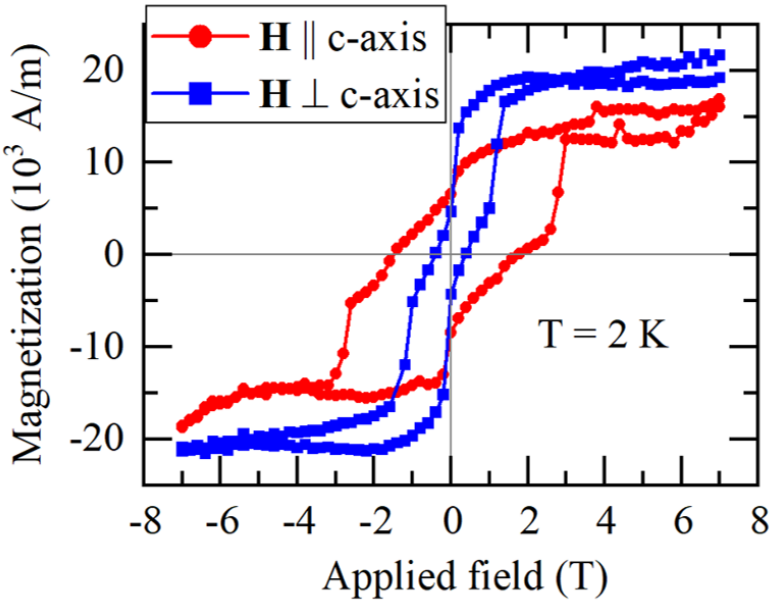

Figure 5.4: Magnetization of the BST-MnF_2 thin film bilayer measured along two perpendicular in plane directions, parallel and perpendicular to the c-axis of the MnF_2 layer.

density and type of carrier, as the carrier density will decrease as the Fermi level moves towards the bulk band gap until the carrier type flips when the Fermi level moves entirely through the gap and into the opposite bulk band. The carrier type and density is calculated from the ordinary Hall effect. The Hall resistance as a function of field for the TI films used in this project is shown in Fig 5.5(a).

The carrier density of these films is calculated from the Hall resistance according to

$$n = \frac{\mu_0 H}{R_{xy} t e}, \tag{5.1}$$

where μ_0 is the vacuum magnetic permeability, H is the applied magnetic field, t is the film thickness, and e is the charge of an electron. The calculated carrier densities for each TI film at $T = 2$ K are given in Table 5.1.

As shown in Fig 5.5(a) and Table 5.1, pure Bi_2Te_3 films have n-type carriers

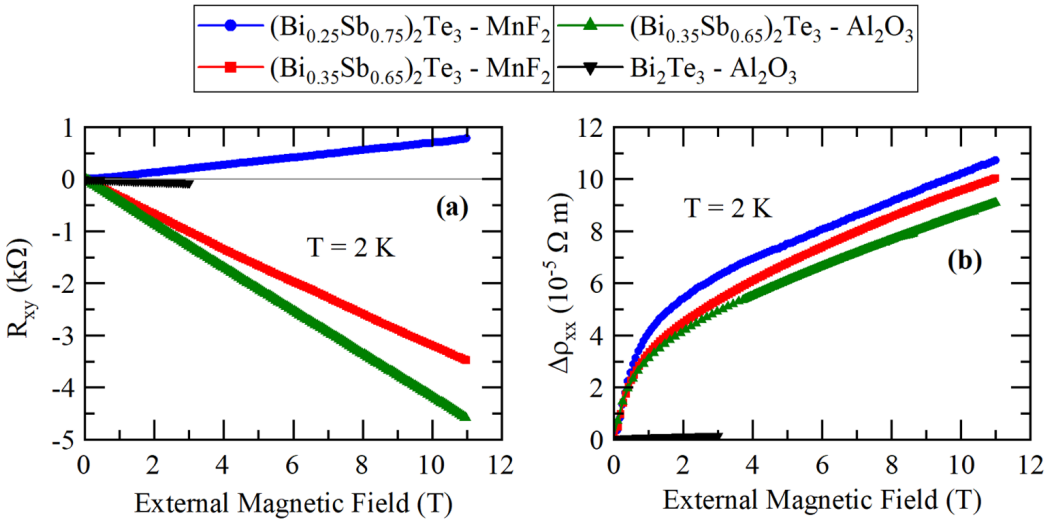

Figure 5.5: (a) Hall resistance as a function of external magnetic field applied normal to the film surface at $T = 2$ K for several TI films. (b) the change in longitudinal resistivity relative to $\rho_{xx}(0)$ for the same time films at $T = 2$ K.

Sample	n (10^{18} cm^{-3})
$(Bi_{0.25}Sb_{0.75})_2Te_3$ - MnF_2	9.79 ± 0.07
$(Bi_{0.35}Sb_{0.65})_2Te_3$ - MnF_2	-2.05 ± 0.01
$(Bi_{0.35}Sb_{0.65})_2Te_3$ - Al_2O_3	-1.62 ± 0.01
Bi_2Te_3 - Al_2O_3	-19.2 ± 0.3

Table 5.1: Carrier density of TI films calculated at $T = 2$ K. Positive values indicate hole carriers, while negative values indicate electron carriers.

due to the Fermi level lying somewhere in the bulk conduction band [90]. By changing the stoichiometry from pure Bi_2Te_3 to $(Bi_{0.35}Sb_{0.65})_2Te_3$, the films are still n-type but have about 10 times fewer carriers, indicating that the Fermi level is very close to the bulk band gap [81, 90]. Increasing the Sb amount even further, to $(Bi_{0.25}Sb_{0.75})_2Te_3$, causes the dominant carrier to flip from n-type to p-type, indicating that the Fermi level has moved through the bulk band gap and now lies somewhere in the bulk valence band [91]. By chemically doping $(Bi,Sb)_2Te_3$ films grown on antiferromagnetic MnF_2 thin films and moving the Fermi level into the bulk band gap, the electric conduction through the TI surface states is enhanced and interactions at the interface between these two

materials should become more pronounced.

Longitudinal resistance measurements of the BST samples as a function of the sample temperature are shown in Fig. 5.6. All samples measured show an increase in resistance below $T = 20$ K associated with enhance electron-electron scattering as discussed in Section 1.2.4, but the BST films grown on antiferromagnetic MnF_2 thin films (Fig. 5.6(a,b)) show greatly enhanced resistance at low temperature when compared to the TI films grown on non-magnetic Al_2O_3 substrates (Fig. 5.6(c,d)). This enhanced longitudinal resistance at low temperature could be due to magnetoelectric proximity effects at the interface that act to reduce the phase coherence length and suppress WAL. Further discussion of these effects will be presented below.

Measurements of the magnetoconductivity at low temperature and near zero applied magnetic field are used to measure the quantum corrections to the conductivity. Theoretical work by Al'tshuler and Aronov predicts the quantum corrections to the magnetoconductivity in the parallel orientation, with the external magnetic field applied parallel to the plane of the film [36]. The parallel magnetoconductivity of a $(Bi_{0.35}Sb_{0.65})_2Te_3$ - MnF_2 thin film Hall bar is shown in Fig 5.7. Figure 5.7(a) shows the parallel magnetoconductivity at small external magnetic fields and at various sample temperatures. By fitting the magnetoconductivity curves to Eq. 1.32, the phase coherence lengths l_ϕ at each temperature can be calculated and are presented in Fig 5.7(b).

It has been shown theoretically that the coherence length of electrons scattered by impurities in a 1D or 2D system have the following relation [39]

$$l_\phi = (D\tau_\phi)^{1/2} \propto T^{-d/4}, \tag{5.2}$$

where D is the diffusion coefficient and d is the dimensionality of the charge

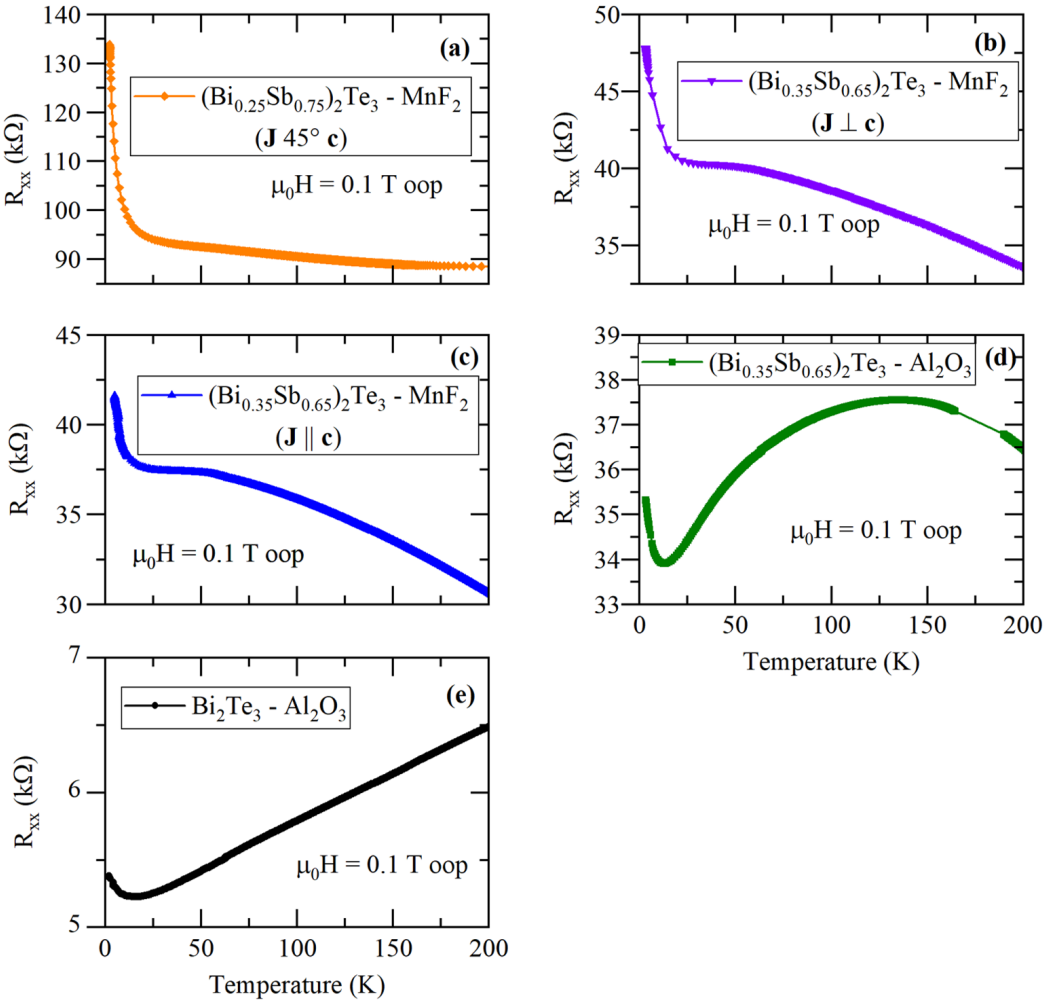

Figure 5.6: Longitudinal resistance R_{xx} as a function of temperature for several BST films and a Bi_2Te_3 film with an external magnetic field applied out-of-plane. The BST-MnF_2 sample shown in (a) has the current flowing through the BST film at an angle of 45° relative to the *c*-axis of the MnF_2 layer, while the sample shown in (b) has the current flowing perpendicular to the *c*-axis of the MnF_2 layer and the sample shown in (c) has the current flowing parallel to the *c*-axis.

transport. The power law fits to the temperature dependent phase coherence length are shown in Fig 5.7(b) and (d), and show good agreement with the 2D case ($d = 2$), indicating that the electronic transport is primarily through the

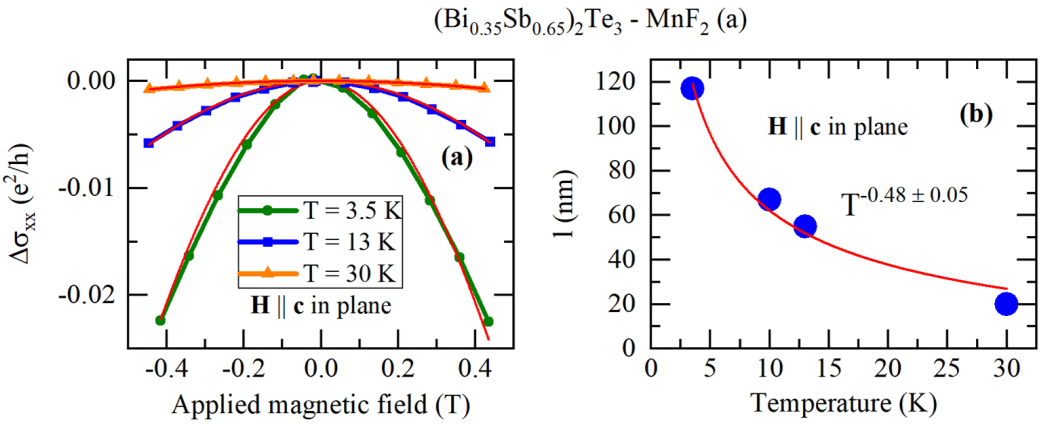

Figure 5.7: (a) Parallel magnetoconductivity of a $(Bi_{0.35}Sb_{0.65})_2Te_3$ - MnF_2 thin film Hall bar with the H-field applied in the plane of the film along the c-axis of the MnF_2. (b) phase coherence length l_ϕ at several temperatures fit to a power law.

2D surface states, in agreement with carrier density measurements presented in Fig. 5.5 that indicated the Fermi level is in close proximity to the bulk band gap.

The elastic scattering time τ_e, the average time between electron scattering events that do not cause the phase to decohere, is determined from the longitudinal conductivity measured as a function of the sample temperature, according to the expression given in Eq. 1.37. At large applied magnetic fields, where the cutoff for a large perpendicular field is given by Eq. 1.35, the localization effects are suppressed and electron-electron scattering dominates the low temperature conductivity. Measurements of the longitudinal conductivity in a large perpendicular magnetic field ($\mu_0 H = 1$ T) for several $(Bi_{0.35}Sb_{0.65})_2Te_3$ thin film samples are shown in Fig. 5.8.

By fitting the temperature dependent conductivity shown in Fig. 5.8 to Eq. 1.37, the averaged screened Coulomb interaction F and elastic scattering time τ_e of the electrons is calculated.

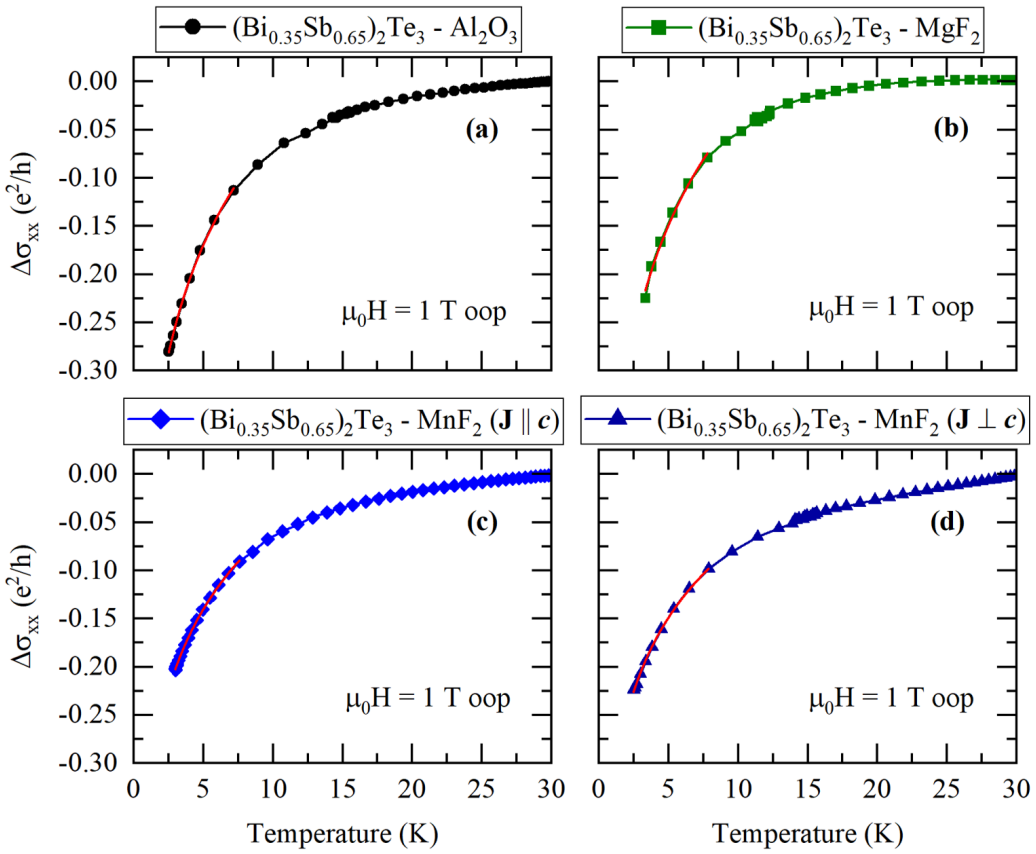

Figure 5.8: Perpendicular magnetoconductivity as a function of temperature for $(Bi_{0.35}Sb_{0.65})_2Te_3$ thin films grown on (a) Al_2O_3, (b) MgF_2, and (c,d) MnF_2, with an external magnetic field $\mu_0 H = 1$ T applied perpendicular to the film surface. The conductivity is measured relative to the conductivity at $T = 30$ K, where $\Delta\sigma_{xx}(T) = \sigma_{xx}(T) - \sigma_{xx}(30\text{K})$. The red curves are fits to Eq. 1.37.

Sample	F	τ_e (ps)
$(Bi_{0.35}Sb_{0.65})_2Te_3$ - Al_2O_3	0.49 ± 0.01	0.54 ± 0.01
$(Bi_{0.35}Sb_{0.65})_2Te_3$ - MgF_2	0.47 ± 0.02	0.63 ± 0.03
$(Bi_{0.35}Sb_{0.65})_2Te_3$ - MnF_2 ($\mathbf{J} \perp \mathbf{c}$)	0.65 ± 0.01	0.40 ± 0.01
$(Bi_{0.35}Sb_{0.65})_2Te_3$ - MnF_2 ($\mathbf{J} \parallel \mathbf{c}$)	0.62 ± 0.01	0.48 ± 0.01

Table 5.2: Values derived from Al'shuler-Aronov-Lee magnetoconductivity (Eq. 1.37) fits to the data shown in Fig. 5.8

Further characterization of the electronic properties of the TI layer are performed by measuring the perpendicular magnetoconductivity at low temper-

ature and small applied magnetic fields. In this regime, localization effects generated by 2D transport become large [32, 34]. The Hikami-Larkin-Nagaoka (HLN) model, shown in Eq. 1.25, is commonly used to describe the quantum corrections to the magnetoconductivity generated by localization behavior of a quasi-2D system. The HLN model is useful for determining the phase coherence length l_ϕ and the dimensionless parameter α, which describes the properties of the electronic system and the type of localization behavior that will be observed. In the orthogonal case ($\alpha = 1$), there is no SOC nor magnetic scattering and weak localization is observed. In the unitary case ($\alpha = 0$), there strong magnetic scattering that suppresses all localization effects. Finally, in the symplectic case ($\alpha = -1/2$), there is strong SOC and no magnetic scattering and weak anti-localization (WAL) is observed.

As discussed in section 1.2.3, the HLN model is useful for describing localization effects in TI materials, but it fails to capture the true 2D electronic transport in the surface states and their Dirac (linear dispersion relation) nature. Work by Adroguer et al. in 2015 sought to address these shortcomings by solving for the magnetoconductivity corrections due to scalar and spin-orbit scatterers in the Dirac surface states of a TI [34]. The Dirac state model they developed is presented in Eq. 1.28. The model predicts WAL ($\alpha = -0.5$) regardless of spin-orbit scattering strength, which means it only applies to TI surface states that are free from significant magnetic scattering effects, as these tend to suppress WAL in real systems [35]. Figure 5.9 shows the perpendicular magnetoconductance of several $(Bi_{0.35}Sb_{0.65})_2Te_3$ thin films, two grown on non-magnetic, insulating substrates, Al_2O_3 and MgF_2, and the other grown on an antiferromagnetic, insulating thin film of MnF_2, at $T = 2$ K. Each sample exhibits WAL, which is fit to the HLN model in Fig. 5.9(a) and to the Dirac state model in Fig. 5.9(b). The values derived from the Dirac state model

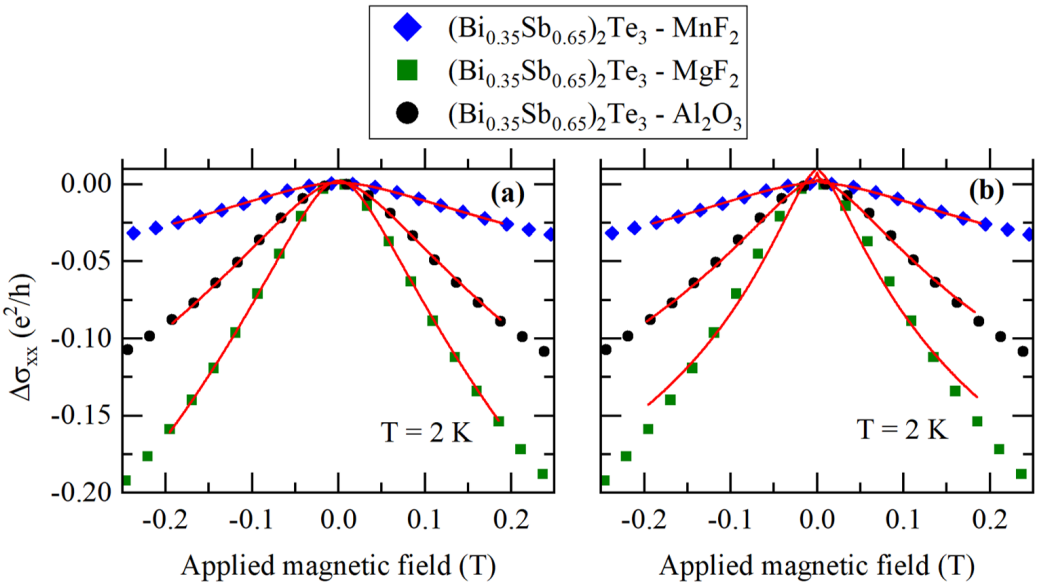

Figure 5.9: Perpendicular magnetoconductivity of several $(Bi_{0.35}Sb_{0.65})_2Te_3$ thin films at $T = 2$ K. Red curves are fits to (a) Eq. 1.25 the HLN model, and (b) Eq. 1.28 the Dirac state WAL model. The $(Bi_{0.35}Sb_{0.65})_2Te_3$ - MnF_2 sample is measured with the current applied perpendicular to the c-axis of the MnF_2 film.

fits to the magnetoconductivity curves shown in Fig. 5.9(b) are presented in table 5.3. The Dirac state model has many degrees of freedom, therefore in order to reduce the degrees of freedom and reduce the errors on the derived values, an approximation is made that the parameter $\tilde{\lambda}$, the relative strength of the spin-orbit scattering, can be set to $\tilde{\lambda} = 0.01$ and held constant. This is an appropriate approximation as the Dirac state model was developed under the assumption that $\tilde{\lambda} << 1$. The fit can further be improved by using the elastic scattering time τ_e calculated via the Al'tshuler-Aronov-Lee model presented in Fig. 5.8 as a constant in the Dirac state model fits. This too is an appropriate simplification as in both models τ_e describes the time between electron scattering events that do not cause the phase of the electron wavefunction to decohere. The derived values from the Dirac state model fit are the

phase coherence length τ_ϕ, the Fermi velocity ν_F, and a constant offset value C to account for a non-zero conductivity at zero applied magnetic field in this model, and are presented in table 5.3.

Sample	τ_e (ps)	τ_ϕ (ps)	$\nu_F(10^3$ m/s)	C (e^2/h)
BST - Al_2O_3	0.54	4.6 ± 2.4	21 ± 6	-0.33 ± 0.08
BST - MgF_2	0.63	6.0 ± 3.6	22 ± 9	-0.33 ± 0.10
BST - MnF_2 ($\mathbf{J} \perp \mathbf{c}$)	0.40	0.95 ± 0.10	33 ± 3	-0.11 ± 0.02
BST - MnF_2 ($\mathbf{J}\|\|\mathbf{c}$)	0.48	0.82 ± 0.04	33 ± 1	-0.11 ± 0.01

Table 5.3: Values derived from Al'shuler-Aronov-Lee magnetoconductivity (Eq. 1.37) fits to the data shown in Fig. 5.8(b).

HLN model fits to the magneconductivity curves shown in Fig. 5.9(a) are also performed, with the derived values from the fits shown in table 5.4. Magnetoconductivity measurements and fits for the $(Bi_{0.35}Sb_{0.65})_2Te_3$-$MnF_2$ bilayer with the current applied parallel and perpendicular to the c-axis of the MnF_2 layer are shown in Fig. 5.10.

Sample	α	l_ϕ (nm)
$(Bi_{0.35}Sb_{0.65})_2Te_3$ - Al_2O_3	-0.57 ± 0.04	73 ± 2
$(Bi_{0.35}Sb_{0.65})_2Te_3$ - MgF_2	-0.82 ± 0.03	81 ± 2
$(Bi_{0.35}Sb_{0.65})_2Te_3$ - MnF_2 ($\mathbf{J} \perp \mathbf{c}$)	-0.21 ± 0.01	65 ± 1
$(Bi_{0.35}Sb_{0.65})_2Te_3$ - MnF_2 ($\mathbf{J}\|\|\mathbf{c}$)	-0.22 ± 0.01	55 ± 1

Table 5.4: Values derived from HLN fits to the conductivity data shown in Fig. 5.9(a).

The Dirac state model fits shown in Fig. 5.9(b) and Fig. 5.10(b) and the values derived from these fits, shown in table 5.3, provide a useful tool for characterizing the low temperature transport properties of the 2D surface states of the TI. Notably, from the magnetoconductivity the Dirac state model provides a fit value for the Fermi velocity near the Dirac point, a value that is often determined from angle-resolved photoemission spectroscopy (ARPES). The Fermi velocity values derived from this model are on the order of 10^4 m/s, which is an order of magnitude smaller than the Fermi velocity at the Dirac point

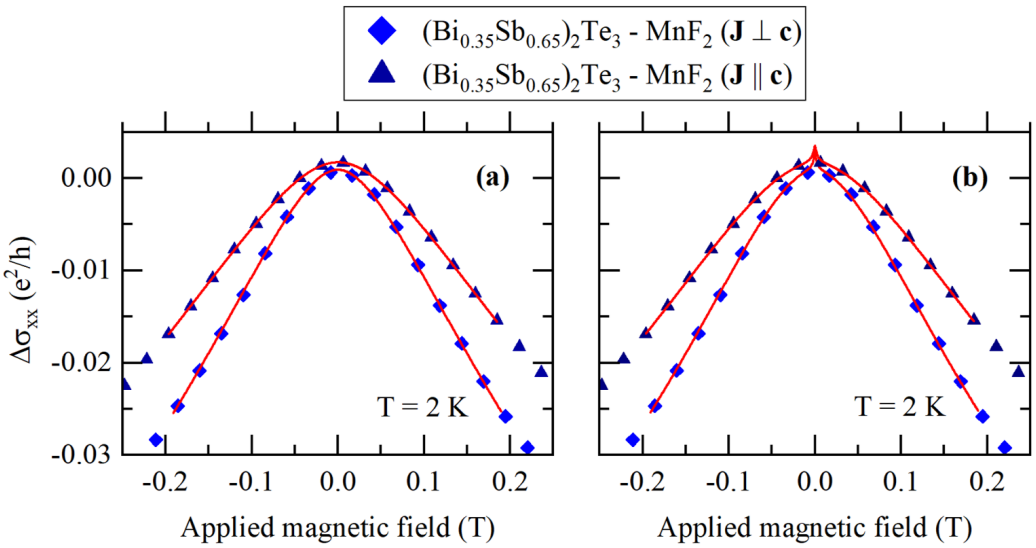

Figure 5.10: Perpendicular magnetoconductivity vs applied field of $(Bi_{0.35}Sb_{0.65})_2Te_3$-$MnF_2$ bilayers measured with the current applied parallel and perpendicular to the *c*-axis of the MnF_2 layer, respectively. Red curves represent fits to (a) the HLN model and (b) the Dirac state model.

reported by ARPES of similar TI samples [89, 90]. It is possible that the Fermi velocity is lower in the samples measured in this chapter because the Fermi level is unlikely to be precisely at the Dirac point. It is also worth noting that a measurement of the Fermi velocity in a Bi_2Te_3 crystal by microwave cyclotron resonance derived a value of 3.2×10^3 m/s, an order of magnitude smaller than the value derived here by Dirac state model fits to the magnetoconductivity [92].

The HLN model fits shown in Fig. 5.9(a) and Fig. 5.10(a) yield interesting insight into the effects of the MnF_2 interface on electronic transport of the BST films. As shown in table 5.4, the two BST films grown on non-magnetic substrates of Al_2O_3 and MgF_2 respectively, have values of α that correspond to the symplectic case, as is expected for TI films without magnetic scatterers. From the HLN model, each 2D channel in the symplectic case contributes an additive factor of -0.5 to α, therefore in a TI thin film, $\alpha = -0.5$ is indicative

of a single conducting channel, hybridizing the top and bottom surface states of the TI, as is observed in the $(Bi_{0.35}Sb_{0.65})_2Te_3$ - Al_2O_3 sample. A value of α larger in magnitude than -0.5, as observed in the $(Bi_{0.35}Sb_{0.65})_2Te_3$ - MgF_2 sample, is indicative of some decoupling of the top and bottom surface states of the TI into independent 2D states that each contribute to the cumulative value of α [93]. If the value of α approaches zero, then the electronic state is approaching the unitary case, where magnetic scattering effects dominate and localization is suppressed. HLN fits to the $(Bi_{0.35}Sb_{0.65})_2Te_3$ - MnF_2 bilayers show that the electronic states of the BST layer are approaching the unitary case, suggesting the presence of enhanced magnetic scattering in these bilayers, which must be due to the interface with the MnF_2 antiferromagnet. The fact that $\alpha = -0.22$ in these samples is consistent with the interpretation of two decoupled 2D conducting channels with additive values of α. The top surface of the TI has no magnetic interface and thus is in the symplectic case, contributing a value of $\alpha = -0.5$. The bottom surface of the TI, by contrast, is interfaced with the antiferromagnetic MnF_2 layer. If the magnetic scattering at this interface is strong, then that bottom channel will be in the unitary case and contribute a value of $\alpha = 0$ to the total conductivity. Taking the average of these two values, as the magnetoconductivity measurement cannot separate the contributions from the two channels, yields a value of $\alpha = -0.25$, remarkably close to the observed value. These results suggest that the surface states of the BST film are coupling with the magnetic moments of the MnF_2 film, in a way that could be potentially exploitable in future magnetoelectric transduction experiments.

5.3.3 Summary

To summarize the results of this chapter, it has been demonstrated how co-doped $(BiSb)_2Te_3$ TI films can be grown on MnF_2 thin films. Characterization of the carrier density of these films indicates that the Fermi level can be tuned to lie in the bulk band gap, and the dependence of the phase coherence length with temperature indicates 2D electronic transport in these films, both evidence that the transport is dominated by the 2D surface states. Weak antilocalization of non-magnetic TI films can be fit to a Dirac state model of magnetoconductivity that properly accounts for the 2D nature of the TI surface states. This model is particularly useful for deriving the Fermi velocity of the TI without need for ARPES measurements, but this model may be less accurate in describing TI films with significant magnetic scattering effects, as the Dirac nature of the surface states is disrupted by the presence of the magnetic scattering centers. Alternatively, the HLN model can be used to fit to the magnetoconductivity data of TI films with significant magnetic scattering, which reveals evidence of enhanced magnetic scattering in BST films interfaced with MnF_2. This enhanced magnetic scattering is believed to be due to proximity interaction effects between the conducting surface states of the BST and the magnetic order in the MnF_2 and demonstrates the potential utility of this platform to exhibit other magnetoelectric transduction effects.

Chapter 6

Conclusions

The work presented here represents advancements in the scientific understanding of the electronic and magnetic properties of the transition metal fluoride antiferromagnetic insulator and topological insulator thin films, as well as development and characterization of the novel antiferromagnetic insulator alloy $Mn_xNi_{1-x}F_2$ and antiferromagnetic insulator-topological insulator bilayers.

Growth of thin film MnF_2 (110) on MgF_2 (110) revealed piezomagnetic effects in the MnF_2 film due to epitaxial strain from growth on the smaller MgF_2 substrate. To alleviate the epitaxial strain at the interface, a novel growth process was developed where a graded $(MnNi)F_2$ buffer layer is used to gradually adjust the interface lattice parameter. Use of the graded buffer layer enabled the growth of MnF_2 thin films free from strain and piezomagnetic changes to the transition temperature. Fixed stoichiometry thin film alloys of $Mn_xNi_{1-x}F_2$ were grown on MgF_2 (110) substrates and the magnetic phase diagram of the system was developed from experiment and theory. The alloys show evidence of two additional magnetic phases, an oblique antiferromagnetic phase and an emergent phase that is believed to be either spin glass or helical in nature. Fits to mean field theory are used to derive the exchange energies between ions

in the alloy and to predict the angle and stoichiometric range of the oblique phase, with the derivation of the latter from the spin Hamiltonian being presented in full in the text. The results of the crystallographic and magnetic characterization of MnF_2 and $Mn_xNi_{1-x}F_2$ thin films represent advancements in the understanding of the magnetic ordering dynamics of these systems and systems like them.

Magnetic and electronic transport measurements of thin films of the ferromagnetic TI, Mn doped Bi_2Te_3, exhibited magnetization strength that increased with decreasing bulk carrier density. This correlation, which initially seems counter intuitive to the behavior of ferromagnetic metals, is believed to be due to RKKY interaction long range magnetic ordering mediated through the conduction electrons of the TI surface states, a mechanism unique to the TI system. The MBT films grown on antiferromagnetic NiF_2 thin films show signs of a suppressed magnetic moment, evidence of magnetoelectric proximity effects at the MBT-NiF_2 interface.

In co-doped $(BiSb)_2Te_3$ TI thin films, it was shown how the Fermi level can be tuned to lie in the bulk band gap by controlling the stoichiometric ratio of Bi and Sb, and how these co-doped BST films were successfully grown on MnF_2 thin films. Measurements of the parallel magnetoconductance at low temperature are fit to the Al'tshuler Aronov model, from which the phase coherence length of the charge carriers and the dimensionality of the transport is derived, demonstrating that the BST-MnF_2 bilayers exhibit 2D transport from the surface states due to the Fermi level being tuned into the bulk band gap. Measurements of the perpendicular magnetoconductance at low temperature are also performed and fit to the HLN model for quasi-2D transport and a Dirac model of magnetoconductance for 2D Dirac states, from which parameters related to phase coherence are derived. Comparison of these two models

and their fits to the data demonstrate how the surface states of TI films with magnetic scattering centers deviate from the Dirac state. Suppressed weak antilocalization in BST-MnF_2 films is evidence of enhance magnetic scattering, believed to be due to proximity effect interactions between the BST surface states and the magnetic order of the MnF_2 film.

Future work stemming from these results could take many forms. The spin structure of the emergent magnetic phase observed in $Mn_xNi_{1-x}F_2$ thin film alloys has yet to be definitively identified. Further experiments could investigate the structure of this phase with neutron scattering measurements, to check for the formation of a skyrmion lattice, or by Raman scattering measurements to check for additional magnon modes associated with either the skyrmion phase or a spin glass phase. Fermi level tuned BST-MnF_2 bilayers have the potential to exhibit enhanced magnetoelectric coupling effects when compared with Pt-MnF_2 bilayers that have been used in the past. Spin pumped electric voltage from magnon modes in MnF_2, electrical detection of the spin Seebeck effect, and anomalous planar Hall effects are a few types of magnetoelectric phenomena that could be investigated using this novel platform.

Taken together, these results add to the scientific understanding of magnetic and electronic spin based physical phenomena and are evidence of the wealth of unique behaviors that can emerge from these novel systems. Continued fundamental research is necessary to manifest the full promise of these materials and is a near certainty to reveal yet undiscovered physical phenomena.

Appendix A

Appendix

Bibliography

[1] K. Yoshida, D. Kunikita, Y. Miyazaki, Y. Nishida, T. Miyao, H. Matsuzaki, *Radiocarbon* **2013**, *55*, Publisher: Cambridge University Press, 1322–1333.

[2] R. Maddin, J. D. Muhly, T. S. Wheeler, *Scientific American* **1977**, *237*, Publisher: Scientific American, a division of Nature America, Inc., 122–131.

[3] V. K. Joshi, *Engineering Science and Technology an International Journal* **2016**, *19*, 1503–1513.

[4] A. Fert, N. Reyren, V. Cros, *Nature Reviews Materials* **2017**, *2*, Number: 7 Publisher: Nature Publishing Group, 1–15.

[5] N. Kent, N. Reynolds, D. Raftrey, I. T. G. Campbell, S. Virasawmy, S. Dhuey, R. V. Chopdekar, A. Hierro-Rodriguez, A. Sorrentino, E. Pereiro, S. Ferrer, F. Hellman, P. Sutcliffe, P. Fischer, *Nature Communications* **2021**, *12*, Number: 1 Publisher: Nature Publishing Group, 1562.

[6] S. Mühlbauer, B. Binz, F. Jonietz, C. Pfleiderer, A. Rosch, A. Neubauer, R. Georgii, P. Böni, *Science* **2009**, *323*, Publisher: American Association for the Advancement of Science, 915–919.

[7] T. Kampfrath, A. Sell, G. Klatt, A. Pashkin, S. Mährlein, T. Dekorsy, M. Wolf, M. Fiebig, A. Leitenstorfer, R. Huber, *Nature Photonics* **2011**, *5*, Number: 1 Publisher: Nature Publishing Group, 31–34.

[8] I. Dzyaloshinsky, *Journal of Physics and Chemistry of Solids* **1958**, *4*, 241–255.

[9] T. Moriya, *Physical Review* **1960**, *120*, Publisher: American Physical Society, 91–98.

[10] T. Moriya, *Physical Review* **1960**, *117*, Publisher: American Physical Society, 635–647.

[11] A. Borovik-Romanov, A. Bazhan, N. Kreines, *Journal of Experimental and Theoretical Physics* **1973**, *37*, 695–702.

[12] P. Vaidya, S. A. Morley, J. van Tol, Y. Liu, R. Cheng, A. Brataas, D. Lederman, E. del Barco, *Science* **2020**, *368*, Publisher: American Association for the Advancement of Science, 160–165.

[13] S. M. Wu, W. Zhang, A. KC, P. Borisov, J. E. Pearson, J. S. Jiang, D. Lederman, A. Hoffmann, A. Bhattacharya, *Physical Review Letters* **2016**, *116*, Publisher: American Physical Society, 097204.

[14] M. I. Dyakonov, V. I. Perel, *Physics Letters A* **1971**, *35*, 459–460.

[15] M. D'yakonov, V. Perel', *JETP Letters* **1971**, 657.

[16] J. E. Hirsch, *Physical Review Letters* **1999**, *83*, Publisher: American Physical Society, 1834–1837.

[17] Y. K. Kato, R. C. Myers, A. C. Gossard, D. D. Awschalom, *Science* **2004**, *306*, Publisher: American Association for the Advancement of Science, 1910–1913.

[18] J. Sinova, S. O. Valenzuela, J. Wunderlich, C. H. Back, T. Jungwirth, *Reviews of Modern Physics* **2015**, *87*, Publisher: American Physical Society, 1213–1260.

[19] H. Nakayama, M. Althammer, Y.-T. Chen, K. Uchida, Y. Kajiwara, D. Kikuchi, T. Ohtani, S. Geprägs, M. Opel, S. Takahashi, R. Gross, G. E. W. Bauer, S. T. B. Goennenwein, E. Saitoh, *Physical Review Letters* **2013**, *110*, Publisher: American Physical Society, 206601.

[20] N. Nagaosa, J. Sinova, S. Onoda, A. H. MacDonald, N. P. Ong, *Reviews of Modern Physics* **2010**, *82*, Publisher: American Physical Society, 1539–1592.

[21] K. v. Klitzing, G. Dorda, M. Pepper, *Physical Review Letters* **1980**, *45*, Publisher: American Physical Society, 494–497.

[22] K. von Klitzing, *Annual Review of Condensed Matter Physics* **2017**, *8*, _eprint: https://doi.org/10.1146/annurev-conmatphys-031016-025148, 13–30.

[23] C.-Z. Chang, J. Zhang, X. Feng, J. Shen, Z. Zhang, M. Guo, K. Li, Y. Ou, P. Wei, L.-L. Wang, Z.-Q. Ji, Y. Feng, S. Ji, X. Chen, J. Jia, X. Dai, Z. Fang, S.-C. Zhang, K. He, Y. Wang, L. Lu, X.-C. Ma, Q.-K. Xue, *Science* **2013**, *340*, Publisher: American Association for the Advancement of Science, 167–170.

[24] J. Jiang, D. Xiao, F. Wang, J.-H. Shin, D. Andreoli, J. Zhang, R. Xiao, Y.-F. Zhao, M. Kayyalha, L. Zhang, K. Wang, J. Zang, C. Liu, N. Samarth, M. H. W. Chan, C.-Z. Chang, *Nature Materials* **2020**, *19*, Number: 7 Publisher: Nature Publishing Group, 732–737.

[25] L. Onsager, *Physical Review* **1944**, *65*, Publisher: American Physical Society, 117–149.

[26] F. Matsubara, S. Inawashiro, *Journal of the Physical Society of Japan* **1977**, *42*, Publisher: The Physical Society of Japan, 1529–1537.

[27] G. K. Wertheim, H. J. Guggenheim, M. Butler, V. Jaccarino, *Physical Review* **1969**, *178*, Publisher: American Physical Society, 804–805.

[28] L. Fu, C. L. Kane, *Physical Review B* **2006**, *74*, Publisher: American Physical Society, 195312.

[29] T. Fukui, T. Fujiwara, Y. Hatsugai, *Journal of the Physical Society of Japan* **2008**, *77*, Publisher: The Physical Society of Japan, 123705.

[30] X.-L. Qi, T. L. Hughes, S.-C. Zhang, *Physical Review B* **2008**, *78*, Publisher: American Physical Society, 195424.

[31] R. Moessner, J. E. Moore, *Topological Phases of Matter: New Particles, Phenomena, and Ordering Principles*, Cambridge University Press, **2021**.

[32] S. Hikami, A. I. Larkin, Y. Nagaoka, *Progress of Theoretical Physics* **1980**, *63*, 707–710.

[33] H.-T. He, G. Wang, T. Zhang, I.-K. Sou, G. K. L. Wong, J.-N. Wang, H.-Z. Lu, S.-Q. Shen, F.-C. Zhang, *Physical Review Letters* **2011**, *106*, Publisher: American Physical Society, 166805.

[34] P. Adroguer, W. E. Liu, D. Culcer, E. M. Hankiewicz, *Physical Review B* **2015**, *92*, Publisher: American Physical Society, 241402.

[35] M. Liu, J. Zhang, C.-Z. Chang, Z. Zhang, X. Feng, K. Li, K. He, L.-l. Wang, X. Chen, X. Dai, Z. Fang, Q.-K. Xue, X. Ma, Y. Wang, *Physical Review Letters* **2012**, *108*, Publisher: American Physical Society, 036805.

[36] B. L. Altshuler, A. G. Aronov, *Journal of Experimental and Theoretical Physics* **1981**, *33*.

[37] M. E. Gershenzon, B. N. Gubankov, Y. E. Zhuravlev, *Journal of Experimental and Theoretical Physics* **1982**, *56*, 1362.

[38] R. S. Markiewicz, C. J. Rollins, *Physical Review B* **1984**, *29*, Publisher: American Physical Society, 735–747.

[39] B. L. Altshuler, A. G. Aronov, D. E. Khmelnitsky, *Journal of Physics C: Solid State Physics* **1982**, *15*, 7367.

[40] B. L. Altshuler, A. G. Aronov, P. A. Lee, *Physical Review Letters* **1980**, *44*, Publisher: American Physical Society, 1288–1291.

[41] P. A. Lee, T. V. Ramakrishnan, *Reviews of Modern Physics* **1985**, *57*, 287–337.

[42] D. V. Schroeder, *An Introduction to Thermal Physics*, Addison Wesley Longman, **2000**.

[43] S. Hasegawa in *Characterization of Materials*, John Wiley & Sons, **2012**.

[44] Y. Kainuma, *Acta Crystallographica* **1955**, *8*, Publisher: International Union of Crystallography, 247–257.

[45] J. R. Arthur, *Surface Science* **2002**, *500*, 189–217.

[46] C. Kittel, *Introduction to Solid State Physics*, Eighth, John Wiley & Sons, **2005**.

[47] A. Glavic, M. Björck, *Journal of Applied Crystallography* **2022**, *55*, Number: 4 Publisher: International Union of Crystallography, 1063–1071.

[48] F. A. Perez, P. Borisov, T. A. Johnson, T. D. Stanescu, R. Trappen, M. B. Holcomb, D. Lederman, M. R. Fitzsimmons, A. A. Aczel, T. Hong, *Physical Review Letters* **2015**, *114*, Publisher: American Physical Society, 097201.

[49] J. W. Stout, S. A. Reed, *Journal of the American Chemical Society* **1954**, *76*, Publisher: American Chemical Society, 5279–5281.

[50] S. Emori, U. Bauer, S.-M. Ahn, E. Martinez, G. S. D. Beach, *Nature Materials* **2013**, *12*, Number: 7 Publisher: Nature Publishing Group, 611–616.

[51] J. Barker, O. A. Tretiakov, *Physical Review Letters* **2016**, *116*, Publisher: American Physical Society, 147203.

[52] X. Zhang, Y. Zhou, M. Ezawa, *Scientific Reports* **2016**, *6*, Number: 1 Publisher: Nature Publishing Group, 24795.

[53] F. N. Rybakov, N. S. Kiselev, A. B. Borisov, L. Döring, C. Melcher, S. Blügel, *APL Materials* **2022**, *10*, Publisher: American Institute of Physics, 111113.

[54] J. Barak, V. Jaccarino, S. M. Rezende, *Journal of Magnetism and Magnetic Materials* **1978**, *9*, 323–332.

[55] J. Zhao, A. V. Bragas, R. Merlin, D. J. Lockwood, *Physical Review B* **2006**, *73*, Publisher: American Physical Society, 184434.

[56] I. S. Jacobs, *Journal of Applied Physics* **1961**, *32*, S61–S62.

[57] G. P. Felcher, R. Kleb, *Europhysics Letters (EPL)* **1996**, *36*, 455–460.

[58] M. T. Hutchings, B. D. Rainford, H. J. Guggenheim, *Journal of Physics C: Solid State Physics* **1970**, *3*, 307.

[59] A. Borovik-Romanov, *Soviet Physics JETP* **1960**, *11*, 786–793.

[60] J. Baruchel, M. Schlenker, B. Barbara, *Journal of Magnetism and Magnetic Materials* **1980**, *15-18*, 1510–1512.

[61] J. Baruchel, A. Draperi, M. El Kadiri, G. Fillion, M. Maeder, P. Molho, J. L. Porteseil, *Le Journal de Physique Colloques* **1988**, *49*, C8–1895–C8–1896.

[62] A. L. Patterson, *Physical Review* **1939**, *56*, 978–982.

[63] W. Baur, *Acta Crystallographica Section B Structural Crystallography and Crystal Chemistry* **1976**, *32*, 2200–2204.

[64] J. Haines, J. M. Léger, F. Gorelli, D. D. Klug, J. S. Tse, Z. Q. Li, *Physical Review B* **2001**, *64*, Publisher: American Physical Society, 134110.

[65] H. Shi, D. Lederman, K. V. O'Donovan, J. A. Borchers, *Physical Review B* **2004**, *69*, Publisher: American Physical Society, 214416.

[66] M. T. Hutchings, M. F. Thorpe, R. J. Birgeneau, P. A. Fleury, H. J. Guggenheim, *Physical Review B* **1970**, *2*, Publisher: American Physical Society, 1362–1373.

[67] I. A. Sergienko, E. Dagotto, *Physical Review B* **2006**, *73*, Publisher: American Physical Society, 094434.

[68] S. Venugopalan, A. Petrou, R. R. Galazka, A. K. Ramdas, *Solid State Communications* **1981**, *38*, 365–369.

[69] G. M. Rotaru, B. Roessli, A. Amato, S. N. Gvasaliya, C. Mudry, S. G. Lushnikov, T. A. Shaplygina, *Physical Review B* **2009**, *79*, Publisher: American Physical Society, 184430.

[70] O. Nikotin, P. A. Lindgård, O. W. Dietrich, *Journal of Physics C: Solid State Physics* **1969**, *2*, 1168.

[71] D. Bloch, *Journal of Physics and Chemistry of Solids* **1966**, *27*, 881–885.

[72] F. Keffer, *Physical Review* **1952**, *87*, Publisher: American Physical Society, 608–612.

[73] C. Liu, Y. Zang, W. Ruan, Y. Gong, K. He, X. Ma, Q.-K. Xue, Y. Wang, *Physical Review Letters* **2017**, *119*, Publisher: American Physical Society, 176809.

[74] L. D. Alegria, H. Ji, N. Yao, J. J. Clarke, R. J. Cava, J. R. Petta, *Applied Physics Letters* **2014**, *105*, Publisher: American Institute of Physics, 053512.

[75] J.-Q. Yan, Q. Zhang, T. Heitmann, Z. Huang, K. Y. Chen, J.-G. Cheng, W. Wu, D. Vaknin, B. C. Sales, R. J. McQueeney, *Physical Review Materials* **2019**, *3*, Publisher: American Physical Society, 064202.

[76] X. Kou, M. Lang, Y. Fan, Y. Jiang, T. Nie, J. Zhang, W. Jiang, Y. Wang, Y. Yao, L. He, K. L. Wang, *ACS Nano* **2013**, *7*, Publisher: American Chemical Society, 9205–9212.

[77] C.-Z. Chang, J. Zhang, M. Liu, Z. Zhang, X. Feng, K. Li, L.-L. Wang, X. Chen, X. Dai, Z. Fang, X.-L. Qi, S.-C. Zhang, Y. Wang, K. He, X.-C. Ma, Q.-K. Xue, *Advanced Materials* **2013**, *25*, _eprint: https://onlinelibrary.wiley.com/doi/pdf/ 1065–1070.

[78] Y. S. Hor, P. Roushan, H. Beidenkopf, J. Seo, D. Qu, J. G. Checkelsky, L. A. Wray, D. Hsieh, Y. Xia, S.-Y. Xu, D. Qian, M. Z. Hasan, N. P. Ong, A. Yazdani, R. J. Cava, *Physical Review B* **2010**, *81*, Publisher: American Physical Society, 195203.

[79] N. H. Jo, K. Lee, J. Kim, J. Jang, J. Kim, M.-H. Jung, *Applied Physics Letters* **2014**, *104*, 252413.

[80] D. Zhang, A. Richardella, D. W. Rench, S.-Y. Xu, A. Kandala, T. C. Flanagan, H. Beidenkopf, A. L. Yeats, B. B. Buckley, P. V. Klimov, D. D. Awschalom, A. Yazdani, P. Schiffer, M. Z. Hasan, N. Samarth, *Physical Review B* **2012**, *86*, Publisher: American Physical Society, 205127.

[81] J. S. Lee, A. Richardella, D. W. Rench, R. D. Fraleigh, T. C. Flanagan, J. A. Borchers, J. Tao, N. Samarth, *Physical Review B* **2014**, *89*, Publisher: American Physical Society, 174425.

[82] J. G. Checkelsky, J. Ye, Y. Onose, Y. Iwasa, Y. Tokura, *Nature Physics* **2012**, *8*, Number: 10 Publisher: Nature Publishing Group, 729–733.

[83] P. Sessi, F. Reis, T. Bathon, K. A. Kokh, O. E. Tereshchenko, M. Bode, *Nature Communications* **2014**, *5*, Number: 1 Publisher: Nature Publishing Group, 5349.

[84] E. Stoner, *Proceedings of the Royal Society of London. Series A. Mathematical and Physical Sciences* **1938**, *165*, 372–414.

[85] R. Watanabe, R. Yoshimi, M. Kawamura, M. Mogi, A. Tsukazaki, X. Z. Yu, K. Nakajima, K. S. Takahashi, M. Kawasaki, Y. Tokura, *Applied Physics Letters* **2019**, *115*, 102403.

[86] H.-Z. Lu, J. Shi, S.-Q. Shen, *Physical Review Letters* **2011**, *107*, Publisher: American Physical Society, 076801.

[87] A. R. Mellnik, J. S. Lee, A. Richardella, J. L. Grab, P. J. Mintun, M. H. Fischer, A. Vaezi, A. Manchon, E.-A. Kim, N. Samarth, D. C. Ralph, *Nature* **2014**, *511*, Number: 7510 Publisher: Nature Publishing Group, 449–451.

[88] M. Jamali, J. S. Lee, J. S. Jeong, F. Mahfouzi, Y. Lv, Z. Zhao, B. K. Nikolić, K. A. Mkhoyan, N. Samarth, J.-P. Wang, *Nano Letters* **2015**, *15*, Publisher: American Chemical Society, 7126–7132.

[89] J. Zhang, C.-Z. Chang, Z. Zhang, J. Wen, X. Feng, K. Li, M. Liu, K. He, L. Wang, X. Chen, Q.-K. Xue, X. Ma, Y. Wang, *Nature Communications* **2011**, *2*, Number: 1 Publisher: Nature Publishing Group, 574.

[90] Y. L. Chen, J. G. Analytis, J.-H. Chu, Z. K. Liu, S.-K. Mo, X. L. Qi, H. J. Zhang, D. H. Lu, X. Dai, Z. Fang, S. C. Zhang, I. R. Fisher, Z. Hussain, Z.-X. Shen, *Science* **2009**, *325*, Publisher: American Association for the Advancement of Science, 178–181.

[91] Y. Jiang, Y. Y. Sun, M. Chen, Y. Wang, Z. Li, C. Song, K. He, L. Wang, X. Chen, Q.-K. Xue, X. Ma, S. B. Zhang, *Physical Review Letters* **2012**, *108*, Publisher: American Physical Society, 066809.

[92] A. Wolos, S. Szyszko, A. Drabinska, M. Kaminska, S. G. Strzelecka, A. Hruban, A. Materna, M. Piersa, *Physical Review Letters* **2012**, *109*, 247604.

[93] W. J. Wang, K. H. Gao, Z. Q. Li, *Scientific Reports* **2016**, *6*, Number: 1 Publisher: Nature Publishing Group, 25291.